ISSN 2616-8170

Robotics Society of Taiwan

iRobotics

VOLUME 1
NUMBER 3
SEPTEMBER 2018

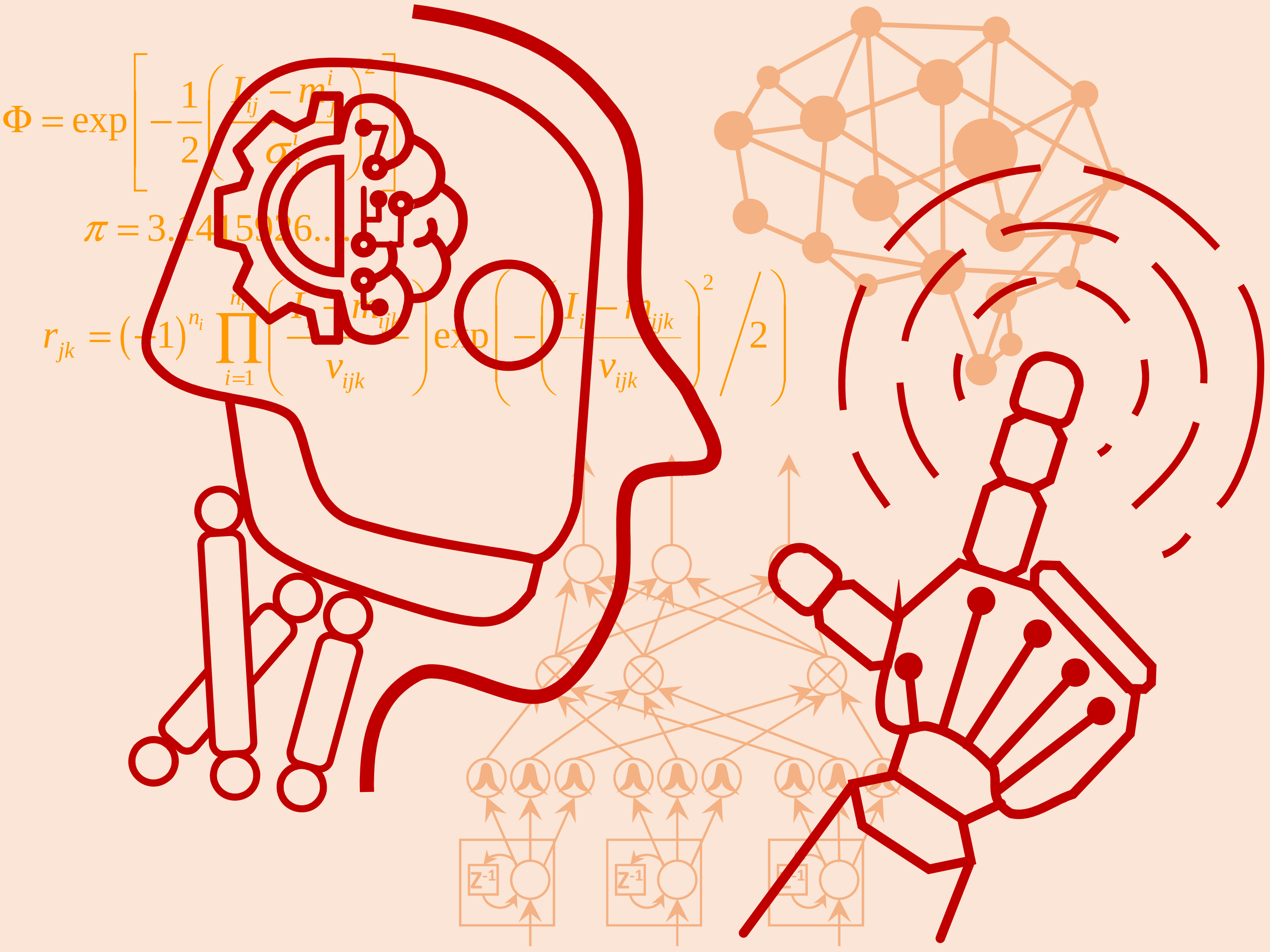

PUBLISHED BY THE ROBOTICS SOCIETY OF TAIWAN

*i*Robotics

EDITORIAL BOARD

Editor-in-Chief

Ching-Chih Tsai,
Dept. of Electrical Engineering,
Nat’l Chung Hsing Univ.,Taiwan
Email: cctsai@nchu.edu.tw

Tzuu-Hseng S. Li,
Dept. of Electrical Engineering,
Nat’l Cheng Kung Univ., Taiwan
Email: thsli@mail.ncku.edu.tw

Editors

C. L. Philip Chen,
Univ. of Macau., Macau

Ren C. Luo,
Nat’l Taiwan Univ., Taiwan

Satoshi Tadokoro,
Tohoku Univ., Japan

Li-Chen Fu,
Nat’l Taiwan Univ., Taiwan

Tsu-Tian Lee,
Tamkang Univ., Taiwan

Tsu-Chin Tsao,
Univ. of California, Los Angeles, U.S.A.

Han-Pang Huang,
Nat‘l Taiwan Univ., Taiwan

Shun-Feng Su,
Nat’l Taiwan Univ. of Sci. and Tech., Taiwan

Wen-June Wang,
Nat’l Central Univ., Taiwan

Chung-Liang Chang,
Nat’l Pingtung Univ. of Sci. and Tech., Taiwan

Raja Chatila,
University Pierre et Marie Curie, France

Chin-Sheng Chen,
Nat’l Taipei Univ. of Tech., Taiwan

Chih-Yung Cheng,
Nat’l Taiwan Ocean Univ., Taiwan

Ming-Yang Cheng,
Nat’l Cheng Kung Univ., Taiwan

Chen-Chien James Hsu,
Nat’l Taiwan Normal Univ., Taiwan

Jwu-Sheng Hu,
ITRI,
Taiwan

Guo-Shing Huang,
Nat’l Chin-Yi Univ. of Tech., Taiwan

Hsu-Chih Huang,
Nat’l Ilan Univ.,
Taiwan

Kao-Shing Hwang,
Nat’l Sun-Yat Sen Univ., Taiwan

Chung-Hsien Kuo,
Nat’l Taiwan Univ. of Sci. and Tech., Taiwan

Chia-Feng Juang,
Nat’l Chung Hsing Univ., Taiwan

Feng-Li Lian,
Nat‘l Taiwan Univ., Taiwan

Chih-Jer Lin,
Nat’l Taipei Univ. of Tech., Taiwan

Chyi-Yen Lin,
Nat’l Taiwan Univ. of Sci. and Tech., Taiwan

Hsien-I Lin,
Nat’l Taipei Univ. of Tech., Taiwan

Huei-Yung Lin,
Nat’l Chung Cheng Univ., Taiwan

Jung-Shan Lin,
Nat’l Chi-Nan Univ., Taiwan

Pei-Chun Lin,
Nat’l Taiwan Univ., Taiwan

Alan Liu,
Nat’l Chung Cheng Univ., Taiwan

Yen-Chen Liu,
Nat’l Cheng Kung Univ., Taiwan

Yi-Hung Liu,
Nat’l Taipei Univ. of Tech., Taiwan

Chi-Huang Lu,
Hsiuping Univ. of Sci. and Tech., Taiwan

Max Meng,
Chinese Univ. of Hong Kong, China

Stephen D Prior
Univ. of Southampton,
United Kingdom

Ming-Yuan Shieh,
Southern Taiwan Univ. of Sci. and Tech., Taiwan

Jae-Bok Song,
Korea Univ.,
Korea

Kai-Tai Song,
Nat’l Chiao Tung Univ., Taiwan

Kuo-Lan Su,
Nat’l Yunlin Univ. of Sci. and Tech., Taiwan

Tong-Boon Tang
Universiti Teknologi PETRONAS, Malaysia

Kuo-Yang Tu,
Nat’l Kaohsiung First Univ. of Sci. and Tech., Taiwan

Ming-Shyan Wang,
Sourthern Taiwan Univ. of Sci. and Tech., Taiwan

Rong-Jyue Wang,
Nat’l Formosa Univ., Taiwan

Wei-Yen Wang,
Nat’l Taiwan Normal Univ., Taiwan

Ching-Chang Wong,
Tamkang Univ.,
Taiwan

Sendren Sheng-Dong Xu,
Nat’l Taiwan Univ. of Sci. and Tech., Taiwan

Ting-Jen Yeh,
Nat’l Tsing Hua Univ., Taiwan

Jia-Yush Yen,
Nat’l Taiwan Univ., Taiwan

Ping-Lang Yen,
Nat’l Taiwan Univ., Taiwan

Kuu-Young Young,
Nat’l Chiao Tung Univ., Taiwan

Gwo-Ruey Yu,
Nat’l Chung Cheng Univ., Taiwan

PUBLISHER

Robotics Society of TAIWAN (RST)
Society President: Ching-Chih Tsai

Department of Electrical Engineering, National Chung Hsing University
Taichung, Taiwan

Tel: +886-4-2285-1549#601
URL: http://www.rst.org.tw

The ***i*****Robotics** is published quarterly each year by the Robotics Society of Taiwan (RST). Institutional rate: US$140 annually; individual annual subscription rate: US$50 for nonmembers, US$25 for members (including postage). Note that another US$100 is needed if the express is required.

Observer-based Impedance Control for Power Assisting Devices

Chao-Jen Chen, Ming-Yang Cheng, and Chun-Hsien Wu

Abstract—**Power assisting devices can be found in many exercise and rehabilitation applications. Since the power assisting devices have direct contact with the user, crucial issues, such as providing proper load/assistance force for the user during exercise or rehabilitation, and ensuring the safety of the user, need to be carefully addressed in its control design. In this paper, an observer-based impedance controller is developed to provide suitable load/assistance force for the user. In particular, the disturbance observer is used as an alternative to the force sensor in estimating the contact force between the user and device. Since the proposed disturbance observer for contact force estimation exploits the idea of "integration by parts", acceleration information is not essential. Finally, experimental results verify the effectiveness of the proposed observer-based impedance controller for power assisting devices.**

Index Terms—**Power assisting device, disturbance observer, impedance control.**

I. INTRODUCTION

POWER assisting devices can be used in applications such as exercise/fitness equipment, rehabilitation of spinal cord injury or stroke patients, limb muscle enhancement of workers, and bionic limbs of amputee patients. Recently, with increasing demands for rehabilitation and exercise equipment, the number of studies concerning the control design of power assisting devices has continued to increase. In particular, several manufacturing giants have developed walking assistance devices for the elderly and those who may need assistance force while walking or working [1]. Since the power assisting device has direct contact with the user, several issues need to be thoroughly addressed when developing its control scheme. For example, ensuring user safety is the top priority in the control design of the power assisting device. In addition, the power assisting device should provide an adequate amount of load/assistance force for the user to do exercise or rehabilitation effectively.

In all kinds of power assisting devices, robotic systems for rehabilitation and exercise have been extensively investigated [2-13]. For instance, to help those in need of rehabilitation, Noritsugu and Tanaka [2] developed a pneumatic artificial muscle actuator that exploited the idea of impedance control to perform different therapy modes such as isometric, isokinetic, and isotonic modes. In [3], a robotic task-practice system was developed to assist stroke patients who need rehabilitation in the performance of daily living functional tasks. In [5], Hwang *et al.* developed a disturbance observer to estimate the interactive torque and monitor the intentional motion of the user. Komada *et al.* [6] developed a robotic biofeedback exercise device that can be used in the physical therapy of patients for lower limb rehabilitation. Duschau-Wicke *et al.* [7] developed a path control strategy that exploits the idea of a compliant virtual wall for patients/healthy subjects to perform task-oriented training using a gait rehabilitation robot. In [9], Freeman *et al.* developed an upper limb rehabilitation system that employs a functional electrical stimulation model-based control method, where a planar robot arm is used as the load and the patient is asked to move the robot arm to periodically track a desired path. In [12], Wu *et al.* developed a 3-DOF lower limb rehabilitation robot for assisting stroke patients to recover mobility.

Regarding the power assisting devices for exercise, Li and Horowitz [14, 15] designed a controller which is based on the assumption that the force generated by the muscles of the user decreases as the velocity of exercise increases. Moreover, for the sake of safety, a control scheme is designed to maintain the passivity of the system so that the direction of the net energy is always from the user to the device. Another item of exercise equipment, a wearable unit on a bicycle, was developed by Kiryu and Yamashita [16]. The wearable unit can measure heart rate and the surface electromyogram serves to calculate the fatigue index using fuzzy logics, adjusting the torque-assistance ratio of the bicycle accordingly so as to prevent the user from severe muscular fatigue while exercising.

Recently, compliance control has become a hot research topic regarding control problems of the robot manipulator [17-20], thus playing a crucial role in power assisting devices. In particular, Calanca *et al.* [20] provided a thorough review of compliance control algorithms for the robot manipulator. Furthermore, human-robot interaction is also a research topic that has attracted, and continued to attract much attention [21, 22].

In order to achieve better exercise and rehabilitation outcomes, the load/force provided by the power assisting device should depend on the force/torque exerted by the user and whether he or she is doing exercise or rehabilitation. The

This work was supported in part by the Ministry of Science and Technology of the Republic of China, Taiwan, under Grant NSC99-2221-E-006-204-MY2 and by the Ministry of Economic Affairs of the Republic of China, Taiwan, under Grant MOEA101-EC-17-A-05- S1-192.

C.-J. Chen was with the Electrical Engineering Department, National Cheng Kung University, Tainan 701, Taiwan (e-mail: chaojen.chen@catcher-group.com).

M.-Y. Cheng is with the Electrical Engineering Department, National Cheng Kung University, Tainan 701, Taiwan (e-mail: mycheng@mail.ncku.edu.tw).

C.-H. Wu was with the Electrical Engineering Department, National Cheng Kung University, Tainan 701, Taiwan (e-mail: tnfsh117@hotmail.com)

above literature reviews indicate that most previous studies either used force/torque sensors or employed disturbance observers to detect the force/torque exerted by the user. However, the force/torque sensors are not cost-effective. In addition, the failure of force/torque sensors may trigger inappropriate assistance force and put the safety of the user in jeopardy.

It is worthy to note that some of the previous studies employing the disturbance observer require acceleration information when estimating external force/torque. However, the acceleration information in those previous studies is often obtained by performing numerical differentiations twice with respect to encoder data. As a result, it is not surprising that the obtained acceleration information usually contains significant noise and may lead to inaccurate detection results. In order to alleviate the aforementioned difficulties, this paper proposes an observer-based impedance controller to provide suitable loads/assistance force to the user. Most importantly, the proposed disturbance observer for estimating the contact force between the user and device exploits the idea of "integration by parts" so that acceleration information is not essential. In addition, the proposed force/torque sensorless solution can also play a redundant role in a power assisting device that is equipped with torque/force sensors so as to protect the safety of the user when the force/torque sensor malfunctions. The effectiveness of the proposed control approach is verified by several experiments.

The remainder of the paper is organized as follows. Section 2 lays out the dynamic model derivation and system parameter identification of the power assisting device used in this paper. Section 3 provides an overview of the proposed control scheme for the power assisting device. Section 4 and Section 5 elaborate upon the proposed disturbance observer and the impedance control scheme employed in this paper, respectively. Experimental results and conclusions are given in Section 6 and Section 7, respectively.

II. POWER ASSISTING DEVICE

A. Dynamic Model Derivation

Fig. 1 shows the simplified model of the 2-DOF power assisting device with the specific system parameters given in Table 1. Based on Fig. 1, the dynamic equations of the power assisting device can be derived by using the Lagrange's equation [23] to have a general form of

$$M(\theta)\ddot{\theta} + H(\theta,\dot{\theta})\dot{\theta} + G(\theta) = \tau \qquad (1)$$

where $\theta=[\theta_1 \quad \theta_2]^T$, $\dot{\theta}$ and $\ddot{\theta} \in R^2$ represent the angular position, angular velocity, and angular acceleration of the joints, respectively. $M(\theta)$ is the 2×2 inertia matrix, $H(\theta,\dot{\theta})$ is the 2×2 matrix containing Coriolis and centrifugal forces, $G(\theta)$ is the 2×1 gravity vector, and τ denotes the 2×1 torque vector of the device.

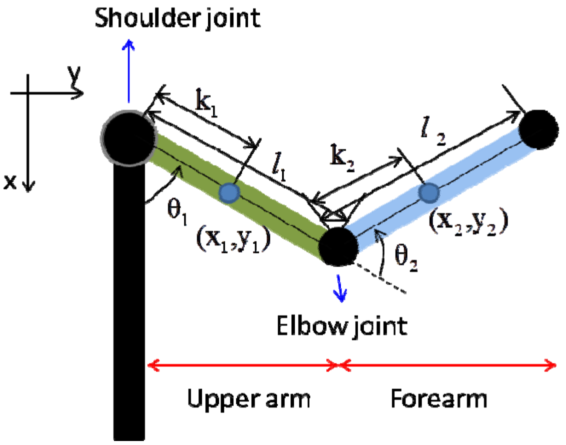

Fig. 1. Simplified model of the 2-DOF power assisting device.

TABLE I
NOTATIONS AND DEFINITIONS FOR THE SYSTEM PARAMETERS

Symbol	Definition
m_1	Mass of the upper arm
m_2	Mass of the forearm
l_1	Length of the upper arm
l_2	Length of the forearm
θ_1	Angle of the shoulder joint
θ_2	Angle of the elbow joint
k_1	Distance from the center of mass of the upper arm to the shoulder joint
k_2	Distance from the center of mass of the forearm to the elbow joint
I_1	Rotational inertia of the upper arm
I_2	Rotational inertia of the forearm
g	Earth gravitational acceleration
(x_1,y_1)	Position of the center of mass of the upper arm
(x_2,y_2)	Position of the center of mass of the forearm

Given the notation in Table 1, $M(\theta), H(\theta,\dot{\theta})$, and $G(\theta)$ can be described below.

$$M(\theta) = \begin{bmatrix} M_{11} & M_{12} \\ M_{21} & M_{22} \end{bmatrix}, \; H(\theta,\dot{\theta}) = \begin{bmatrix} H_{11} & H_{12} \\ H_{21} & H_{22} \end{bmatrix}, \text{ and}$$

$$G(\theta) = [G_1 \quad G_2]^T$$

where

$$\begin{aligned}
M_{11} &= m_1 k_1^2 + m_2 l_1^2 + m_2 k_2^2 + 2 m_2 l_1 k_2 \cos\theta_2 + I_1 + I_2 \\
M_{12} &= m_2 k_2^2 + m_2 l_1 k_2 \cos\theta_2 + I_2 \\
M_{21} &= m_2 k_2^2 + m_2 l_1 k_2 \cos\theta_2 + I_2 \\
M_{22} &= m_2 k_2^2 + I_2 \\
H_{11} &= -2 m_2 l_1 k_2 \sin\theta_2 \dot{\theta}_2 \\
H_{12} &= -m_2 l_1 k_2 \sin\theta_2 \dot{\theta}_2 \\
H_{21} &= m_2 l_1 k_2 \sin\theta_2 \dot{\theta}_1 \\
H_{22} &= 0 \\
G_1 &= m_1 g k_1 \sin\theta_1 + m_2 g l_1 \sin\theta_1 + m_2 g k_2 \sin(\theta_1+\theta_2) \\
G_2 &= m_2 g k_2 \sin(\theta_1+\theta_2)
\end{aligned}$$

Additionally, with the consideration of the torques caused by disturbance and friction, (1) can further be rewritten as

$$M(\theta)\ddot{\theta} + H(\theta,\dot{\theta})\dot{\theta} + G(\theta) + B = \tau = \tau_m + \tau_d \tag{2}$$

where $\tau_m = [\tau_{m1} \quad \tau_{m2}]^T$ consists of two elements representing the motor torques of the shoulder and the elbow joints, respectively. $\tau_d = [\tau_{d1} \quad \tau_{d1}]$ is the 2×1 disturbance torque vector due to the contact force between the user and the shoulder and elbow joints of the power assisting device, and B=[B_1 B_2] is the 2×1 friction torque vector for the shoulder and elbow joints. Note that in this paper, only the Coulomb friction and viscous friction are taken into account. Moreover, since both Coulomb friction and viscous friction are functions of angular velocities, the friction torque vector B can be denoted as $B(\dot{\theta})$.

B. Parameter Identification of the Dynamic Model of the 2-DOF of the Power Assisting device

What follows is the system identification of the 2-DOF power assisting device employed in this paper. Unlike the traditional approach which needs to identify every system parameter, the barycentric parameters method [24] is adopted such that (2) can be rewritten as

$$\Lambda(\theta_1,\dot{\theta}_1,\ddot{\theta}_1,\theta_2,\dot{\theta}_2,\ddot{\theta}_2)\phi = \tau_m + \tau_d \tag{3}$$

where $\phi = [\phi_1 \quad \cdots \quad \phi_9]^T$ is the barycentric parameter vector containing parameters that form $M(\theta)$, $H(\theta,\dot{\theta})$, $G(\theta)$ and $B(\dot{\theta})$, and some other important elements. Since there is no contact force between the user and the power assisting device during identification, τ_d is set to zero in (3). $\Lambda = [\Lambda_1 \quad \cdots \quad \Lambda_9]^T$ is the identification matrix depending on the angular position, velocity and acceleration of the joint. Each element of ϕ and Λ is listed below:

$$\phi_1 = m_1k_1^2 + m_2l_1^2 + I_1$$
$$\phi_2 = m_2k_2^2 + I_2$$
$$\phi_3 = m_2l_1k_2$$
$$\phi_4 = m_1gk_1 + m_2gl_1$$
$$\phi_5 = m_2gk_2$$
$$\phi_6 = K_{c1}$$
$$\phi_7 = K_{c2}$$
$$\phi_8 = K_{v1}$$
$$\phi_9 = K_{v2}$$
$$\Lambda_1 = [\ddot{\theta}_1 \quad 0]^T$$
$$\Lambda_2 = [\ddot{\theta}_1 + \ddot{\theta}_2 \quad \ddot{\theta}_1 + \ddot{\theta}_2]^T$$
$$\Lambda_3 = \begin{bmatrix} (2\ddot{\theta}_1 + \ddot{\theta}_2)\cos\theta_2 - (2\dot{\theta}_1\dot{\theta}_2 + \dot{\theta}_2^2)\sin\theta_2 \\ \ddot{\theta}_1\cos\theta_2 + \dot{\theta}_1^2\sin\theta_2 \end{bmatrix}$$
$$\Lambda_4 = [\sin\theta_1 \quad 0]^T$$
$$\Lambda_5 = [\sin(\theta_1+\theta_2) \quad \sin(\theta_1+\theta_2)]^T$$
$$\Lambda_6 = [\mathrm{sgn}(\dot{\theta}_1) \quad 0]^T$$
$$\Lambda_7 = [0 \quad \mathrm{sgn}(\dot{\theta}_2)]^T$$
$$\Lambda_8 = [\dot{\theta}_1 \quad 0]^T$$
$$\Lambda_9 = [0 \quad \dot{\theta}_2]^T$$

where K_{C1} and K_{C2} are the Coulomb's friction coefficients for the shoulder and the elbow joints, respectively. K_{v1} and K_{v2} denote the viscous friction coefficients for each joint. sgn(•) is the signum function.

Subsequently, to estimate the elements of ϕ, one can feed a prescribed torque command τ_m to the 2-DOF power assisting device. Measuring the motion data $(\theta_1,\ \dot{\theta}_1,\ \ddot{\theta}_1,\ \theta_2,\ \dot{\theta}_2,\ \ddot{\theta}_2,\ \tau_m)$ at every sampling time instant t_k for a given time interval Δt, one will have

$$A\phi = b \tag{4}$$

where $A = [\Lambda_{(1)}{}^T \quad \Lambda_{(2)}{}^T \quad \cdots \quad \Lambda_{(k)}{}^T \quad \cdots \quad \Lambda_{(n)}{}^T]^T$, $b = [\tau_{m(1)}{}^T \quad \tau_{m(2)}{}^T \quad \cdots \quad \tau_{m(k)}{}^T \quad \cdots \quad \tau_{m(n)}{}^T]^T$, $\Lambda_{(k)}$ and $\tau_{m(k)}$, for $k = 1,2,\cdots,n$, are the identification matrix and the corresponding torque data measured at the sampling time instant t_k, respectively.

The barycentric parameter vector can be estimated using the least square method as in (5), and hence we can estimate $M(\theta)$, $H(\theta,\dot{\theta})$, and $G(\theta)$.

$$\hat{\phi} = (A^TA)^{-1}A^Tb \tag{5}$$

III. CONTROL SCHEME FOR THE POWER ASSISTING DEVICE

A. Control Scheme for Trajectory Following Applications

Performing repetitive trajectory following tasks is commonly seen in the physical exercise/rehabilitation process. Fig. 2 shows the control block diagram for the power assisting device in trajectory following applications, where p_r, $\dot{p}_r$, $\ddot{p}_r \in R^2$ represent the reference position, velocity, and acceleration vectors for the handle of the power assisting device in the Cartesian space, respectively. $\theta_r = [\theta_{r1} \quad \theta_{r2}]^T$, $\dot{\theta}_r$ and $\ddot{\theta}_r \in R^2$ denote the reference angular position, velocity, and acceleration vectors for the joints obtained from inverse kinematics [25], respectively. With the identified system parameters, the well-known computed torque method [26,27] can be exploited in the trajectory following of a power assisting device. As a result, the motor torque τ_m can be expressed as:

$$\tau_m = \hat{M}(\theta)[\ddot{\theta}_r + K_p(\theta_r - \theta) + K_d(\dot{\theta}_r - \dot{\theta})] + \hat{H}(\theta,\dot{\theta})\dot{\theta} + \hat{G}(\theta) + B(\dot{\theta}) - \hat{\tau}_d \tag{6}$$

where $\hat{M}(\theta)$, $\hat{H}(\theta,\dot{\theta})$, $\hat{G}(\theta)$, $B(\dot{\theta})$ and $\hat{\tau}_d$ are the estimations of $M(\theta)$, $H(\theta,\dot{\theta})$, $G(\theta)$, $B(\dot{\theta})$, and τ_d , respectively. In addition,

$$K_p = \begin{bmatrix} K_{p1} & 0 \\ 0 & K_{p2} \end{bmatrix}, \; K_d = \begin{bmatrix} K_{d1} & 0 \\ 0 & K_{d2} \end{bmatrix}$$

where $K_{p1}, K_{p2}, K_{d1}, K_{d2} > 0 \in R$ are the postivie gain constants of the proportional and derivative controllers for the shoulder and the elbow joints of the power assisting device, respectively.

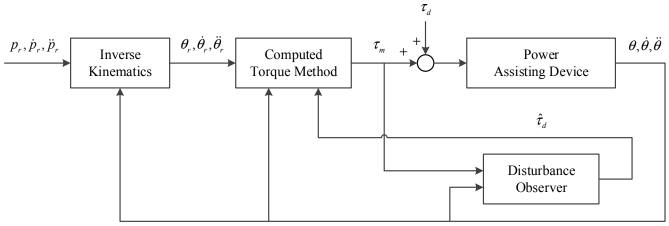

Fig. 2. Control block diagram for the power assisting device in trajectory following applications.

B. Proposed Control Scheme for Exercise/Rehabilitation Applications

Although the control scheme shown in Fig. 2 is effective in trajectory following applications, it is not suitable to be directly used in exercise/rehabilitation applications since it cannot provide proper load/assistance force for the user during exercise or rehabilitation. Fig. 3 shows the block diagram of the proposed control scheme for the power assisting device in exercise/rehabilitation applications, where x_0 , $\dot{x}_0 \in R^2$ denote the initial position and initial velocity of the handle, respectively. $\hat{F}$ refers to the contact force between the user/patient and the device that is either measured by a force sensor or estimated by a disturbance observer. The impedance controller in Fig. 3 aims at controlling the power assisting device to behave like a mass-spring-damper system. The user/patient can use the power assisting device as a load to perform activities such as weight training, aerobic exercise and rehabilitation. As shown in Fig. 3, the impedance controller generates the reference velocity $\dot{p}_r$ of the handle according to the estimated contact force $\hat{F}$ and the initial position and velocity of the handle. By performing inverse kinematics, the reference position, velocity, and acceleration vectors for the handle can be converted into the reference joint position θ_r, reference joint velocity $\dot{\theta}_r$, and reference joint acceleration vectors $\ddot{\theta}_r$. The computed torque controller in Fig. 3 is responsible for guiding the power assisting device to track the reference joint commands. Note that a disturbance observer is proposed to provide the estimated contact force $\hat{F}$ between the user and the power assisting device. Detailed elaborations about the sub-blocks of Fig. 3 such a,s disturbance observer and impedance controller, will be provided in the subsequent sections.

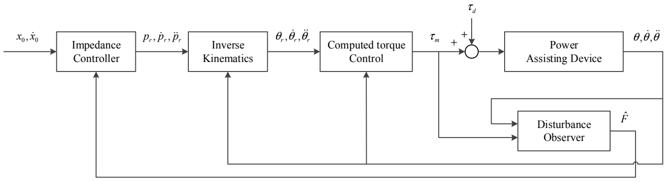

Fig. 3. Block diagram of the proposed control scheme for the power assisting device in exercise/rehabilitation applications.

IV. DISTURBANCE OBSERVER AND CONTACT FORCE ESTIMATION

For the purpose of assisting users/patients to achieve better exercise/rehabilitation performance, it is essential for power assisting devices to perform trajectory following control. Nonetheless, trajectory following performance might be degraded due to the contact force between the user and the device, which is regarded as an external disturbance. In order to effectively suppress the effect of the contact force, a closed-loop disturbance observer [28-30], as illustrated in Fig. 4, is employed in this section. As the figure shows, the proposed disturbance observer is basically composed of the observer gain block and the forward model. The disturbance torque of our interest can be obtained once the outputs of both the real system and the forward model coincide with each other, and the contact force between the user and the power assisting device can be estimated accordingly.

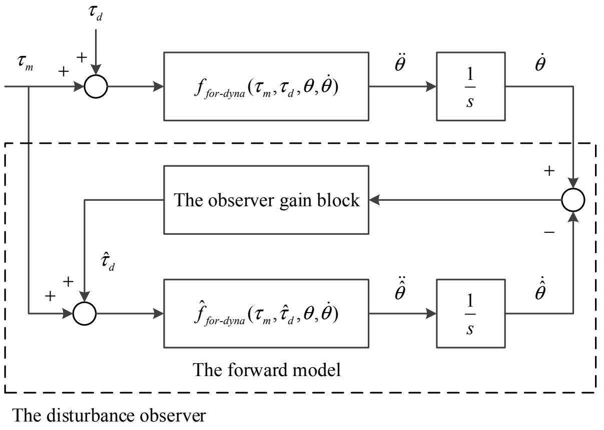

Fig. 4. Closed-loop disturbance observer

Without the loss of generality, suppose that the variation of τ_d with respect to time is small. That is, $\dot{\tau}_d \cong 0$. Then, the observer gain block designed to exponentially converge the estimation error of disturbance torque to zero can be described by

$$\dot{\hat{\tau}}_d = K_o \hat{M}(\theta)(\ddot{\theta} - \ddot{\hat{\theta}}) \tag{7}$$

where $K_o = \begin{bmatrix} K_{o1} & 0 \\ 0 & K_{o2} \end{bmatrix}$ and K_{o1} , $K_{o2} > 0 \in R$ are the observer gains for the shoulder and elbow joints, respectively.

As one can see, acquiring the acceleration data of the real system is essential when using (7) to implement the disturbance observer directly. Nevertheless, in practice such data are susceptible to noise due to the measurement error of the joint position by the encoder. To cope with this problem, we can take advantage of the idea of "integration by part" to rewrite (7) as follows such that no real acceleration data are required.

$$\int K_o \hat{M}(\theta)(\ddot{\theta} - \ddot{\hat{\theta}})dt = K_o \hat{M}(\theta)(\dot{\theta} - \dot{\hat{\theta}}) - \int K_o \dot{\hat{M}}(\theta)(\dot{\theta} - \dot{\hat{\theta}})dt$$

As a result, the estimated disturbance torque can be calculated with (8) as an alternative.

$$\hat{\tau}_d = K_o \hat{M}(\theta)(\dot{\theta} - \dot{\hat{\theta}}) - \int K_o \dot{\hat{M}}(\theta)(\dot{\theta} - \dot{\hat{\theta}})dt \tag{8}$$

where

$$\dot{\hat{M}}(\theta) = \frac{\partial \hat{M}(\theta)}{\partial \theta_1}\dot{\theta}_1 + \frac{\partial \hat{M}(\theta)}{\partial \theta_2}\dot{\theta}_2$$

$$\frac{\partial \hat{M}(\theta)}{\partial \theta_1} = \begin{bmatrix} 0 & 0 \\ 0 & 0 \end{bmatrix}$$

$$\frac{\partial \hat{M}(\theta)}{\partial \theta_2} = \begin{bmatrix} -2m_2 l_1 k_2 \sin\theta_2 & -m_2 l_1 k_2 \sin\theta_2 \\ -m_2 l_1 k_2 \sin\theta_2 & 0 \end{bmatrix}$$

The contact force between the user and the power assisting device can then be estimated using (9):

$$\hat{F} = f_{inv-sta}(\hat{\tau}_d, \theta) = \begin{cases} J^{T^{-1}}(\theta)\hat{\tau}_d \ , \ \theta_2 \neq 0 \\ [\hat{F}_x(\hat{\tau}_d, \theta) \quad \hat{F}_y(\hat{\tau}_d, \theta)]^T \ , \ \theta_2 = 0 \end{cases} \tag{9}$$

where $\hat{F}_x = -\dfrac{\sin\theta_1}{l_1 + l_2}\hat{\tau}_{d1}$, $\hat{F}_y = \dfrac{\cos\theta_1}{l_1 + l_2}\hat{\tau}_{d1}$, and $J(\theta)$ is the Jacobian matrix which is given by

$$J(\theta) = \frac{\partial f_{for-kine}(\theta)}{\partial \theta} = \begin{bmatrix} -l_1 \sin\theta_1 - l_2 \sin(\theta_1 + \theta_2) & -l_2 \sin(\theta_1 + \theta_2) \\ l_1 \cos\theta_1 + l_2 \cos(\theta_1 + \theta_2) & l_2 \cos(\theta_1 + \theta_2) \end{bmatrix}.$$

Fig. 5 illustrates the proposed disturbance/contact force observer that exploits the idea of integration by parts. It is worthy to note that the forward model in Fig. 5 can be derived using the forward dynamics obtained from (2) as follows.

$$\begin{aligned} \ddot{\hat{\theta}} &= \hat{f}_{for-dyna}(\tau_m, \hat{\tau}_d, \theta, \dot{\theta}) \\ &= \hat{M}^{-1}(\theta)[\tau_m + \hat{\tau}_d - \hat{H}(\theta, \dot{\theta})\dot{\theta} - \hat{G}(\theta) - \hat{B}(\dot{\theta})] \end{aligned} \tag{10}$$

$$\dot{\hat{\theta}} = \int \ddot{\hat{\theta}} dt \tag{11}$$

$$\hat{\theta} = \int \dot{\hat{\theta}} dt \tag{12}$$

where $\hat{\theta} = [\hat{\theta}_1 \quad \hat{\theta}_2]^T$, $\dot{\hat{\theta}}$, and $\ddot{\hat{\theta}} \in R^2$ denote the angular position, velocity, and acceleration of the joints in the forward model, respectively.

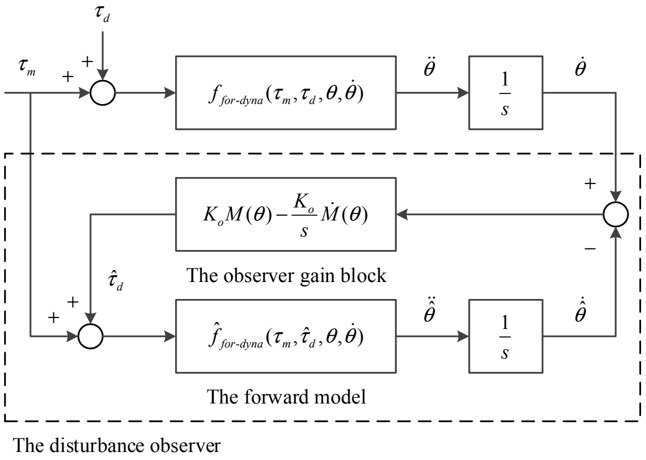

Fig. 5. The proposed disturbance/contact force observer exploits the idea of integration by parts.

V. IMPEDANCE CONTROL OF THE POWER ASSISTING DEVICE

Impedance control is often adopted in power assisting devices to regulate the force of the user and the position of the handle to satisfy a certain relationship, so as to help the user perform autonomous motions and achieve better exercise and rehabilitation outcomes.

In general, fitness can be divided into categories such as weight training and aerobic exercise. The purpose of weight training is to increase muscle strength so that the user/patient can produce high force output. In contrast, the purpose of aerobic exercise is to consume calories and burn energy; namely, the user/patient is required to generate high power output. In order to let the user/patient generate the proper amount of force or power during exercise/rehabilitation, appropriate loads need to be provided so that the generated force, velocity and acceleration satisfy specific relationships.

A. Load for Weight Training

As is often the case, mass and spring are commonly used as loads during weight training since they can convert and store the mechanical energy produced by muscles into gravity potential or spring potential, and later deliver the energy back to the muscles. As pointed out by Hortobagyi [31], if an exercise involves concentric contraction and eccentric contraction of muscles, better muscle strength can be achieved. This can probably explain why using mass or spring as loads during weight training can have better fitness outcomes.

Biceps training and shoulder muscle training are two of the most commonly used weight training modes. In biceps training, the user holds the mass by hand and the upper arm is hanging, while the elbow performs flexion and extension as shown in Fig. 6(a). In shoulder muscle training, the user holds the spring by hand and bends the arm so that the spring is pulled horizontally to the shoulder as shown by Fig. 6 (b).

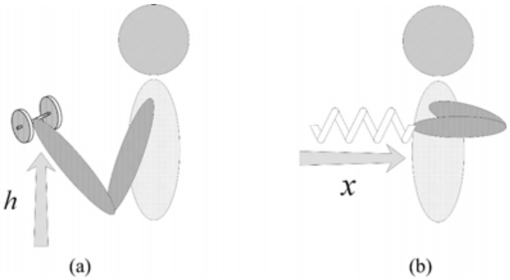

Fig. 6 Two commonly used weight training types (a) biceps training; (b) shoulder muscle training

Although high force output and a large amount of energy releasing/receiving by muscle can effectively increase muscle strength, excessive energy releasing/receiving by muscles or excessive force output may lead to sports injury. Therefore, selection of the proper amount of mass and a spring wit suitable stiffness is paramount for weight training.

In biceps training, the force needed in lifting the mass i $F=Mg$, while the required energy is $E=Mgh$, where M is th mass, g is the gravitational constant, and h is the lift heigh Suppose that the maximum force output generated by the use is $\widehat{F}$, the maximum energy released/received by muscle during a single lift is $\widehat{E}$, and the maximum lift height i denoted as $\widehat{h}$. One can design the suitable values of mass and lift height to satisfy the constraints/limits on force output, energy and lift height as follows: If $\widehat{E} / \widehat{F} \leq \widehat{h}$, then the mass M can be designed as $M = \widehat{F} / g$ and the lift height h can be designed as $h = \widehat{E} / \widehat{F}$; otherwise, M is designed as $M = \widehat{F} / g$ and h is designed as $h = \widehat{h}$.

In shoulder muscle training, the force required to pull/push a spring is designed as $F=k\Delta x$ and the needed energy is $E = k(\Delta x)^2 / 2$, where k and Δx are the stiffness coefficient and the extension displacement of the spring, respectively. Suppose that the maximum force output generated by the user is $\widehat{F}$, the maximum energy released/received by muscles during a single pulling/pushing is $\widehat{E}$, and the maximum extension displacement is denoted as $\Delta\widehat{x}$. The stiffness coefficient and extension displacement of the spring can be designed to satisfy the constraints on force output, energy and extension displacement as follows: If $2\widehat{E} / \widehat{F} \leq \Delta\widehat{x}$, then k can be designed as $k = \widehat{F}^2 / (2\widehat{E})$, and Δx can be designed as $\Delta x = 2\widehat{E} / \widehat{F}$; otherwise, k is designed as $k = \widehat{F} / \Delta\widehat{x}$ and Δx is designed as $\Delta x = \Delta\widehat{x}$.

B. Load for Aerobic Exercise

In general, a damper is commonly used in aerobic exercise as a load to consume the energy released by muscles. As shown in Fig. 7, in aerobic exercise, the user holds the damper by hand and performs a repetitive motion by repeatedly pushing the damper forward and backward in a horizontal direction. By choosing a damper with a proper damping coefficient so that the damper can consume the maximal energy in aerobic exercise, optimal fitness results can be achieved. The relationship between the maximum force $F_{\max}$ generated by muscles and the motion speed $|\dot{x}|$ can be described by the so-called Hill's muscle model [14,32]. In order to facilitate the analysis, this paper uses a straight line to approximate the Hill's muscle model, in which $F_{\max} = F_0 - b_0|\dot{x}|$, where F_0 is the maximum force generated when $|\dot{x}|=0$, and b_0 is a positive constant.

Imagine that if force is analogous to voltage and motion speed is analogous to current, then muscle can be analogous to an ideal voltage source in series with a resistor. The mechanism of the motion in which a user tries to push the damper with the maximum force can be transformed into an electric circuit shown in Fig. 8, where b is the damping coefficient. Based on the maximum power transfer theorem, when $b=b_0$, the damper has the maximum power consumption $F_0^2 / (4b_0)$, and the orresponding exercise speed is $F_0 / (2b_0)$. As a result, b is set o b_0 in this paper to satisfy the requirement of maximum power onsumption. The value of b_0 can be determined by the pen-circuit test and short-circuit test. 1) open-circuit test: The ser exerts the maximum force to push a fixed load. In this case, he force output is F_0. 2) short-circuit test: Under no load ondition, the user exerts the maximum force F_0 when xercising. In this case, b_0 is equal to F_0 divided by the current peed.

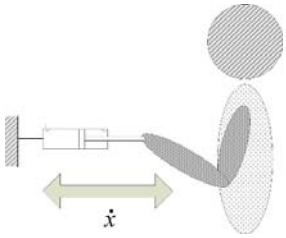

Fig. 7 Aerobic exercise.

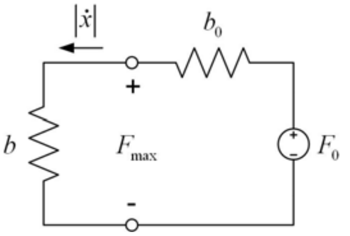

Fig. 8 Equivalent circuit for aerobic exercise.

C. Load for Early Stage of Rehabilitation

Rehabilitation therapy is composed of the early stage and later stage. In general, at the early stage of rehabilitation, the patient needs some assistance force from the power assisting device, since he/she only has partial muscle strength due to stroke or injury. In contrast, at the later stage of rehabilitation, the patients are able to move by themselves to regain normal muscle strength. A better approach for the early stage of rehabilitation is that the rehabilitation therapist indirectly leads the patient to perform prescribed motions through the spring. As such, the spring can provide large assistance force only when the difference between the action of the patient and the desired action is large. By selecting a spring with proper stiffness, suitable assistance force can be provided to the patient.

In particular, the assistance force provided by the spring is $F = k\Delta x$, where k is the stiffness coefficient of the spring and Δx is the extension distance of the spring. Suppose that the total moving distance for a set of motions is x, namely the difference between the action of the patient and the desired one is smaller than x. Also assumes that the maximum assistance force is $\widehat{F}$. Therefore, the stiffness coefficient k of the spring can be designed as $k = \widehat{F} / x$ to satisfy the constraints on the maximum assistance force. As for the later stage of the rehabilitation, the therapy is very similar to that in aerobic exercise.

For all the scenarios described above, this paper develops an impedance controller for the power assistance device such that the user/patient can use the device as the load to perform the aforementioned weight training, aerobic exercise and rehabilitation therapy.

D. Impedance Controller Design

The impedance controller developed in this paper is based on the idea of the mass-spring-damper system illustrated in Fig. 9, in which the relationship between the motion command of the handle of the power assisting device and the contact force is described by (13):

$$F = M_z(\ddot{p}_r - g_z) + B_z(\dot{p}_r - \dot{x}_0) + K_z(p_r - x_0) \tag{13}$$

where M_z, B_z and $K_z \in R^{2\times2}$ are the diagonal mass, damping and stiffness coefficient matrices, respectively. $F \in R^2$ is the contact force vector and $g_z \in R^2$ is the gravity acceleration vector. In particular,

$$M_z = \begin{bmatrix} M_x & 0 \\ 0 & M_y \end{bmatrix},\ B_z = \begin{bmatrix} B_x & 0 \\ 0 & B_y \end{bmatrix},\ K_z = \begin{bmatrix} K_x & 0 \\ 0 & K_y \end{bmatrix}$$

$$F = [F_x \quad F_y]^T,\ x = [x_x \quad x_y]^T,\ x_0 = [x_{0x} \quad x_{0y}]^T,$$

$$g_z = [g_x \quad g_y]^T$$

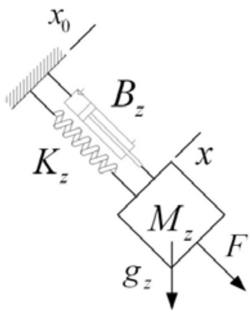

Fig. 9. The mass-spring-damper system.

In this paper, the disturbance observer illustrated in Fig. 5 is used to estimate the contact force between the user and the device. As shown in Fig. 3, with the estimated contact force and the values of x_0 and $\dot{x}_0$ given, based on (13), the impedance controller can be designed as follows;

$$\ddot{p}_r = M_z^{-1}[F - B_z(\dot{p}_r - \dot{x}_0) - K_z(p_r - x_0)] + g_z \tag{14}$$

$$\dot{p}_r = \int \ddot{p}_r dt \tag{15}$$

$$p_r = \int \dot{p}_r dt\,. \tag{16}$$

Note that B_z, and K_z cannot both be zero matrices. Moreover, in order to let the user do exercise or rehabilitation more smoothly, some constraints on acceleration may be required; that is, M_z can be designed such that M_z^{-1} exists. By exploiting inverse kinematics, the calculated p_r, $\dot{p}_r$, $\ddot{p}_r$ are converted into the reference joint angle θ_r, reference joint velocity $\dot{\theta}_r$, and reference joint acceleration $\ddot{\theta}_r$, respectively.

VI. EXPERIMENTAL RESULTS

A. Experimental Setup

The photograph of the experimental platform for the developed power assisting device is shown in Fig. 10, where the servomotors installed at the shoulder and the elbow joints of the power assisting device provide assistance force to the user. In addition, the gear boxes are used to increase the torque of the servomotor while reducing its speed. Moreover, as a reference to assess the accuracy of the force estimated by the proposed disturbance/contact force observer, a force sensor is mounted on the handle to measure the contact force that the user exerts on the device. In particular, the resolutions of the encoders are 10000 and 4096 pulses per revolution for the servomotors installed at the shoulder joint and elbow joint, respectively. Furthermore, the gear ratios of the gearboxes are 50:1 and 113:1, individually. The user/patient will hold the handle to do either exercise or rehabilitation as shown in Fig. 11.

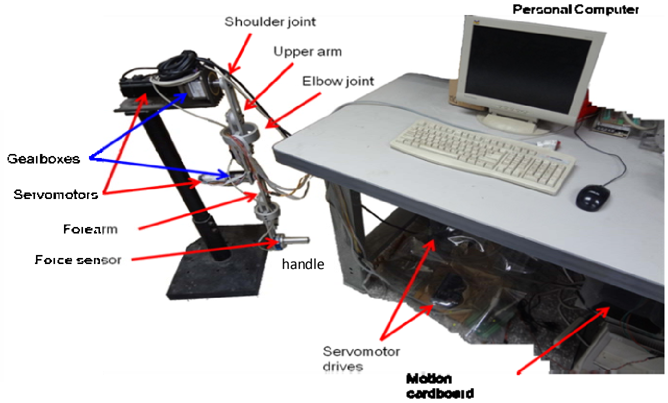

Fig. 10. Photograph of the experimental platform for arm exercise and rehabilitation developed in this paper.

Fig. 11. The user/patient holds the handle of the power assisting device to do either exercise or rehabilitation.

B. System Parameter Identification

In order to perform system identification, first of all, let τ_m have the following form:

$$\tau_m = \begin{bmatrix} 100 & 0 \\ 0 & 80 \end{bmatrix}(\theta_r - \theta) + \begin{bmatrix} 10 & 0 \\ 0 & 8 \end{bmatrix}(\dot{\theta}_r - \dot{\theta}) \quad (17)$$

where $\theta_r = [\theta_{r1} \quad \theta_{r2}]^T$ is set as follows.

$$\theta_{r1} = \frac{\pi}{4}[\sin(\pi t - \frac{\pi}{2}) + 1]$$
$$\theta_{r2} = \frac{\pi}{4}[\sin(0.9\pi t - \frac{\pi}{2}) + 1]$$

The barycentric parameters can be computed with (4) and (5) as shown below, and $M(\theta)$, $H(\theta, \dot{\theta})$ and $G(\theta)$ can thus be estimated:

$$\phi = [0.4924 \quad 0.1873 \quad 0.1625 \quad 13.6250 \quad 4.4026 \quad 2.9917 \quad 0.9851 \quad 1.5113 \quad 0.5013]^T$$

With the estimated $\hat{M}(\theta)$, $\hat{H}(\theta,\dot{\theta})$, $\hat{G}(\theta)$, the proposed disturbance observer, the impedance controller and the computed torque controller can be implemented.In particular, the following parameter settings for the proposed disturbance observer are used throughout the experiments: $K_{o1} = 30$, and $K_{o2} = 30$. The formulas for calculating Root Mean Square Error (RMSE) and Mean of Absolute Error (MAE) are shown in the following:

$$RMSE = \sqrt{\frac{1}{N}\sum_{i=1}^{N} e_i^2}\ , MAE = \frac{1}{N}\sum_{i=1}^{N}|e_i|$$

where e_i is the error at the ith sampling time, and N is the total number of the sampling time.

C. Verification of Disturbance Observer and Contact Force Estimation

In order to verify the effectiveness of the proposed disturbance observer described by (8), let τ_m have the same form as in (17). Additionally, the reference positions of the shoulder and the elbow joints are set as

$$\theta_{r1} = \frac{\pi}{4}[\sin(0.5\pi t - \frac{\pi}{2}) + 1]$$
$$\theta_{r2} = \frac{\pi}{4}[\sin(0.45\pi t - \frac{\pi}{2}) + 1].$$

Also, suppose in the experiment, the disturbances that are intentionally added to the shoulder and the elbow joints have the following forms:

$$\tau_{d1} = -10\sin(0.25\pi t) \quad (18)$$
$$\tau_{d2} = 5\sin(0.25\pi t). \quad (19)$$

The estimation results shown in Table 2 and Fig. 12 indicate that the estimated disturbances approximate the given disturbances, which verifies the efficacy of the proposed disturbance observer. Subsequently, input the disturbance provided by the user (i.e. the user holds the handle and executes some tasks) into the proposed disturbance observer and calculate the contact force using (9). The results shown in Fig. 13 and Table 2 indicate that the observer estimates well the contact force that the user exerts onto the device (the real contact force is measured by the force sensor mounted on the handle; for verification only).

TABLE II
ERROR INDEX FOR DISTURBANCE ESTIMATION USING THE PROPOSED APPROACH

	Shoulder joint		Elbow joint	
	RMSE(N·m)	MAE(N·m)	RMSE(N·m)	MAE(N·m)
Estimation error	1.2336	1.0407	0.5192	0.3939

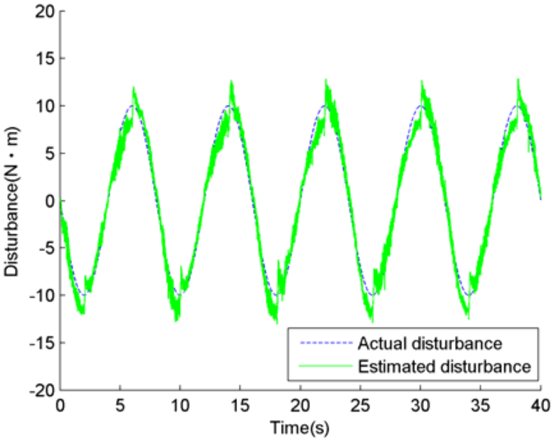

(a)

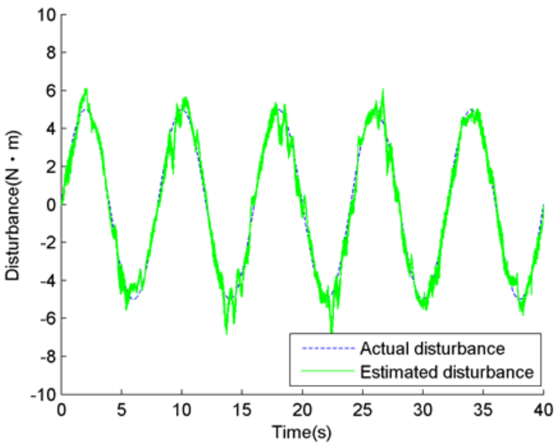

(b)

Fig. 12. Disturbance estimation using the proposed disturbance observer: (a) Shoulder joint of the power assisting device; (b) Elbow joint of the power assisting device.

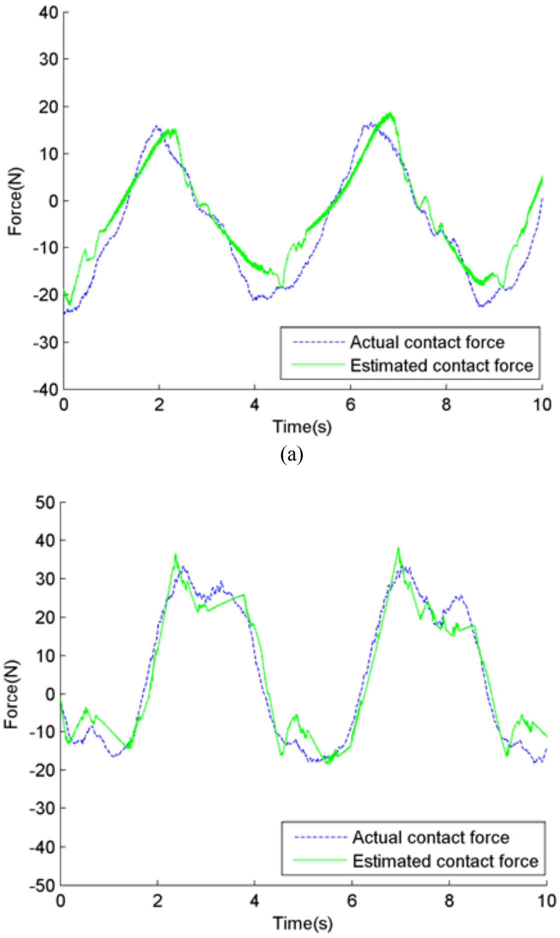

(a)

(b)

Fig. 13. Contact force estimation: (a) X component; (b) Y component.

TABLE III
Error Index for Contact Force Estimation

	X component		Y component	
	RMSE(N)	MAE(N)	RMSE(N)	MAE(N)
Estimation error	2.4640	1.1788	2.5001	1.2371

D. *Impedance Control Experiment*

1) *Biceps Muscle Training*

In biceps muscle training, the user/patient holds the handle and lifts it up in a vertical direction (i.e. upward or downward). Assume that the maximum force that the user can generate during biceps muscle training is $F=Mg=40$ N. In addition, the maximum energy the muscles of the user can release/absorb each time is $E=Mgh=10$ Joules. The lift height h each time can then be obtained from the formula: $h=E/F=10/40=0.25$ m. Also, given the gravitational acceleration $g_z = [10 \quad 0]^T$ m/s^2, the mass M_z in the impedance control is 4 kg (i.e. $M_x=M_y= 4$ kg). Furthermore, other relevant parameters are set as follows: $B_x=B_y=50$ N·s/m, $K_x=K_y=0$ N/m, $x_0 = [0.45 \quad 0.4]^T$ m, and $\dot{x}_0 = [0 \quad 0]^T$ m/s.

Next, let the user lift the handle from (0.45, 0.4) m to (0.2, 0.4) m. The contact force that the user exerts on the handle is measured by the force sensor, while the released energy of the muscles is computed by the following formula:

$$E = \int F_x \dot{x}_p dt \; . \tag{20}$$

Experimental results shown in Fig. 14 indicate that both the real contact force and the calculated maximal energy meet what we set as the prescribed requirements.

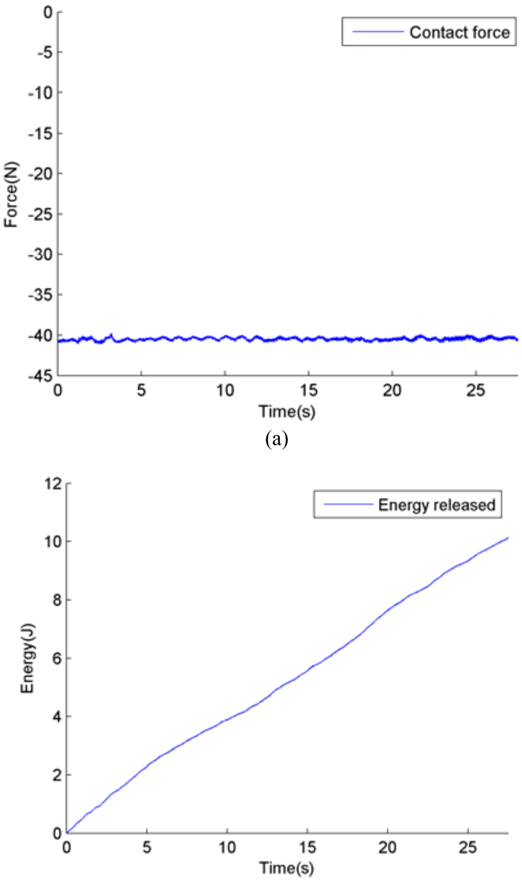

(a)

(b)

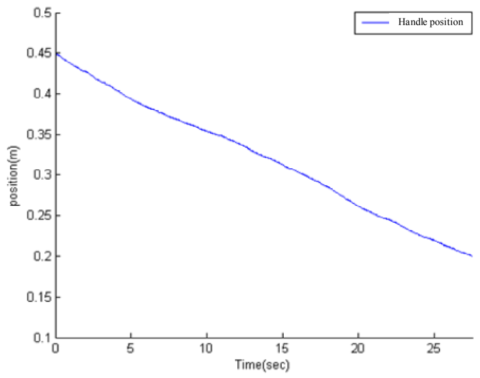

(c)

Fig. 14. Experimental results for biceps muscle training: (a) X component of the contact force; (b) Energy the user releases; (c) Position of the handle.

2) *Shoulder Muscle Training*

In the shoulder muscle training, the user/patient holds the handle and moves it in a horizontal direction. Assume that the maximum force that the user can generate during biceps muscle training is $F=k\Delta x=40$ N. Suppose that the stiffness coefficient is set to $k=k_x=k_y=80$ N/m. As a result, each time the user stretches out the handle (behaves like a spring), the moving distance of every stretch is set to $\Delta x=F/k=0.5$ m. The maximum energy the muscles of the user can release/absorb is $E=k(\Delta x)^2/2=10$ Joules, accordingly. Besides, the parameters in (13) and (14) are set as follows: $M_x=M_y=4$ kg, $B_x=B_y=50$ N·s/m, $K_x=K_y=80$ N/m, $g_z = [0 \quad 0]^T$ m/s^2, $x_0 = [0.2 \quad 0.2]^T$ m, and $\dot{x}_0 = [0 \quad 0]^T$ m/s.

Next, let the user stretch out the handle from (0.2, 0.2) m to (0.2, 0.7) m, and the contact force that the user exerts on the handle as well as the energy the muscles releases are recorded. The energy released is computed using the following formula:

$$E = \int F_y \dot{y}_p dt . \tag{21}$$

As shown in Fig. 15, experimental results suggest that the maximum force and energy constraints can be satisfied as expected.

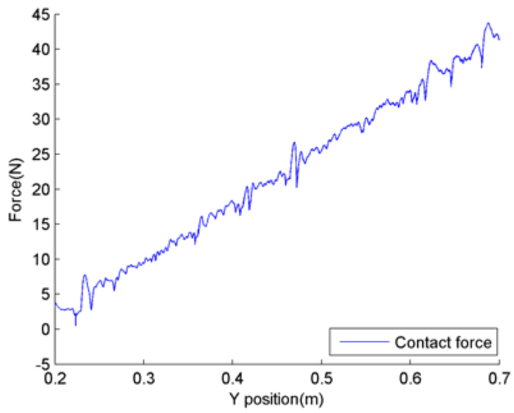

(a)

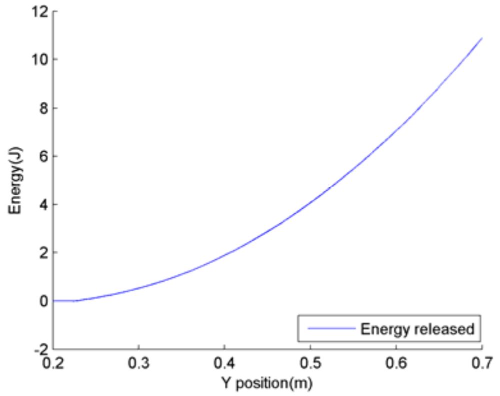

(b)

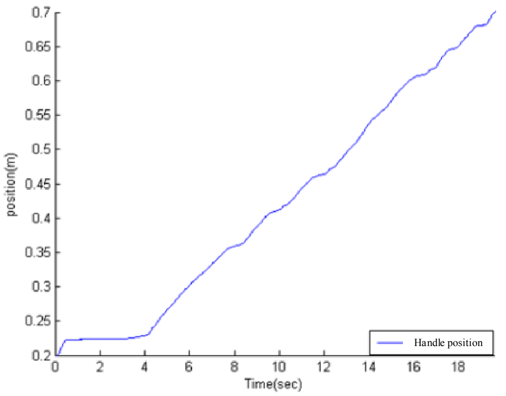

(c)

Fig. 15. Experimental results for shoulder muscle training: (a) Y component of the contact force; (b) Energy the user releases; (c) Position of the handle.

3) *Simulated Scenario of Therapy for Patients at the Early Stage of Rehabilitation*

In general, at the early stage of rehabilitation, the patient needs some assistance force from the power assisting device, since the patient only has partial muscle strength due to stroke or injury. In the experiment, to simulate the scenario of therapy for patients at the early stage of rehabilitation, a 25-year-old healthy male user is instructed to hold the handle and move the handle along a pre-designed trajectory. Suppose that the maximum assistance force $\widehat{F}$ is limited to 20 N, and the total moving distance x of the handle is 0.5 m. Moreover, the pre-designed trajectory and velocity for the handle is $x_0 = [0.2 \quad 0.45+0.25\sin(0.25\pi t)]^T$ m, and $\dot{x}_0 = [0 \quad 0.25^2\pi\cos(0.25\pi t)]^T$ m/s. In addition, the parameters in (13) and (14) are set as follows: $K_x=K_y=40$ N/m, $M_x=M_y=4$ kg, $B_x=B_y=20$ N·s/m, $g_z = [0 \quad 0]^T$ m/s^2.

The results shown in Fig. 16 indicate that the parameter settings of the power assisting device developed in this paper can provide a suitable amount of assistance force to the user such that the handle of the power assisting device can move along the pre-designed trajectory; this satisfies the needs of patients at the early stage of rehabilitation.

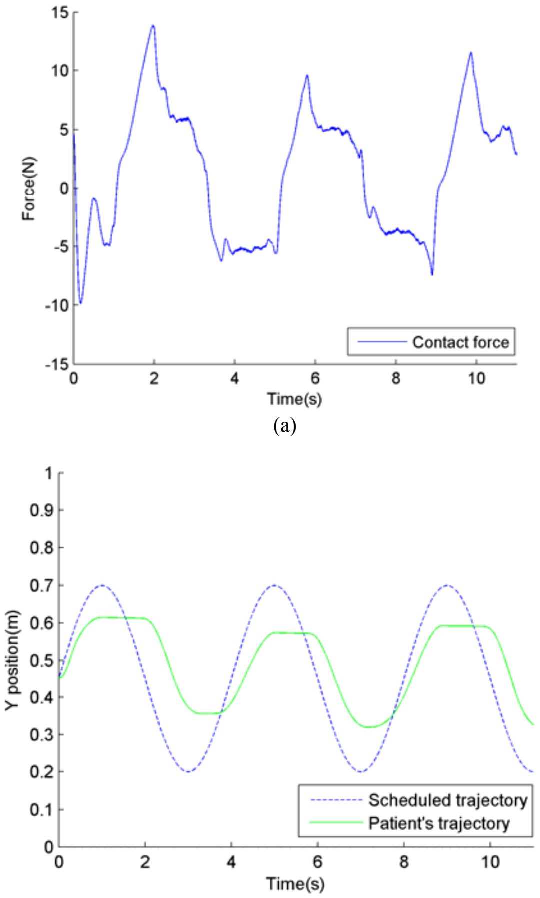

(a)

(b)

Fig. 16. Experimental results for simulated scenario of therapy for patients at the early stage of rehabilitation: (a) Y component of the contact force; (b) Y coordinate of the handle.

VII. CONCLUSIONS

This paper has focused on exploiting observer-based impedance control in a power assisting device so that the proper amount of assistance force or load can be provided. In particular, a disturbance observer is proposed to estimate the contact force between the user and the power assisting device, and therefore compensate for such disturbances. The idea of "integration by part" has been exploited to implement the disturbance observer. Based on the torque/contact force information estimated from the disturbance observer, the impedance control scheme is adopted to calculate the proper amount of assistance force or load for different application scenarios such as weightlifting, aerobic exercise and rehabilitation. Experimental results have shown that the proposed control scheme exhibits satisfactory performance.

The proposed integration-by-parts contact force estimation method belongs to the category of observer-based disturbance estimation approaches. However, one of the well-known disadvantages of observer-based disturbance estimation approaches is that they are sensitive to modeling errors. The proposed integration-by-parts contact force estimation method is no exception and is only suitable for applications with accurate system models. As a result, how to extend the use of the proposed method to more complex systems with modeling errors is an issue deserving more investigation.

VIII. ACKNOWLEDGMENTS

The authors would like to thank the National Science Council of Taiwan for support of this research under Grant NSC99-2221-E-006-204-MY2, and also thank the Ministry of Economic Affairs of Taiwan for support of this research under Grant MOEA101- EC-17-A-05- S1-192.

REFERENCES

[1] http://world.honda.com/Walking-Assist/.

[2] T. Noritsugu and T. Tanaka, "Application of rubber artificial muscle manipulator as a rehabilitation robot," *IEEE/ASME Trans. Mechatron.*, vol. 2, no. 4, pp. 259–267, Dec. 1997.

[3] Y. Choi, J. Gordon, D. Kim, and N. Schweighofer, "An Adaptive Automated Robotic Task-Practice System for Rehabilitation of Arm Functions After Stroke," *IEEE Trans. Robot.*, vol. 25, no. 3, pp. 556–568, Jun. 2009.

[4] K. Kong, H. Moon, B. Hwang, D. Jeon, and M. Tomizuka, "Robotic rehabilitation treatments: Realization of aquatic therapy effects in exoskeleton systems," in *Proc. IEEE Int. Conf. Robot. Autom.*, 2009, pp. 1923–1928.

[5] B. Hwang, H. Moon, and D. Jeon, "Monitoring method of interactive torque between human and robot in exoskeleton systems," in *Proc. IEEE Int. Conf. Rehabil. Robot.*, 2009, pp.283–288.

[6] S. Komada, Y. Hashimoto, N. Okuyama, T. Hisada, and J. Hirai, "Development of a Biofeedback Therapeutic-Exercise-Supporting Manipulator," *IEEE Trans. Ind. Electron.*, vol. 56, no. 10, pp. 3914–3920, Oct. 2009.

[7] A. Duschau-Wicke, J. von Zitzewitz, A. Caprez, L. Lunenburger, and R. Riener, "Path Control: A Method for Patient-Cooperative Robot-Aided Gait Rehabilitation," *IEEE Trans. Neural Syst. Rehabil. Eng.,* vol. 18, no. 1, pp. 38–48, Feb. 2010.

[8] S. Ito, H. Kawasaki, Y. Ishigure, M. Natsume, T. Mouri, and Y. Nishimoto, "A design of fine motion assist equipment for disabled hand in robotic rehabilitation system," *Journal of the Franklin Institute*, vol. 348, no. 1, pp. 79–89, Feb. 2011.

[9] C. T. Freeman, E. Rogers, A. M. Hughes, J. H. Burridge, and K. L. Meadmore, "Iterative learning control in health care: Electrical stimulation and robotic-assisted upper-limb stroke rehabilitation," *IEEE Control. Syst. Mag.*, vol. 32, pp. 18–43, Feb. 2012.

[10] A. U. Pehlivan, F. Sergi, and M. K. O'Malley, "A Subject-Adaptive Controller for Wrist Robotic Rehabilitation," *IEEE/ASME Trans. Mechatron.*, vol. 20, no. 3, pp. 1338–1350, Jun. 2015.

[11] W. Meng, Q. Liu , Z. Zhou,Q. Ai,B. Sheng, S. Xie, "Recent development of mechanisms and control strategies for robot-assisted lower limb rehabilitation," *Mechatron*., vol.31, pp. 132–145,Oct. 2015.

[12] J. Wu, J. Gao, R. Song, R. Li, Y. Li, L. Jiang, "The design and control of a 3DOF lower limb rehabilitation robot," *Mechatron*., vol.33, pp. 13–22, Feb. 2016.

[13] T. Madani, B. Daachi, K. Djouani, "Non-singular terminal sliding mode controller Application to an actuated exoskeleton. " *Mechatron*.,vol.33, pp. 136–145, Feb. 2016.

[14] P. Y. Li and R. Horowitz, "Control of smart exercise machines-Part I : problem formulation and nonadaptive control," *IEEE/ASME Trans. Mechatron.*, vol. 2, no. 4, pp. 237–247, Dec. 1997.

[15] P. Y. Li and R. Horowitz, "Control of smart exercise machines. II. Self-optimizing control," *IEEE/ASME Trans. Mechatron.*, vol. 2, no. 4, pp. 248–258, Dec. 1997.

[16] T. Kiryu and K. Yamashita, "A Ubiquitous Wearable Unit for Controlling Muscular Fatigue During Cycling Exercise Sessions," in *Proc. IEEE Int. Conf. on EEBS*, 2007, pp.4814–4817.

[17] C.-J. Chen, M.-Y. Cheng and K.-H. Su, "Observer-based impedance control and passive velocity control of power assisting devices for exercise and rehabilitation," in *Proc. IEEE Int. Conf. Ind. Electron.*, 2013, pp. 6502-6507.

[18] A. A. Blank, A. M. Okamura and L. L. Whitcomb, "Task-dependent impedance and implications for upper-limb prosthesis control," *The International Journal of Robotics Research*, vol. 33, no. 6, pp. 827–846, Feb. 2014.

[19] M. Cestari, D. Sanz-Merodio, J. C. Arevalo, and E. Garcia, "An Adjustable Compliant Joint for Lower-Limb Exoskeletons," *IEEE/ASME Trans. Mechatron.*, vol. 20, no. 2, pp. 889–898, April 2015.

[20] A. Calanca, R. Muradore, and P. Fiorini, "A Review of Algorithms for Compliant Control of Stiff and Fixed-Compliance Robots," *IEEE/ASME Trans. Mechatron.*, vol. 21, no. 2, pp. 613–624, April 2016.

[21] J. Zhang and C. C. Cheah, "Passivity and Stability of Human–Robot Interaction Control for Upper-Limb Rehabilitation Robots." *IEEE Trans. Robot.*, vol. 31, no. 2, pp. 233–245, April 2015.

[22] S. A. Bowyer, and F. R. y Baena, "Dissipative Control for Physical Human–Robot Interaction," *IEEE Trans. Robot.*, vol. 31, no. 6, pp. 1281–1293, Dec. 2015.

[23] W. N. White, D. D. Niemann, and P. M. Lynch, "The presentation of Lagrange's equations in introductory robotics courses," *IEEE Transactions on Education*, vol. 32, no. 1, pp. 39–46, Feb. 1989.

[24] J. Swevers, W. Verdonck, and J. D. Schutter, "Dynamic Model Identification for Industrial Robots," *IEEE Control Systems Magazine*, vol. 27, no. 5, pp. 58–71, Oct. 2007

[25] L. Sciavicco and B. Siciliano, "A solution algorithm to the inverse kinematic problem for redundant manipulators," *IEEE Trans Robot. Autom.*, vol. 4, no. 4, pp. 403–410, Aug. 1988.

[26] J. Luh, M. Walker, R. Paul, "Resolved-acceleration control of mechanical manipulators," *IEEE Transactions on Automatic Control*, vol. 25, no. 3, pp. 468–474, Jun. 1980.

[27] J. J. E. Slotine and W. Li, *Applied Nonlinear Control*. Prentice Hall, 1991.

[28] E.-C. Tseng, M.-Y. Cheng, and M.-C. Tsai, "Design of a PI-type torque observer for detecting abnormal load," in *Proceedings of the 1998 International Conference on Mechatronics Technology*, 1998, pp. 147–152.

[29] M.-C. Tsai, E.-C. Tseng, and M.-Y. Cheng, "Design of a torque observer for detecting abnormal load," *Control Engineering Practice*, vol. 8, pp. 259–269, Mar. 2000.

[30] W.-H. Chen, D. J. Ballance, P. J. Gawthrop, and J. O'Reilly, "A nonlinear disturbance observer for robotic manipulators," *IEEE Trans. Ind. Electron.*, vol. 47, no. 4, pp. 932–938, Aug. 2000.

[31] T. Hortobagyi, "The positives of negatives: clinical implications of eccentric resistance exercise in old adults," *Journal of Gerontology, Series A, Biological Sciences and Medical Sciences*, vol. 58, no. 5, pp. 417–418, May 2003.

[32] A. Hill, "The heat of shortening and the dynamic constants of muscle," *Proceedings of the Royal Society of London. Series B, Biological Sciences*, vol. 126, no.843, pp.136–195, 1938.

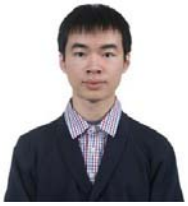

Chao-Jen Chen was born in Taiwan, in 1988. He received a B.S. degree in Electrical Engineering from the National Cheng-Kung University, Taiwan, in 2011. He received an M.S. degree in Electrical Engineering from the National Cheng-Kung University, Taiwan, in 2013. He is currently an engineer with Catcher Technology Co., Ltd., Taiwan. His research interests include motion control, mechatronics and machine vision.

Ming-Yang Cheng was born in Taiwan in 1963. He received the B.S. degree in control engineering from National Chiao Tung University, Hsinchu, Taiwan, in 1986, and M.S. and Ph.D. degrees in electrical engineering from the University of Missouri, Columbia, in 1991 and 1996, respectively. From 1997 to 2002, he held several teaching positions at Kao Yuan Institute of Technology, Kaohsiung, Taiwan; Dayeh University, Changhua, Taiwan; and National Kaohsiung First University of Science and Technology, Kaohsiung, Taiwan. Since 2002, he has been with the Department of Electrical Engineering, National Cheng Kung University, Tainan, Taiwan, where he is currently a Professor. His research interests include motion control, motor drives, visual servoing, and robot control.

Chun-Hsien Wu was born in Taiwan, in 1985. He received a B.S. degree in Electrical Engineering from the National Cheng-Kung University, Taiwan, in 2008. He received an M.S. degree in Electrical Engineering from the National Cheng-Kung University, Taiwan, in 2009. He is currently a civil servant of the National Communication Committee, Taiwan. His research interests include motion control and nonlinear control theories.

A Wheeled Robot Indoor Positioning System Based on Particle Filter

Yuan-Pao Hsu and Chih-Hao Yang

Abstract—**This paper combines the sensory data of odometers and a Laser Range Finder (LRF) through the Particle Filter (PF) algorithm to realize an indoor positioning system on a wheeled robot. In the system a particle set and the odometer are first used to predict the posture of the robot, and then the data points measured by the LRF are clustered by an Adaptive Breakpoint Detector (ABD) algorithm. An Iterative End-Point Fit (IEPF) algorithm is then adopted to perform line segment fitting on the clustered laser points to generate a local map. Each particle will be assigned a weight according to the comparison results of this local map and a built-in environment map. Finally, a resampling procedure is performed in accordance with each particle's weight to generate a new particle set to correct the estimated posture of the robot. This paper uses a Field Programmable Gate Array (FPGA) based platform as the hardware control platform, which is responsible for data acquisition of motor encoders and motors control. A remote computation platform is used for receiving motor encoder data from the hardware control platform and measurement data of the LRF. After a series of computations, the remote computation platform transmits the final control command back to the hardware control platform to drive the motors. Simulation and experimental results show that the resultant system can accurately correct posture errors of the robot within ranges, where the position error range is ± 0.1m and the orientation error range is ± 5 degrees.**

Index Terms: **Field programmable gate array, indoor positioning, Laser range finder, particle filter, odometer.**

I. INTRODUCTION

1.1 Background

MANY countries have developed national projects to stimulate economic growth in response to labor shortages and boost productivity, and an important solution to the labor shortage in these projects is the use of robots to replace manpower. In addition to the need of industrial robots for intelligent production in factories, the need of a storage system for storage and management of products for factories is another challenge. Actually, not only factories need storage systems, recent popular e-commerce companies also need these related systems and technologies. Consequently, mobile robots, the key role in storage systems, would be more demanded in the near future.

If a robot wants to move smoothly in the environment, the robot has to know related information about the environment, such as aisle, turn corner, wall, etc. Hence, the robot uses sensors to perceive surrounding environments, integrates these sensing data with appropriate algorithms to build the environment map, and even uses the established map to locate itself, which is a processing called SLAM(Simultaneous Localization and Mapping) [1].

1.2 Related Work

Positioning a robot usually encounters a lot of uncertainties, most researchers use the probability algorithms to deal with this issue, such as EKF(Extended Kalman Filter), PF(Particle Filter), EIF(Extended Information Filter),and etc. Teslic *et al.* [2] used a LRF and odometer sensors and combined with the EKF algorithm and map matching to implement a robot positioning system. Chen *et al.* also used a LRF and odometers, extracted the environmental features from a number of corner points, and combined with the EKF algorithm for indoor robot positioning [3].

There are some scholars used camera and other image capture sensors to locate robots. Hashemi *et al.* used landmarks, line segments and feature points and applied with the PF algorithm to achieve a biped robot indoor positioning system [4]. In [5], Baklouti *et al.* adopted 3D image sensor information and the PF algorithm for positioning a mobile wheelchair, and introduced a three-dimensional obstacle detection controller, which is responsible for processing a variety of different shapes of three-dimensional obstacles.

In addition to general mobile robot localization research field, there are also many scholars focused on localization other issues. Kim *et al.* used some known information, fixed landmarks, distance, and azimuth messages to compare the performance between EKF and PF algorithms, and derived that PF is less affected by non-Gaussian noise than EKF [6]. Scholars, Li *et al.*, probed into the resampling steps of PF, proposed the classification of various resampling methods and provided a reference standard for the selection of resampling methods [7].

According to above discussion, the PF algorithm has shown effective on robot positioning. This motivates this paper to integrate LRF, odometer and PF algorithm into a system to control motion of a wheeled robot, in order to carry out the task of localization in indoor environments.

The rest of the paper is organized as follows. Section II describes the robot motion control process. The localization algorithm based on the PF is proposed in Section III. System integration is presented in Section IV. Simulation and experimental results are presented in Section V. Finally, some concluding remarks and perspectives are given in Section VI.

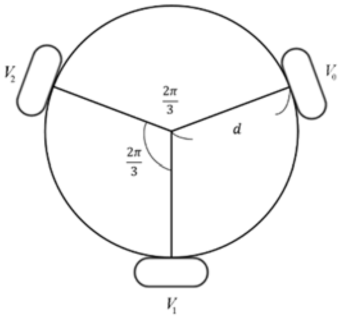

Fig. 1. Wheeled robot configuration diagram.

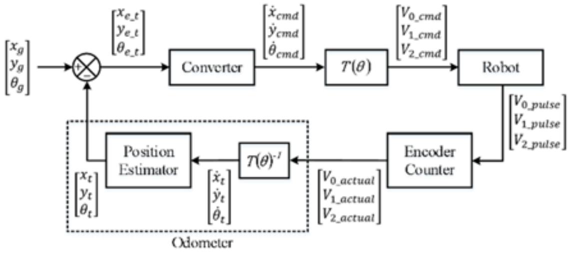

Fig. 2. Platform control diagram.

II. ROBOT MOTION CONTROL

This section will introduce the used omni-direction mobile platform due to its high maneuverability. The platform can perform motion such as in situ rotation, cure movement, etc. Being a three-DOF mobile platform that the robot can be localized in position (x, y) and angle (θ) at the same time. Fig. 1 shows the configuration diagram of a tri-omni wheeled robot.

Fig. 2 shows the platform control diagram. Assuming that the target posture which we want the robot to be is $[x_g \quad y_g \quad \theta_g]^T$ and the current robot posture is $[x_t \quad y_t \quad \theta_t]^T$, we subtract the current posture from the target posture to produce posture error $[x_{e\_t} \quad y_{e\_t} \quad \theta_{e\_t}]^T$. Then the posture error is converted to the speed control command $[\dot{x}_{cmd} \quad \dot{y}_{cmd} \quad \dot{\theta}_{cmd}]^T$ and further generating the three wheels speed command $[v_{0\_cmd} \quad v_{1\_cmd} \quad v_{2\_cmd}]^T$ to output to control the robot. The motor encoders will return the pulses number of each motor $[V_{0\_pulse} \quad V_{1\_pulse} \quad V_{2\_pulse}]^T$, and then the three wheels speeds are calculated through (1).

$$V_{i\_actual} = (V_{i_{pulse}} * 2\pi r)/(\Delta T n ι) \qquad (1)$$

where r is the wheel radius, n is the number of pulses for the wheel to rotate one revolution and ι is the gear ratio. After the speed of each wheel is obtained, then the speed is multiplied by ΔT(control cycle time) , and adding the robot posture at time step $t-1$ $[x_{t-1} \quad y_{t-1} \quad \theta_{t-1}]^T$, the robot posture at time step t $[x_t \quad y_t \quad \theta_t]^T$ is then obtained. Please refer to [8] for the detail.

III. LOCALIZATION ALGORITHM BASED ON PARTICLE FILTER

In the Section, the PF algorithm will be employed to estimate the state of a system in three stages: prediction, weight assignment and resampling.

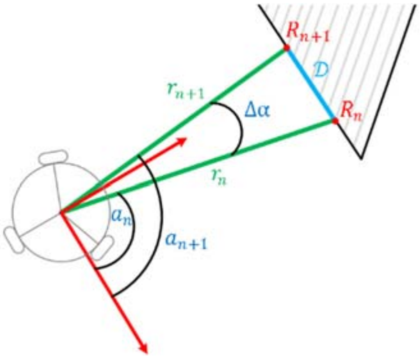

Fig. 3. ABD algorithm.

Fig. 4. Data points set.

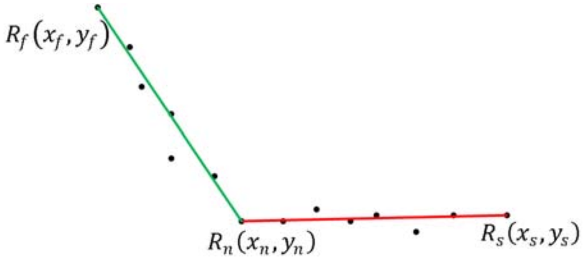

Fig. 5. Results of IEPF algorithm.

3.1 Prediction

From the posteriori probability P_{t-1} of time step $t-1$ and the control command u_t of time step t, the system state is predicted. At the current time step t, the system state is represented by a probability $\overline{P_t}$ called priori probability.

$$\bar{p_t}^{(m)} \sim p(s_t | u_t, p_{t-1}^m), \qquad m = 1 \sim M \qquad (2)$$

where s_t is the system state at time t and *M* is the number of particles.

3.2 Weight Assignment

The weight assignment is carried out through the measured information of the LRF and the built-in map of the robot. The ABD algorithm, shown in Fig. 3, is used to cluster the laser data points. When $D(R_n, R_{n+1}) < D_{thd}$, laser points R_n and R_{n+1} are clustered to the same group. If $D(R_n, R_{n+1}) \geq D_{thd}$, laser point R_{n+1} is clustered to a group which is different from the group which R_n belongs to. $D(R_n, R_{n+1})$ and D_{thd} are calculated as in (3) and (4).

$$D(R_n, R_{n+1}) = \sqrt{r_n^2 + r_{n+1}^2 - 2 r_n r_{n+1} \cos \Delta\alpha} \qquad (3)$$

$$D_{thd} = r_n \frac{\sin \Delta\alpha}{\sin(\lambda - \Delta\alpha)} + 3\delta_r \tag{4}$$

where the distance information of a laser data point is presented by r_n, $\Delta\alpha$ is the angle between laser beams, δ_r is the data noise of the LRF, and λ is the threshold of cluster.

After grouping, each data points group needs to be extracted line segment features for the subsequent operation. In this section, the IEPF algorithm is used for the line segment feature extraction. Fig. 4 depicts the schematics of a data point group, and Fig. 5 shows the processing result of the IEPF algorithm for the group.

Once each line segment feature has been extracted, the least square regression(LSM) is used to calculate line parameters, which is represented by polar coordinates, the distance ρ_R^k and the angle α_R^k, where k is the number of line sets, and can be calculated by (5) and (6), respectively.

$$\alpha_R^k = \frac{1}{2} atan\left(\frac{-2 \cdot \sum_{i=1}^{i}\left[\left(y_m^k - y_i^k\right)\left(x_m^k - x_i^k\right)\right]}{\sum_{i=1}^{i}\left[\left(y_m^k - y_i^k\right)^2 - \left(x_m^k - x_i^k\right)^2\right]} \right) \tag{5}$$

$$\rho_R^k = x_m^k \cos(\alpha_R^k) + y_m^k \sin(\alpha_R^k) \tag{6}$$

where x_m^k and y_m^k are calculated by (7) and (8), N is the number of laser points on the line：

$$x_m^k = \frac{1}{N}\sum_{i=1}^{i} x_i^k\,, i = 1 \sim N \tag{7}$$

$$y_m^k = \frac{1}{N}\sum_{i=1}^{i} y_i^k\,, i = 1 \sim N \tag{8}$$

A particle, which is closer to the actual system state, should have its higher assigned weight. In the section, the Gaussian kernel function is used to assign the weight of each particle, as shown in (9), where R is the measurement noise. Therefore, each particle's weight will be normalized to complete the particle weight calculation.

$$\omega(m) = \frac{1}{\sqrt{R}\sqrt{2\pi}} * exp\left(-\frac{\left|\rho_R^k - \rho_p^m\right|^2}{2R}\right) \tag{9}$$

3.3 Resampling

The resampling is according to the weight of each particle in the particle set. In doing so, we use multinomial, stratified, systematic, residual and RSR five resampling algorithms to carry out simulation and experiments to compare their performances; for details, please refer to [7]. The resampling result of the new particle set is finally applied to estimate the system state and complete a control cycle.

Fig. 6. System architecture diagram.

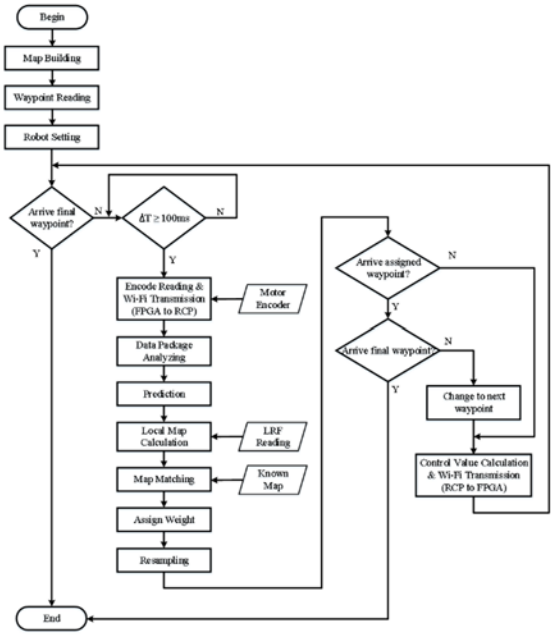

Fig. 7. Localization system flowchart.

IV. SYSTEM INTEGRATION

4.1 System Architecture

Fig. 6 shows the system architecture diagram. The system uses a FPGA development board to catch motor encoder data, and sends the data to RCP(Remote Computation Platform) through a Wi-Fi module. RCP combines the received data and the measurement information of the LRF to compute the robot posture and robot control commands.

4.2 Localization System Flowchart

Fig. 7 depicts the software flowchart of the localization system. After initialization, the system reads encoder data from hardware platform, and transmits the data to RCP through Wi-Fi module. The RCP combines this data with the PF algorithm to predict the robot posture. Then the system uses ABD and IEPF algorithms to extract environment features from LRF data to match with built-in map, and assigns each particle's weight according to matching results. The PF can produce a new particle set by resampling this weight in the assigned particle set according to the weight of each particle. Finally, the new particle set is then used to update the robot prediction posture. Based on this updated posture, the system will calculate new control command and transmit this control command back to the hardware platform, in order to drive the robot.

V. SIMULATION AND EXPERIMENTS

In this section, indoor positioning simulation for the robot is performed to first confirm the feasibility of the PF method and the robot system architecture described in the previous sections. Afterward, the whole system is realized on a tri-omni wheeled robot to carry out experiments.

5.1 Simulation

In this subsection, a particle filter localization simulation is performed to control the robot travelling to all the planned waypoints in a known indoor environment. Fig. 8 show the simulation results that the estimated robot's trajectories via the PF estimation are quite close to those of real trajectories. The results reveal that the five resampling algorithms can run smoothly in this application.

5.2 Experiments

Fig. 9 shows posture variations of the robot during localization experiments. Since the experimental results of the five resampling methods are almost identical, only the results of the RSR method are shown in the figure, where Fig. 9(a) shows the position variations in the x direction, Fig. 9 (b) displays the position variations in the y direction, and Fig. 9(c) depicts the orientation variations. Motion trajectories of the localization experiments are respectively shown in Fig.10 (a) - (e) by respectively using the multinomial, stratified, systematic, residual, and RSR algorithms.

The errors in positioning experiments are shown in Table 1, which are the errors between the initial postures and return postures. The position errors of experimental lie within 0.1 meters and the orientation error is within 5 degrees. The result indicates that this system can accurately accomplish the task of indoor positioning. Additionally, the result also verifies that the five resampling algorithms can be applied to this kind of task. Worthy of mention is that the robot travelled for about 80 meters and the motion trajectory was in accordance with the setting trajectory.

Furthermore, Table 2 lists the FPGA total resource usage, where the FPGA chip is Altera Cyclone III EP3C16F484, containing 15,408 LEs(Logic Elements). The system uses 51.5% of the FPGA LEs, among which software is 39.4% and hardware is 12.1%. The result shows that the FPGA realization succeeded.

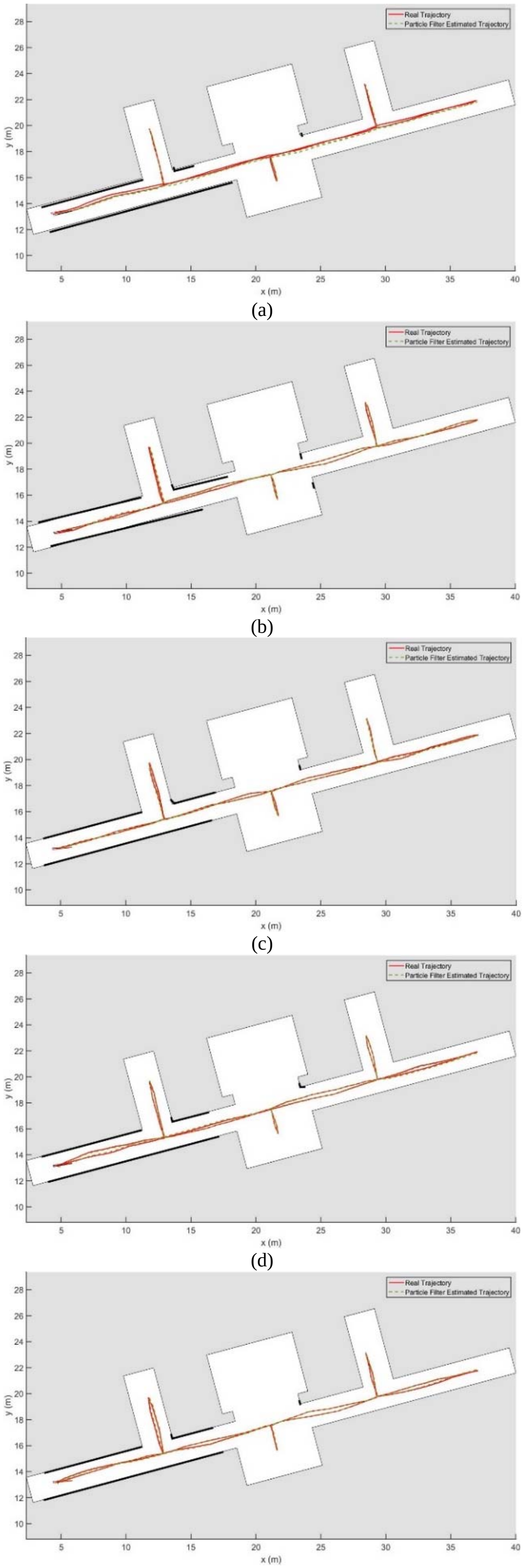

(a)

(b)

(c)

(d)

(e)

Fig. 8. Simulated trajectories of five resampling methods:(a) multinomial ; (b)stratified ; (c)systematic ; (d)residual ; (e)RSR.

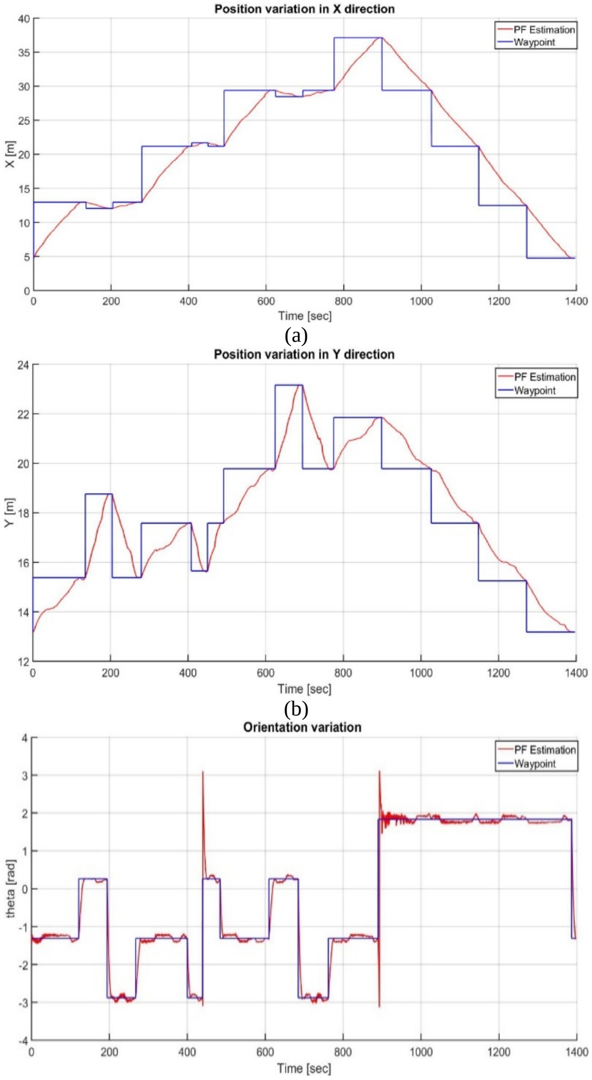

Fig. 9. Position variations of final experiments: (a)X direction; (b)Y direction; (c)Orientation.

VI. CONCLUSIONS

6.1 Conclusions

This paper has realized an indoor positioning wheeled robot with a FPGA cored platform as the control board. The positioning algorithm is based on the known Particle Filter algorithm. Combining with the odometry information and LRF readings as the sources of the robot's environmental perception, the robot can perform localization task in a known indoor environment [9]. The simulation and experimental results show that the system can accurately accomplish the indoor positioning task, where the position error is within 0.1 meters and the orientation error is within 5 degrees.

Moreover, this paper has also used five different resampling algorithms in simulation and experiments. The results show that these five methods can be applied to indoor positioning, even after long voyage and steering.

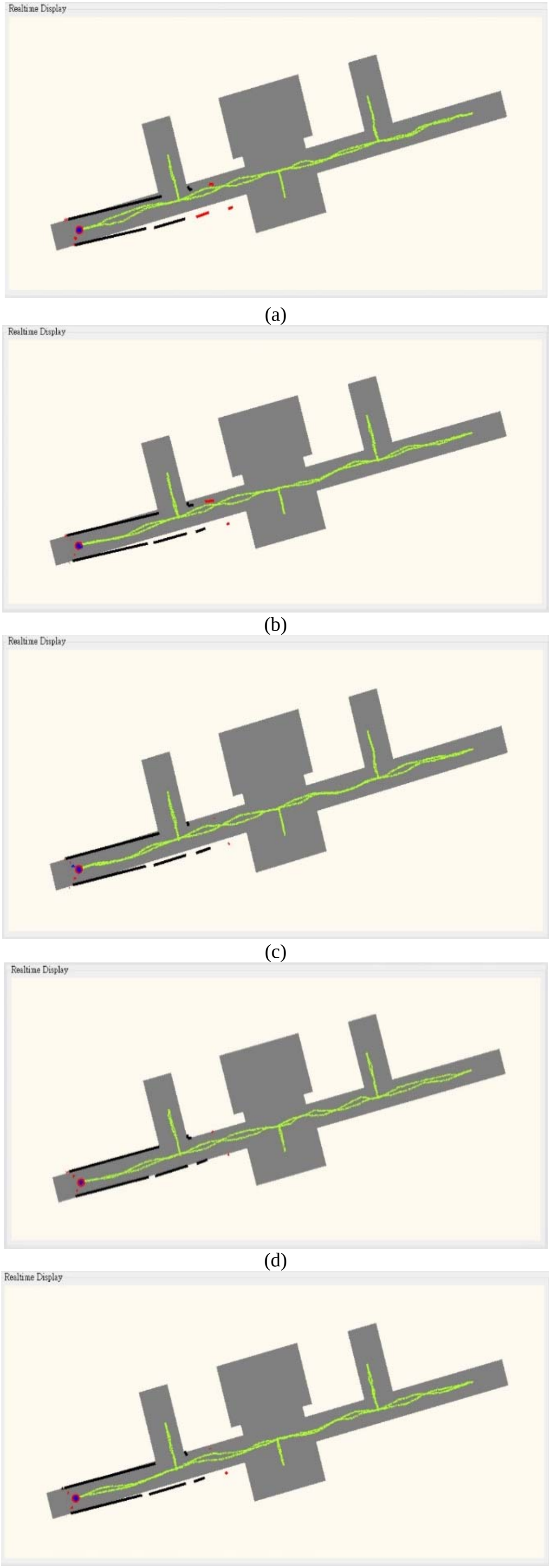

(e)

Fig. 10. Experimental trajectories of various resampling methods: (a)Multinomial; (b)Stratified; (c)Systematic; (d)Residual; (e)RSR.

TABLE I. ERRORS OF LOCALIZATION EXPERIMENTS.

Resampling Method	x_{error}(m)	y_{error}(m)	θ_{error}(deg)
Multinomial	0.09	0.03	4.1
Stratified	0.11	0.01	4.6
Systematic	0.08	0.05	2.9
Residual	0.08	0.05	2
RSR	0.06	0.05	1.9

TABLE II. FPGA RESOURCE USAGE.

FPGA(7938LEs)					
System			LEs	Total LEs	Les usage
Hardware	Control Interface	Motor Motion Control	191	1865	12.1%
		Motor Encoder Capture	218		
	Other		1456		
Software			6073	6073	39.4%
Total Resources Usage			15408	7938	51.5%

6.2 Future Work

The positioning system implemented in this research can be improved toward the following aspects.

(1) The system should be able to use another kind of features, such as corners, landmarks and etc. to improve the accuracy of positioning.

(2) The robot's chasis is made of aluminum, although it is very strong, but its weight is relatively heavy. In the future, it is suggested to use carbon fiber or other lightweight and high strength material for the robot.

(3) In the future, by integrating with other kinds of sensors, such as Radio Frequency Identification(RFID), image processing, etc., the system can do more complex tasks like SLAM(Simultaneous Localization and Mapping).

REFERENCES

[1] D.-W. Hugh and T. Bailey, "Simultaneous Localization and Mapping (SLAM) : Part I The Essential Algorithms," *IEEE Robotics & Automation Magazine*, Vol.13, No.2, pp.99-110,September 2006.

[2] L. Tesli´c, I. Škrjan,c and G. Klanˇcar, "EKF-Based Localization of a Wheeled Mobile Robot in Structured Environments," *Journal of Intelligent & Robotic Systems*, Vol. 62, No. 2, pp. 187-203, May 2011.

[3] L. Chen, H. Hu, and K. McDonald-Maier, "EKF Based Mobile Robot Localization," in *Proceedings of the 2012 Third International Conference on Emerging Security Technologies*, pp. 149-154, October 2012

[4] E.Hashemi, M. G. Jadid, M. Lashgarian, M. Yaghobi, and M. Shafiei, "Particle Filter Based Localization of the Nao Biped Robots," *in Proceeding of 2012 44th Southeastern Symposium on System Theory(SSST)*,pp. 168-173, March 2012

[5] E.Baklouti, N. B.Amor, and M.Jallouli, "Particle Filter Localization and Real Time Obstacle Avoidance Control Based on 3D Perception for Wheelchair Mobile Robot," in *Proceeding of 2016 IEEE 8th International Conference on Intelligent Systems(IS)*,pp. 735-740, November 2016.

[6] Tae Gyun Kim, Hyun-Taek Choi and Nak Yong Ko, "Localization of a Robot Using Particle Filter With Range and Bearing Information," in *Proceeding of 10th International Conference on Ubiquitous Robots and Ambient Intelligence (URAI), 2013*, pp. 368–370, October 2013.

[7] T. Li, M. Bolic´, and Petar M. Djuric, "Resampling Methods for Particle Filtering: Classification, Implementation, and Strategies," *IEEE Signal Processing Magazine*, Vol.32, No.3, pp.70-86, May 2015.

[8] C. -H. Yang, *A Wheeled Robot Indoor Positioning System Based on Particle Filter*, Master Thesis, Department of Computer Science and Information Engineering National Formosa University, 2018

Yuan-Pao Hsu received the B.S. and M.S. degrees in the Department of Electronic Engineering from National Taiwan University of Science and Technology, Taipei, Taiwan, R.O.C., in 1987 and 1989. He received the Ph.D. degree in Electrical Engineering department of National Chung Cheng University, Chiayi, Taiwan, R.O.C., in 2004. His research areas are mobile robot applications, applications of SW/HW co-design, machine learning, image processing, and embedded systems.

Chih-Hao Yang received the B.S. degree in the Department of Electrical Engineering from Far East University, Tainan, Taiwan, R.O.C., in 2016. He received the M.S. degree in the Department of Computer Science and Information Engineering from National Formosa University, Yunlin, Taiwan, R.O.C., in 2018. His major research interests include mobile robot applications and applications of SW/HW co-design.

Intelligent Control of a Wheeled Mobile Robot for Path Tracking and Anti-Collision System

Gwo-Ruey Yu, *Member, IEEE* and Yu-Shan Chiu

Abstract—**This paper proposes a design of intelligent controllers for the path tracking and anti-collision system of a wheeled mobile robot (WMR). We design the intelligent controllers by using fuzzy logic systems that incorporate expert knowledge in terms of 25 linguistic rules to drive the WMR to track a straight line and a target position. The program codes of intelligent controllers are implemented on a PC which could send all the motion commands to the WMR by wireless communication. Experiment results demonstrate that the performance of the intelligent controllers is superior to that of fine-tuned PID controllers. Based on the intelligent controller of the anti-collision system, the WMR can shun the barrier.**

Index Terms—Wheeled Mobile Robot, Intelligent Control, Path Tracking.

I. INTRODUCTION

ROBOTS could assist humans in performing some activities that are considered laborious, boring, and at risky situation. Robots are also achieving operations more efficiently than the humans and they lead to the increase of the productivity, of the precision, and of the reliability [1]. There are many advantages to incorporate robots in automatic control systems. Thus, wheeled mobile robots (WMR) have been widely investigated and applied in recent years [2]-[5].

The WMR is a nonholonomic dynamic system for which linear control theory cannot be implemented directly [6]. It is a challenge task to control the motion of WMRs. There have been some methodologies in studying the motion control of WMRs, such as sliding mode control [7], predictive control [8], discontinuous feedback [9], switching control [10], time-varying continuous feedback [11], dynamic feedback linearization [12], neural networks-based control [13], and hybrid control strategy [14]. However, it is not easy to realize these methods on WMRs since the complexity of these controllers result in high computational power. On the other hand, intelligent controllers designed by fuzzy logics are capable of tackling nonlinear control systems, making inferences under uncertainty, and easily carrying out hardware realization. Therefore, fuzzy logic controllers are adopted to do the path tracking of a WMR in this paper.

The fuzzy logic control has emerged as one of the most active and useful research areas since Prof. Zadeh established the fuzzy set theory. In recent years, there have been some robot applications using fuzzy logic control [15]-[17]. The use of fuzzy control owns the following two advantages: (i) there is no precise mathematical model needed to design the control system; (ii) expert knowledge can provide linguistic fuzzy control rules or linguistic fuzzy description of the system. The linguistic fuzzy if - then rules will take the fuzzy control of actions. The fuzzy membership functions will characterize the degree of linguistic rules. There are many kinds of fuzzy inference systems in the applications of fuzzy logic control. The Takagi-Sugeno fuzzy model is an efficient technique to describe the behavior of a dynamic plant. In this paper, the authors will apply the Sugeno-type inference system to design the fuzzy logic controllers.

The main contributions of this paper are twofold. First, the intelligent controllers are designed to drive the WMR to trace a straight line and a target position. Second, the anti-collision system is designed by using the intelligent controllers. The rest of this paper is organized as follows. Section 2 describes the wheeled components and architectures of the wheeled mobile robot. Section 3 proposes the design of PID controllers and fuzzy controllers. Section 4 shows experimental results with the presented scheme. Section 5 draws the conclusion.

II. The Wheeled Mobile Robot I90

We used the wheeled mobile robot I90 which is made in Dr. Robot Company [18] for the experimental platform. The robot I90 is a three-wheeled mobile robot with wireless (WiFi 802.11g) and high resolution pan-tilt-zoom CCD camera. The specifications of the robot I90 are described as follows:

A. Mechanics

The weight of the wheeled mobile robot I90 is 5 kg, which can carry an additional payload of 15 kg. The dimensions of the robot I90 are 43 cm width, 38 cm length, and 30 cm height. There are two 12V DC motors with integrated 800 counts per cycle optical encoder in the robot I90. Each motor can supply 40kg.cm of torque. The diameter of two driving wheels is 18 cm. The top speed of the wheels is 0.75 m/s. Fig. 1 shows the diagrammatic sketch of the two-wheeled robot.

B. Architecture

The high-level control of the wheeled mobile robot I90 is sustained by a remote PC communicating with a wireless link. Low-level functionality is operated by an onboard digital signal processor (DSP) while computationally intensive

---

Gwo-Ruey Yu is with Department of Electrical Engineering and Advanced Institute of Manufacturing with High-tech Innovations, National Chung Cheng University, Chia-Yi, Taiwan (e-mail: ieewoyu@ccu.edu.tw).

Yu-Shan Chiu is with Graduate Institute of Opto-Mechatronics, National Chung Cheng University, Chia-Yi, Taiwan.

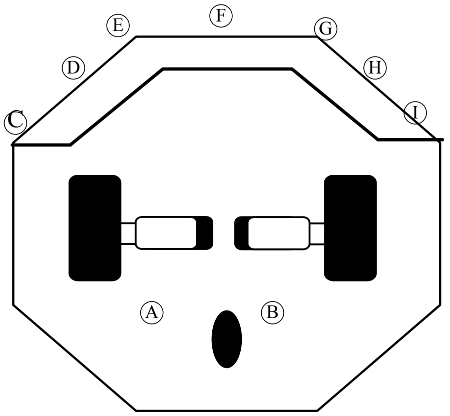

Fig. 1. Two-wheeled mobile robot.

Table 1. The number of modules and servos.

Infrared Range Sensor #1	C - Left front
Infrared Range Sensor #2	D - Left front
Infrared Range Sensor #3	E - Middle front
Infrared Range Sensor #4	F - Middle front
Infrared Range Sensor #5	G - Middle front
Infrared Range Sensor #6	H - Right front
Infrared Range Sensor #7	I - Right front
DC Motor #1 with quadrature encoder	A - Left, use channel 1
DC Motor #2 with quadrature encoder	B - Right, use channel 2

actions are performed off board. The robot I90 can up-load all sensor data to a PC at a rate in excess of 10Hz by an integrated high bandwidth (54Mbps) wireless module. The robot I90 includes development software components such that users can put the coding program into design the controller.

C. Sensor Modules

There are three ultrasonic range sensor modules and seven infrared range sensor modules in the wheeled mobile robot I90. These sensor modules can be utilized to detect obstacles, avoid collisions, find robot range, build a robot environment map. The ultrasonic range sensor module can detect the range information from 4 cm to 340 cm. The working frequency of the ultrasonic range sensor modules is 40 KHz. The ultrasonic range sensor module is plugged inside the wheeled mobile robot I90. The infrared range sensor module can detect the range information from 10 cm to 80 cm. The output information of the infrared range sensor modules is from 0 to 3 VDC. The infrared range sensor module is plugged in the motion control board of the robot I90. Table 1 lists the number of modules and servos.

D. Kinematics Equations of the WMR

The kinematics equations of the considered wheeled mobile robot I90 are given by [19]:

$$\boldsymbol{x}(\boldsymbol{k}+1)=\boldsymbol{x}(\boldsymbol{k})+\frac{\cos(\theta(\boldsymbol{k}))\cdot\Delta \boldsymbol{t}}{2}\boldsymbol{f}_1(\boldsymbol{k}) \tag{1}$$

$$\boldsymbol{y}(\boldsymbol{k}+1)=\boldsymbol{y}(\boldsymbol{k})+\frac{\sin(\theta(\boldsymbol{k}))\cdot\Delta \boldsymbol{t}}{2}\boldsymbol{f}_1(\boldsymbol{k}) \tag{2}$$

$$\theta(\boldsymbol{k}+1)=\theta(\boldsymbol{k})+\frac{\Delta \boldsymbol{t}}{\boldsymbol{b}}\boldsymbol{f}_2(\boldsymbol{k}) \tag{3}$$

$$\boldsymbol{f}_1(\boldsymbol{k})=\boldsymbol{V_R}(\boldsymbol{k})+\boldsymbol{V_L}(\boldsymbol{k}) \tag{4}$$

$$\boldsymbol{f}_2(\boldsymbol{k})=\boldsymbol{V_R}(\boldsymbol{k})-\boldsymbol{V_L}(\boldsymbol{k}) \tag{5}$$

where (x, y) are the coordinates of the WMR position, θ is the angle between the heading direction and the x-axis, b is the length between the left wheel and the right wheel, Δt is the sampling time interval; V_R is the velocity of right wheel, V_L is the velocity of left wheel. Fig. 2 shows the schematic kinematics model of the WMR.

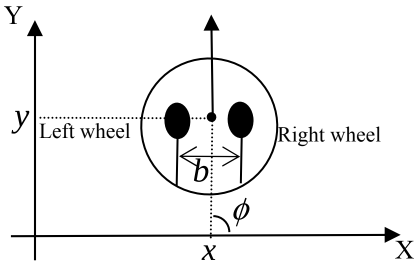

Fig. 2. Schematic kinematics model of the WMR.

III. Control Strategy

A. Intelligent Controller

The Sugeno-type inference system is applied to design the intelligent controllers. The fuzzification procedure maps the crisp input values to the linguistic fuzzy terms using the degree of membership values between 0 and 1. We use five membership functions for both displacement and velocity errors. Figs. 3-4 show the input membership functions, respectively. Fig. 5 shows the output membership functions defined to be fuzzy singleton functions.

The fuzzy sets are defined as follows: NB ≡ Negative Big, NS ≡ Negative Small, ZE ≡ Zero, PS ≡ Positive Small, and PB ≡ Positive Big. Fig. 6 shows the block diagram of the intelligent control system for the WMR path tracking. The output of the fuzzy logic controller is the motor voltage which will govern the velocity of the WMR. The ultrasonic sensor module will detect the displacement of the WMR.

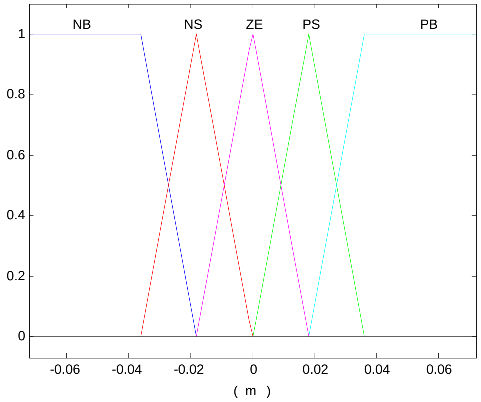

Fig. 3. Membership functions of the displacement error.

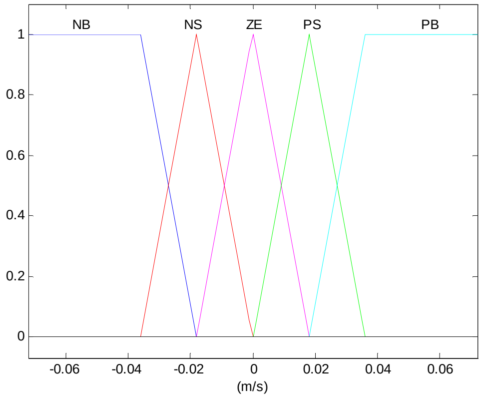

Fig. 4. Membership functions of velocity error.

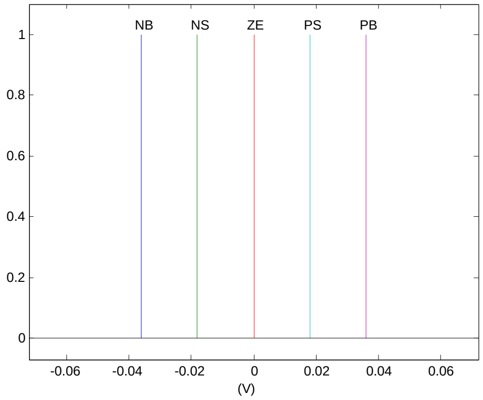

Fig. 5. Output membership functions.

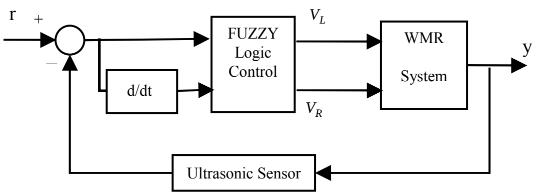

Fig. 6 The block diagram of intelligent control system

Table II. Fuzzy rules of the wheeled mobile robot.

V		*e*				
		NB	NS	ZE	PS	PB
de	NB	PB	PB	PB	PS	ZE
	NS	PB	PS	PS	ZE	NS
	ZE	PS	PS	ZE	NS	NS
	PS	PS	ZE	NS	NS	NB
	PB	ZE	NS	NB	NB	NB

Based on the expert knowledge and testing, the control rules are designed as follows. For example, if the e is Negative Big (NB) and *de* is Negative Big, then the robot velocity should be Positive Big (PB). We acquire 25 fuzzy rules after incorporating this expert knowledge. These rules are designed as follows:

Rule 1: if e = NB and de = NB then V = PB

Rule 2: if e = NS and de = NB then V = PB

⋮

Rule 25: if e = PB and de = PB then V = NB

Table 2 lists the 25 fuzzy rules associated with linguistic variables.

B. PID Controller

Proportional-Integral-Derivative (PID) controllers are implemented in industry enormously. To demonstrate the advantages of the intelligent controllers, the fine-tuned PID controllers are designed for comparison. A PID controller could be considered as an extreme form of a phase lead-lag compensator with one pole at the origin and the others at infinity. In the case of PID control, the transfer function of the PID controller is designed as follows:

$$G_c(s) = K_P + K_D s + \frac{K_I}{s} \tag{6}$$

where K_P is the proportional gain, K_I is the integral gain, and K_D is the derivative gain. The functions of the PID controller are described as follows. The proportional term could provide an overall control action. The integral term could reduce steady-state errors through low-frequency compensation by an integrator. The derivative term could improve transient response which is proportional to the error signal through the all-pass gain factor [20]. In this paper, two PID controllers are fine-tuned by a try-and-error method to control the velocity of the WMR.

C. Anti-Collision System

Seven infrared range sensor modules are used to design the anti-collision system for the WMR. The voltage signal is transmitted by the infrared range sensor. To transform the voltage signal into the distance information is important. Fig. 7 shows the transformation flow chart.

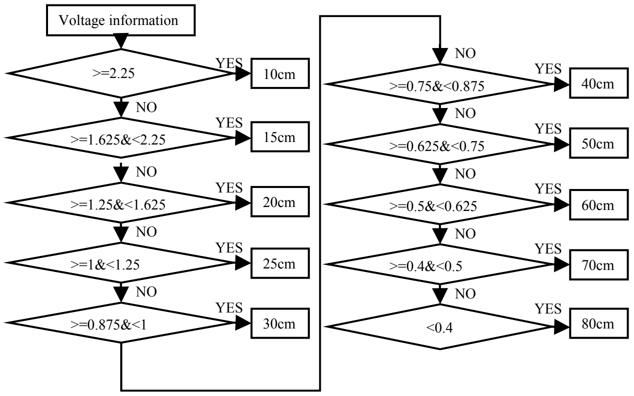

Fig. 7. IR sensor information transformation.

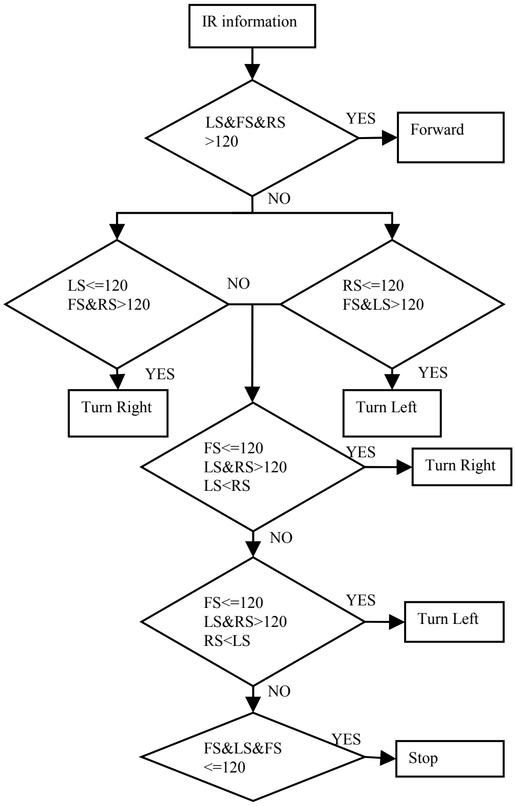

Fig. 8. Flow chart of anti-collision system.

As soon as the distance information is obtained by transferring the information of infrared range sensor, the equalities are designed as follows;

$$\text{Left Side (LS)} \equiv C+D+E \tag{7}$$

$$\text{Front Side (FS)} \equiv E+F+G \tag{8}$$

Fig. 9. Photo of the wheeled mobile robot I90.

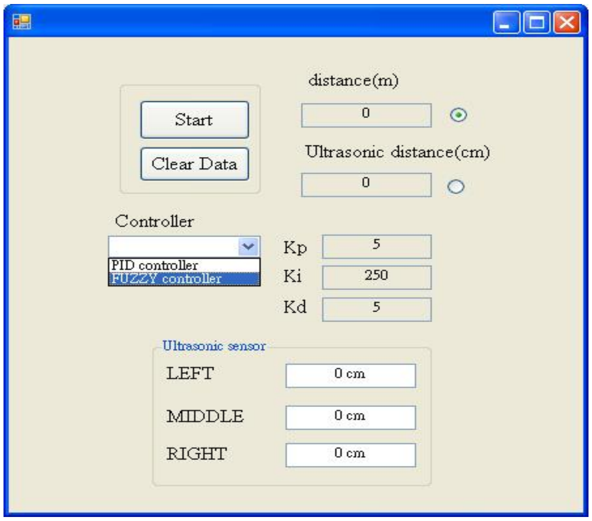

distance(m) 0 ⊙
Ultrasonic distance(cm) 0 ○
Controller
PID controller
FUZZY controller
Kp 5
Ki 250
Kd 5
Ultrasonic sensor
LEFT 0 cm
MIDDLE 0 cm
RIGHT 0 cm

Fig. 10. Front panel of the human-machine interface.

$$\text{Right Side (RS)} \equiv G+H+I \tag{9}$$

Fig. 8 illustrates the flow chart of designing the anti-collision system.

IV. EXPERIMENTAL RESULTS AND DISCUSSION

The control algorithms are coded as the Visual C + + program to perform experiments. Fig. 9 shows the photo of the robot I90. Fig. 10 shows the front panel of human-machine interface.

After several experiments, the parameter values of fine-tuned PID controllers are sought out as follows: $K_P = 5$, $K_I = 250$, and $K_D = 5$. In the channel of fuzzy controller, we used 25 fuzzy rules to control the two-wheel motor velocity such that the WMR could track a straight line and a target position.

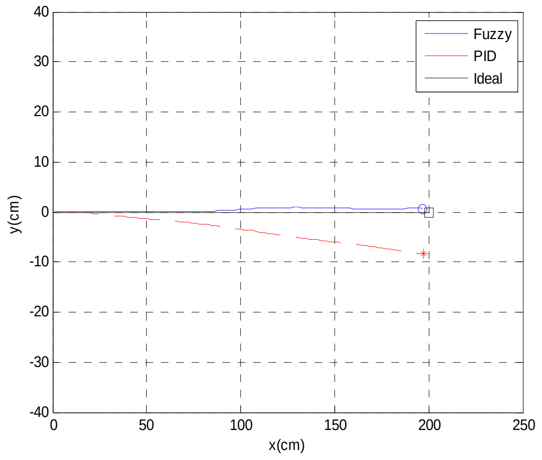

Fig. 11. Trajectory of the WMR.

Table III. Comparative errors of tracking a reference path.

	Tracking Error (cm)
Fuzzy controller	**1.2715**
PID controller	**8.8298**

A. Tracking a Straight Line

In the experiment, we assume that the desired trajectory is a straight line. The total length of the straight line is 200cm. Fig. 11 shows the trajectory of the WMR using the fuzzy logic controllers. The fine-tuned PID controllers do the same experiment for comparison.

In Fig. 11, the symbol ('□') means the desired trajectory, the symbol ('○') represents the trajectory of WMR using fuzzy logic controller, and the symbol ('*') shows the trajectory of WMR using the fine-tuned PID controller. Table 3 lists the tracking errors between the desired trajectory and the trajectory of WMR. Obviously, the fuzzy logic controller obtained better response than the fine-tuned PID controller did. The tacking errors of the fuzzy logic controller are much less than those of the fine-tuned PID controller.

Fig. 12 shows the velocity responses of the left wheel and the right wheel. The fine-tuned PID controllers consume more control energy than the fuzzy logic controllers. However, the tracking error of the fuzzy logic controllers is smaller than the fine-tuned PID controllers. That is, the intelligent controllers are better than the fine-tuned PID controllers in the path tracking of WMR.

B. Tracking a Target Position

Case 1. 20 cm before an object

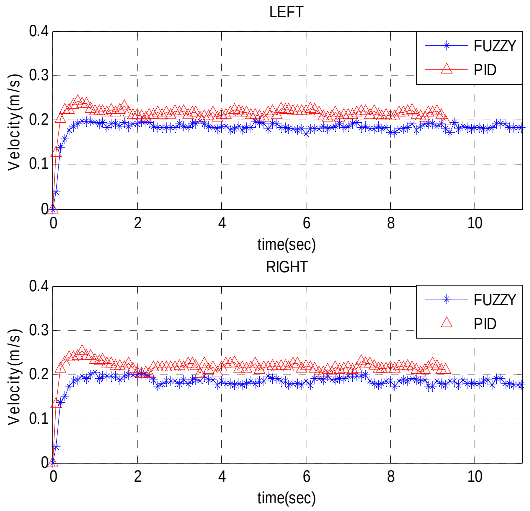

Fig. 12. Velocity responses of the WMR.

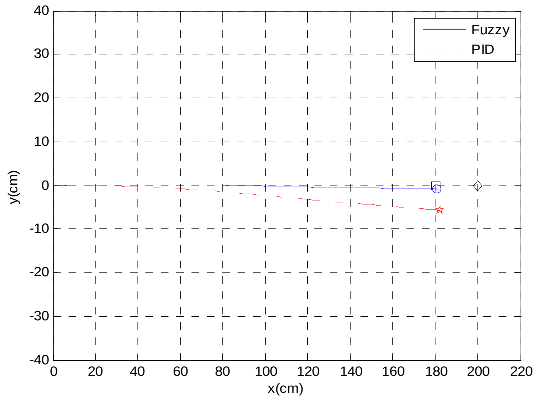

Fig. 13. Trajectory of the WMR (case1).

Table IV. Comparative tracking errors (case1).

	Tracking Error (cm)
Fuzzy controller	**0.6107**
PID controller	**6.1984**

In the experiment, the WMR will track a target whose position is located at the distance 20 cm before an object. Let the coordinates of the object be (200, 0) and the coordinates of the target be (180, 0). When the ultrasonic range sensor modules detect the distance 20 cm, the fuzzy controllers will bring to the destination of the WMR. Fig. 13 shows the trajectories of the WMR using fuzzy logic controllers and fine-tuned PID controllers, respectively.

In Fig. 13, the symbol ('◇') means the object position, the symbol ('□') represents the target position, the symbol ('○') shows the final trajectory of the WMR using the fuzzy logic controller, and the symbol ('☆') shows the final trajectory of the WMR using the fine-tuned PID controller. Table 4 lists the tracking errors of both controllers.

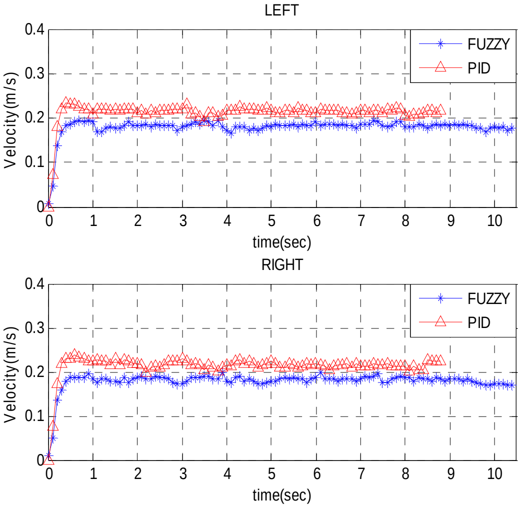

Fig. 14. Velocity responses of the WMR (case1).

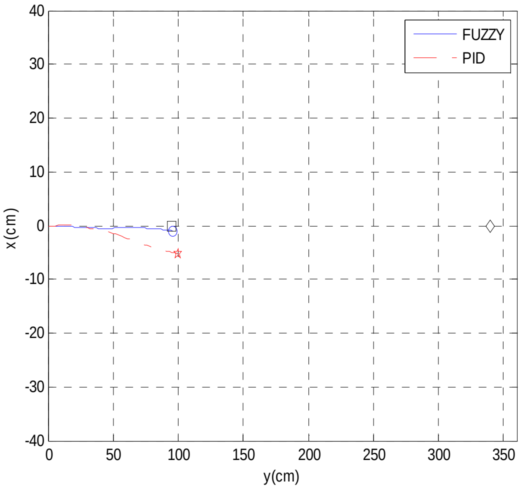

Fig. 15 Trajectories of the WMR (case2)

Fig. 14 respectively shows the velocity responses of the left and right wheels. The fine-tuned PID controller still consume much energy than the fuzzy logic controller does. Apparently, the fuzzy logic controller has smaller tracking errors than the fine-tuned PID controller does. Thus, the intelligent controller is better than the fine-tuned PID controller in terms of target tracking errors.

Case 2. 245 cm before an object

To know the maximum distance of target tracking, the WMR will track a target whose position is located at the distance 245 cm in front of an object. Let the coordinates of the object be (340, 0) and the coordinates of the target be (95, 0). When the ultrasonic range sensor modules reach the distance 245 cm, the fuzzy logic controller will stop the WMR. Fig. 15 depicts he trajectories of the WMR using fuzzy logic controllers and fine-tuned PID controllers, respectively.

Table V. Comparison of the tracking errors (case2).

	Tracking Error (cm)
Fuzzy controller	**0.5704**
PID controller	**6.9999**

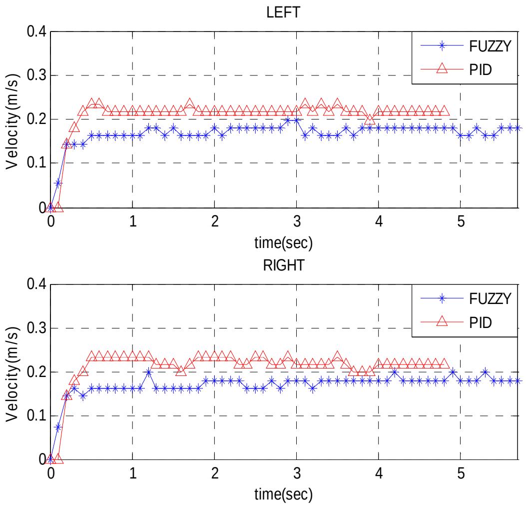

Fig. 16 . Velocity responses of the WMR (case2).

In Fig. 15, the symbol (‘◇’) means the object position, the symbol (‘□’) represents the target position, the symbol (‘○’) shows the final trajectory of the WMR using the fuzzy logic controller, and the symbol (‘☆’) shows the final trajectory of the WMR using the fine-tuned PID controllers. Table 5 compares the tracking error.

Fig. 16 shows the velocity responses of both left and right wheels. Again, the fine-tuned PID controller still consume much energy than the fuzzy logic controller does. On the other hand, the tracking errors of the fuzzy logic controllers are much smaller than those of the fine-tuned PID controller. Thus, the intelligent controller outperforms the fine-tuned PID controller in the maximum distances of target tracking.

Case 3. 12 cm before an object

To know the minimum distance of target tracking, the WMR will track a target whose position is located at distance 12 cm before an object. Let the coordinates of the object be (210, 0) and the coordinates of the target be (198, 0). When the ultrasonic range sensor modules detect the distance 12 cm, the fuzzy logic controller will bring to the target position of the WMR. Fig. 17 shows the trajectories of the WMR using fuzzy logic controller and fine-tuned PID controller, respectively.

In Fig. 17, the symbol (‘◇’) means the object position, the symbol (‘□’) represents the target position, the symbol (‘○’) shows the final trajectory of the WMR using fuzzy logic controllers, and the symbol (‘☆’) shows the final trajectory of the WMR using the fine-tuned PID controllers. Table 6 compares the tracking errors.

Table VI. Comparative tracking errors (case3).

	Tracking Error (cm)

Fuzzy controllers	**1.6954**
PID controllers	**8.6238**

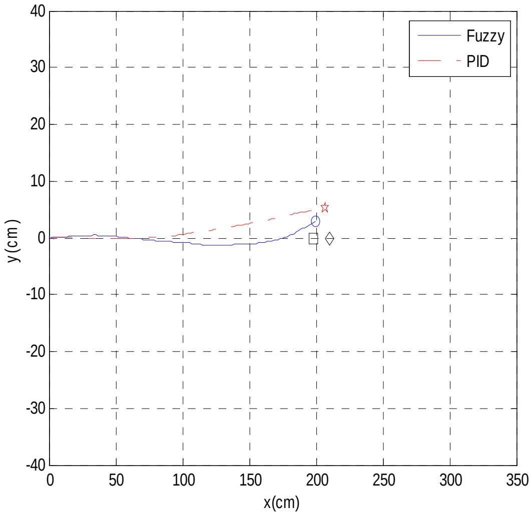

Fig. 17. Trajectories of the WMR (case3).

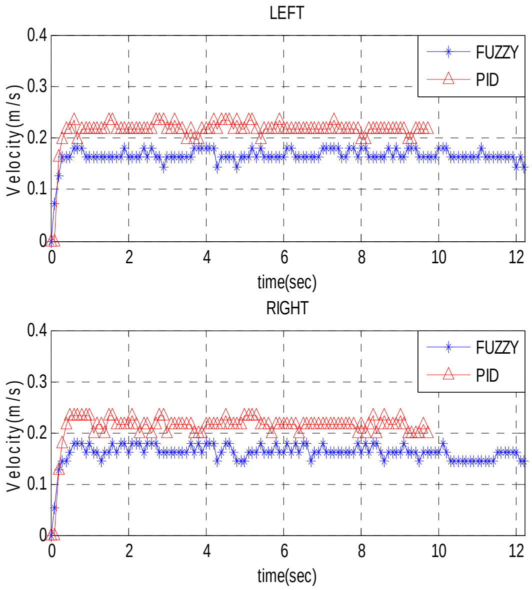

Fig. 18. Velocity responses of the WMR (case3).

Fig. 18 shows the velocity responses of both the two wheels. Similarly, the fine-tuned PID controller still consume much control energy than the fuzzy logic controller does. By the way, the tracking error of the fuzzy logic controller is smaller than that of the fine-tuned PID controller. Therefore, the proposed fuzzy controller is superior to the fine-tuned PID controller in the minimum distances of target tracking.

C. Anti-Collision Experiment

Fig. 19 displays the anti-collision experiment. An L-shaped obstacle is placed to preclude the WMR's moving path. Based on the fuzzy controller, the WMR can shun the barrier and doesn't hit the wall.

Fig. 19. Photos of anti-collision experiment.

V. CONCLUSIONS

In this paper, an intelligent controller has been designed by using fuzzy logic inference system to drive a wheeled mobile robot to achieve path tracking and point stabilization. Three different experiments have been performed to verify the effectiveness of the fuzzy controller design. Experiment results have demonstrated that the performance of the fuzzy controller is superior to that of the fine-tuned PID controller in the case of tracking a straight line and a target stabilization. Both the tracking errors and the control energy of the fuzzy controller are smaller than those of the fine-tuned PID controller. In addition, the anti-collision experiment has also illustrated that the WMR can avoid the barriers by using the fuzzy controller.

REFERENCES

[1] P.A. Lasota, T. Song and J. A. Shah, "A survey of methods for safe human-robot interaction," *Foundations and Trends in Robotics*, vol. 5, no. 4, pp. 261–349, May 2017.

[2] M. A. Kamel, X. Yu, and Y. Zhang, "Fault-tolerant cooperative control design of multiple wheeled mobile robots," *IEEE Transactions on Control Systems Technology*, vol. 26, no. 2, pp. 756–764, March 2018.

[3] J. Liao, Z.Chen, and Bin Yao, "Performance-oriented coordinated adaptive robust control for four-wheel independently driven skid steer mobile robot," *IEEE Access*, vol. 5, pp. 19048-19057, September 2017.

[4] N. Seegmiller and A.Kelly, "High-fidelity yet fast dynamic models of wheeled mobile robots," *IEEE Transactions on Robotics*, vol. 32, no. 3, pp. 614–625, June 2016.

[5] X. Liang, H.Wang, and W. Chen, "Adaptive image-based trajectory tracking control of wheeled mobile robots with an uncalibrated fixed camera, *IEEE Transactions on Control Systems Technology*, vol. 23, no. 6, pp. 2266 - 2282, Nov. 2015.

[6] Z. Li, C. Yang and C.-Y. Su, "Vision-based model predictive control for steering of a nonholonomic mobile robot," *IEEE Transactions on Control Systems Technology*, vol. 24, no. 2, pp. 553–564, March 2016.

[7] J.-X.Xu, Z.-Q. Guo, and T. H. Lee, "Design and implementation of integral sliding-mode control on an underactuated two-wheeled mobile robot," *IEEE Transactions on Industrial Electronics*, vol. 61, no. 7, pp. 3671 - 3681, July 2014.

[8] H. Xiao, Z.Li, and C. Yang, " Robust stabilization of a wheeled mobile robot using model predictive control based on neurodynamics optimization," *IEEE Transactions on Industrial Electronics*, vol. 64, no. 1, pp. 505 - 516, Jan. 2017.

[9] Liu, K. Z. and T. Kanahara, "Steering control of vehicles by discontinuous control approach," *in Proc. 2001 Amer. Contr. Conf.* , Arlington, TX, June 2001, pp. 1521–1526.

[10] D. Rotondo, V. Puig, and F. Nejjari, "A fault-hiding approach for the switching quasi-LPV fault-tolerant control of a four-wheeled omnidirectional mobile robot," *IEEE Transactions on Industrial Electronics*, vol. 62, no. 6, pp. 3932 - 3944, June 2015.

[11] C. Samson, "Control of chained systems application to path following and time-varying point-stabilization of mobile robots," *IEEE Transactions on Automatic Control*, vol. 40, no. 1, pp. 64 - 77, Jan. 1995.

[12] D. Chwa, "Tracking control of differential-drive wheeled mobile robots using a backstepping-like feedback linearization," *IEEE Transactions on Systems, Man, and Cybernetics - Part A: Systems and Humans*, vol. 40, no. 6, pp. 1285 - 1295, Nov. 2010.

[13] C. Yang, Z. Li and R. Cui, " Neural network-based motion control of an underactuated wheeled inverted pendulum model," *IEEE Transactions on Neural Networks and Learning Systems*, vol. 25, no. 11, pp. 2004 - 2016, Nov. 2014.

[14] S. Wei, K. Uthaichana and M. Žefran, "Hybrid model predictive control for the stabilization of wheeled mobile robots subject to wheel slippage," *IEEE Transactions on Control Systems Technology*, vol. 21, no. 6, pp. 2181 - 2193, Nov. 2013.

[15] Dr. Robot Networks Available: http://www.drrobot.com/

[16] Y. Huang, X. Li ,P. Wang , L. Wei, and M. Jiang, " Mixed fuzzy sliding mode three-dimensional trajectory tracking control for a wheeled mobile robot," *in Proc. 32nd Youth Academic Annual Conference of Chinese Association of Automation*, Hefei, China, May 2017, pp. 5–9.

[17] M. Ghiasvand and K. Alipour, " Formation control of wheeled mobile robots based on fuzzy logic and system dynamics," *in Proc. 2013 13th Iranian Conference on Fuzzy Systems*, Qazvin, Iran, Aug. 2013, pp. 1–6.

[18] S.Duan, Y. Li, S. Chen, L. Chen, L. Zou, Z. Ma, and J. Ding, "Study of obstacle avoidance based on fuzzy planner for wheeled mobile robot," *in Proc. 2011 9th World Congress on Intelligent Control and Automation*, Taipei, Taiwan, June 2011, pp. 672 - 676.

[19] C. U. Dogruer, "Optimal trajectory tracking under parametric uncertainty," *in Proc. 2015 IEEE International Conference on Advanced Intelligent Mechatronics*, Busan, South Korea, July 2015, pp. 706 - 712.

[20] C.-T. Lee, B.-R. Su, and C.-H. Chang, T.-Y. Hsu, and W.-D. Lee, " Applications of Taguchi method to PID control for path tracking of a wheeled mobile robot," *in Proc. 2018 IEEE International Conference on Applied System Invention*, Chiba, Japan, April 2018, pp. 453 - 456.

Gwo-Ruey Yu received the Ph.D. degree in Electrical Engineering from the University of Southern California, Los Angeles, in 1997. He is currently a Professor of Electrical Engineering Department and the Director of Elegant Power Application Research Center, National Chung Cheng University, Taiwan. Dr. Yu is respectively the recipients of the Best Paper Award of IEEE 2017 International Automatic Control Conference, the Advisor Award of Robotic Society of Taiwan in 2018, the Best Paper Award in Application of IEEE 2016 International Conference on Fuzzy Theory and It's Applications, the Outstanding Paper Award of IEEE 2016 International Automatic Control Conference, the Best Paper Award of 2018 International Conference on Advanced Robotics and Intelligent Systems. His research interests include intelligent robots, automatic control based on artificial intelligence, and renewable energy systems.

Yu-Shan Chiu received the B.S. degree from Chung Yuan Christian University, Taoyuan City, Taiwan, in 2017. She is currently a student at Graduate Institute of Opto-Mechatronics, National Chung Cheng University, Chia-Yi, Taiwan. She received the Second Place Prize of the Best Paper Award of 2018 International Conference on Advanced Robotics and Intelligent Systems, in 2018. Her research interests include intelligent robots, fuzzy systems, and intelligent control.

Image Recognition and Pick-up Execution of a Robotic Dual-Arm System for Automatic Shoe Sewing

Han-Lin Hsu, Ching-Chih Tsai, and Feng-Chun Tai

Abstract-**This paper presents techniques for object recognition and pick-up execution a robotic dual-arm shoe-sewing system. For object recognition, a bracket image will be set as a reference image for comparison and recognition. According to the image acquired from a RGB-D sensor, the Oriented Fast and Rotated BRIEF (ORB) method is used to find the features in reference images. Image process is executed for finding the specified color in the holding position. The coordinates of the bracket are transformed into the robotic coordinates for the pick-up mission. Experimental results are conducted to show the effectiveness of the proposed image recognition and task execution method for the robotic dual-arm shoe-sewing system.**

Index Terms—**Automatic shoe sewing, dual seven degrees-of-freedom (7-DOF) robotic arms, image processing, image recognition.**

I. INTRODUCTION

SHOE sewing industry is a labor-intensive industry, which relies heavily on a lot of labors to complete the sewing process. Since the manufacturing process is complicated and sophisticated, practitioners need to sew all the small pieces together step by step. Recently, the shortage and rising cost of labors have motivated manufacturers to adopt automatic shoe sewing by using robots and automatic equipment. Consequently, research in automatic sewing with robotic arms have become increasingly important and have provided more acquaintance in sewing automation.

Recently, many researchers and practitioners have paid significant efforts on reducing labor cost as well as improving product quality for labor-intensive shoe-sewing industry which relies heavily on a lot of labors to complete the sewing process. The authors in [1] proposed a robotic dual-arm system for automatic shoe sewing. In order to implement the robotic dual-arm system for automatic show sewing, the image recognition for robotic dual-arm is required to pick up the object. The authors in [2] presented a scale and rotation invariant feature detection method, where the integral image was used for improving the computation speed and the interest point is detected by Hessian matrix, and the process in image pyramid was used to increase the scale invariant and Haar wavelet response was computed to obtain the descriptor. In [3], a feature for object detection, called ORB, was implemented in computer vision. This feature keypoint and descriptor were shown good for its rotation invariant and resistant to noise. Furthermore, the experiment of this method showed a good real-time performance result by comparing to other existing method. The study in [4] implemented a dual-arm system for the task of coffee making. The images from the stereo vision camera on the robotic head was processed to obtain the object position by the coordinate transformation. Moreover, the robotic dual-arm system was shown to cooperate to accomplish the procedure. In [5], a humanoid 6-DOF robotic arm was employed to execute the grasping action based on the vision of the Kinect. The process of the depth image completed the image segmentation in order to find a proper plane; afterward, the speed up robust feature (SURF) detector was used to find the object in the plane according to the database. Furthermore, considering the obstacle avoidance, the potential field was used in the motion planning. The authors in [6] showed the most popular edge detector suited for noise-interrupted images. The detector filtered the images by a Gaussian filter first and the Sobel operator was used to find the gradient. Then non-maximum suppression and Hysteresis threshold was used to filter out some error edge, and, the Canny edge detector, which is a low error rate edge detector, was utilized.

Inspired by the aforementioned investigations [1-6], this paper aims to propose methodologies and techniques for object recognition in order to pick up the stitching objects that are ready for sewing. By comparing to existing systems for the automatic shoe-sewing process, the proposed method and systems is novel in using 7-DOF robotic dual-arms to replace human two hands and devising an automatic object recognition method for recognizing stitching objects via a RGB-D camera. The proposed method and built system may provide references for professionals working in the field of the automatic shoe-sewing process.

The rest of this paper is constructed as follows. The proposed system structure and description is stated in Section II. Section III addresses image recognition by ORB feature extraction, feature descriptor and feature matching. Section IV delineates the image processing technique from the RGB-D camera including the color space transformation, edge detector and morphological operation. Furthermore, the approach of coordinate transformation is used to achieve task of picking up the bracket. In Section V, experiments are conducted to verify the effectiveness and practicality of the proposed method. Section VI concludes the paper.

II. SYSTEM STRUCTURE AND DESCRIPTION

This section will introduce an overall system structure of the proposed robotic dual-arm shoe-sewing system. The dual arms

---

Han-Lin Hsu, Ching-Chih Tsai, and Feng-Chun Tai are with the Department of Electrical Engineering, National Chung Hsing University, Taichung 40227, Taiwan.

(Corresponding author Ching-Chih Tsai, email: cctsai@nchu.edu.tw)

(email: stanleyfreeze@gmail.com, d099064008@mail.nchu.edu.tw)

The authors gratefully acknowledge financial support from the Ministry of Science and Technology, Taiwan, the R.O.C., under contract MOST 106-2218-E-005-003-.

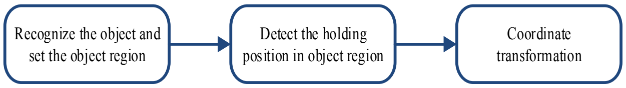

Fig. 1. Flow chart of the image process.

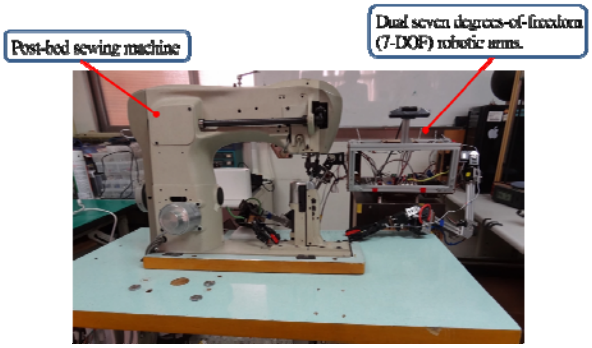

Fig. 2. Picture of the robotic dual-arm shoe-sewing system.

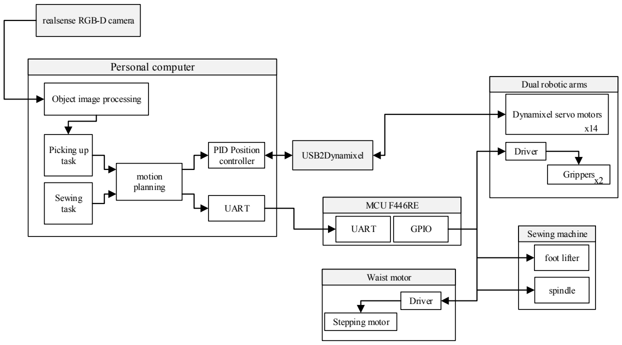

Fig. 3. Overall control system and signal flowchart of the shoe-sewing system.

and post-bed sewing machine are briefly described. Particular effort will be paid to describe the overall system architecture and signal flows of the experimental system. Fig. 1 shows the flow chart of the image recognition and process.

Fig. 2 illustrates a picture of the proposed automatic shoe sewing system, and Fig. 3 depicts the overall control system architecture and signal flowchart of the proposed system. In Fig. 3, the personal computer (PC) serves as the main control unit of the overall control system. The task program and image process will be implemented in this computer. The tasks for automatic shoe sewing is divided into two parts: one is for object recognition and picking up task, and the other is for the sewing task.

For the object recognition and pick-up task, the image streams obtained from the Realsense RGB-D sensor and process in the PC will be executed first. Then motion planning block start to generate the corresponding motion for the task with the PID position controller. Afterwards, the motion planning result is sent to the dual-arms through USB2Dynamixel adaptor. If the peripheral device control is necessary, the command will be sent to device through the F446RE microcontroller such as gripper on the robotic arm, waist motor, and sewing machine. The stepper motors and gripper will be driven by the corresponding drivers. Finally, the system can be executed with this control system and architecture.

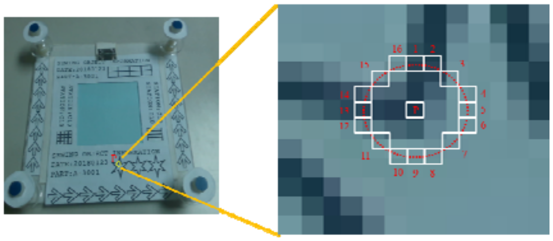

Fig. 4. Illustration of one FAST keypoint.

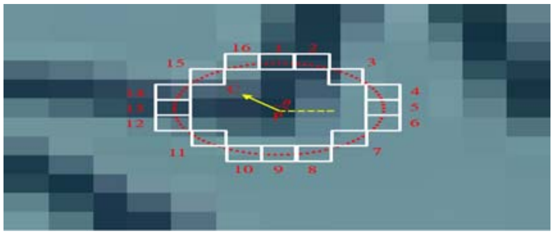

Fig. 5. Orientation in the FAST algorithm.

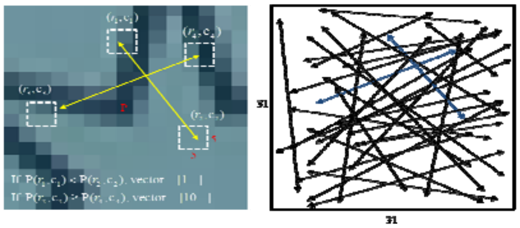

Fig. 6. Binary string from BRIEF.

III. IMAGE RECOGNITION WITH ORB

This section presents image recognition in order to pick up the stitching object that is ready for sewing. An object image will be set as a reference image for comparison and recognition. By using Oriented Fast and Rotated BRIEF (ORB), it is easy to find the features in reference image and transfer to binary descriptor. A kind of RGB-D camera, called Realsense, is installed on the top of the 7-DOF robotic dual-arms. The RGB-D camera is used as the vision system for the 7-DOF robotic dual-arms. Thus the images acquired from the RGB-D camera is the source for the image processing. These images are then compared to the reference image in order to find the sewing object in the view as the waist rotation. After the object detection, the pixel outside the object region will be cleared and the holding position in the object region is detected by the image process. Finally, the coordinate transformation obtains the coordinate in the robot frame for the robotic dual-arms to pick up the stitching object which is ready for sewing.

3.1 Oriented Feature from Accelerated Segment Test

Feature from Accelerated Segment Test (FAST) is a method to find keypoints. The principle of the FAST algorithm is to compare the intensities in the center and the intensity around the circle. If the differences exceed the threshold, then it will be considered as a keypoint. Fig. 4 shows the FAST keypoint.

Oriented FAST (oFAST) is constructed by adding the orientation to the FAST keypoint. The intensity centroid C is calculated using (1) and (2), and the orientation value is computed by (3). The orientation is shown in Fig. 5.

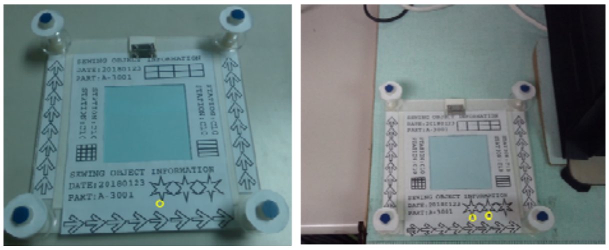

Fig. 7. Example for the two nearest descriptors.

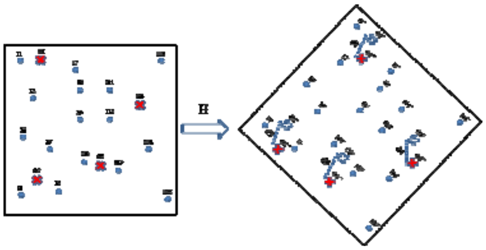

Fig. 8. Some incorrect matches in two images.

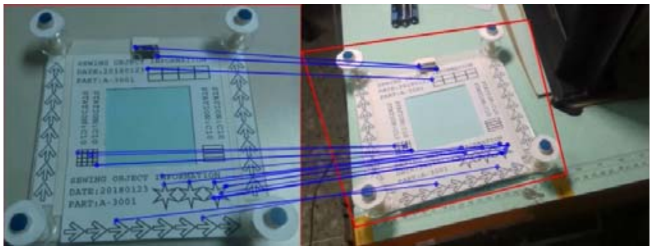

Fig. 9. Inliers between the images.

$$m_{pq} = \sum_{x,y} x^p y^p I(\mathrm{x},\mathrm{y}) \tag{1}$$

$$C = \left(\frac{m_{10}}{m_{00}}, \frac{m_{01}}{m_{00}} \right) \tag{2}$$

$$\theta = \mathrm{atan2}(\mathrm{m}_{01}, \mathrm{m}_{10}) \tag{3}$$

3.2 Binary Robust Independent Elementary Feature

After the feature keypoint is detected, one should calculate the descriptor for this keypoint in order to execute the feature matching. The Binary Robust Independent Elementary Feature (BRIEF) is a bit string description of an image patch constructed from a set of binary intensity tests. A binary test τ is defined by:

$$\tau(\mathrm{p;x,y}) = \begin{cases} 1 \ : p(\mathrm{x}) < \mathrm{p(y)} \\ 0 \ : p(\mathrm{x}) \ge \mathrm{p(y)} \end{cases} \tag{4}$$

where p(x) is the intensity of p at a point x. The feature is defined as a vector of n binary tests:

$$\mathrm{f}_n(\mathrm{p}) = \sum_{1 \le i \le n} 2^{i-1} \tau(\mathrm{p}; \mathrm{x}_i; \mathrm{y}_i) \tag{5}$$

Fig. 6 shows point pairs in the binary descriptor calculation. For the rotation invariance, the steered BRIEF algorithm is employed to rotate the point pairs where is the rotation angle of the oFAST keypoint.

$$S = \begin{pmatrix} x_1, \cdots, x_n \\ y_1, \cdots, y_n \end{pmatrix} \tag{6}$$

$$S_\theta = R_\theta S \tag{7}$$

In order to obtain high variance and reduce correlation of the steered BRIEF, a rotaion-awared (rBRIEF) algorithm for finding the proper point pair position is adopted in the following steps.

Step 1: Find all possible 5x5 sub-window pairs in 31x31 patch for each keypoint, given the training set containing K keypoints. Note that there are M possible sub-window pairs in a 31x31 patch for each keypoint as shown in (8).

$$\begin{aligned} &Patch1: [b_{11}\ b_{12} \cdots b_{1M}] \\ &Patch2: [b_{21}\ b_{22} \cdots b_{2M}] \\ &\qquad \vdots \\ &PatchK: [b_{k1}\ b_{k2} \cdots b_{kM}] \end{aligned} \tag{8}$$

Step 2: Calculate the distance from mean of 0.5 for binary string in each patch as shown in (9).

$$\begin{aligned} &mean(b_{11}\ b_{12} \cdots b_{1M}) = \mathrm{m}_1 \\ &mean(b_{21}\ b_{22} \cdots b_{2M}) = \mathrm{m}_2 \\ &mean(b_{31}\ b_{32} \cdots b_{3M}) = \mathrm{m}_3 \\ &\qquad \vdots \\ &mean(b_{k1}\ b_{k2} \cdots b_{kM}) = \mathrm{m}_k \end{aligned} \tag{9}$$

Step 3: Obtain the matrix T from the order of the mean of each patch m_1, m_2, m_3, …, m_k. Assume the result is $m_2 < m_1 < m_3 < \ldots$, the order of the patch will be rearranged to (10).

$$\begin{aligned} &Patch2: [b_{21}\ b_{22} \cdots b_{2M}] \\ &Patch1: [b_{11}\ b_{12} \cdots b_{1M}] \\ &Patch3: [b_{31}\ b_{32} \cdots b_{3M}] \\ &\qquad \vdots \end{aligned} \tag{10}$$

Step 4: Put the first column $[b_{21}\ b_{11}\ b_{31} \cdots]^T$ to matrix R and remove the first column of T as shown in (11) . Next compare the column $[b_{22}\ b_{12}\ b_{32} \cdots]^T$ in T against all column in R. If the correlation is less than threshold, move the column from T to R as shown in (12), otherwise just remove it from T. Repeat the procedure until there are 256 columns in R as shown in (13) . The result can be used to be the point position for the pair position.

$$T = \begin{bmatrix} b_{21}\ b_{22} \cdots b_{2M} \\ b_{11}\ b_{12} \cdots b_{1M} \\ b_{31}\ b_{32} \cdots b_{3M} \\ \vdots \end{bmatrix} \quad R = \begin{bmatrix} b_{21} \\ b_{11} \\ b_{31} \\ \vdots \end{bmatrix} \tag{11}$$

$$T = \begin{bmatrix} b_{22} \cdots b_{2M} \\ b_{12} \cdots b_{1M} \\ b_{32} \cdots b_{3M} \\ \vdots \end{bmatrix} \quad R = \begin{bmatrix} b_{21} & b_{22} \\ b_{11} & b_{12} \\ b_{31} & b_{32} \\ \vdots & \vdots \end{bmatrix} \tag{12}$$

$$T = \begin{bmatrix} \cdots b_{2M} \\ \cdots b_{1M} \\ \cdots b_{3M} \\ \vdots \end{bmatrix} \quad R = \begin{bmatrix} b_{21} & b_{22} & \cdots \\ b_{11} & b_{12} & \cdots \\ b_{31} & b_{32} & \cdots \\ \vdots & \vdots & \vdots \end{bmatrix} \tag{13}$$

3.3 Match Descriptor

After the feature descriptors are generated, the descriptor between source image and the destination image should be matched. The brute-force approach is used to match the descriptor. It takes the descriptor of one feature in source image and is matched with all other descriptors in the second set using some distance calculation. Hamming distance is adopted for distance calculation, aiming at discriminating the similarity

Fig. 10. Clearing pixel out of the boundary box.

between the descriptors. As the distance between a descriptor pair is close, then the similarity degree becomes high. The k-nearest-neighbor matching is used with k being 2. With this method, the nearest 2 matching descriptors in the destination image will be considered a candidate matching descriptor. After k-nearest-neighbor matching, a ratio between the two nearest descriptors is calculated to verify whether it is a good matching descriptor or not.

$$\text{Distance ratio}= d_1 / d_2 \tag{14}$$

If the distance ratio is smaller than the threshold value, then it is a matching descriptor. Note that the threshold value of the distance ratio is usually set by 0.8. For example, Fig. 7 shows the keypoint in the left image, and there are 2 nearest keypoint descriptors in the right image. These descriptors can be sifted according to the aforementioned distance ratio.

3.4 Find Homography by RANSAC

After finding the feature descriptor, these features of the object in the different images can be related using a transformation. The relationship can be described through a homography transformation matrix H as shown in (15). A point in source image as (x,y) can be transformed to the point $(x^{'},y^{'})$ in a destination image. At least 4 point pairs should be given in order to solve the parameter in the matrix H.

$$\begin{bmatrix} x' \\ y' \\ 1 \end{bmatrix} = H \begin{bmatrix} x \\ y \\ 1 \end{bmatrix} = s \begin{bmatrix} h_{11} & h_{12} & h_{13} \\ h_{21} & h_{22} & h_{23} \\ h_{31} & h_{32} & h_{33} \end{bmatrix} \begin{bmatrix} x \\ y \\ 1 \end{bmatrix} \tag{15}$$

Some of the matched keypoints in the two images are not correct. In Fig. 8, two images contains the relationship by the homography transformation matrix H. The correct matched points are marked in circles and assigned I1 to I15. Otherwise, the incorrect matched points are marked as “x” and assigned from O1 to O4. Because some of the matched keypoints in the two images are incorrect, the random sample consensus (RANSAC) algorithm is adopted to solve the homography matrix. First, choose 4 keypoint matches randomly, and solve the first homography matrix H. Second, transform all the points by the matrix H to get desired points and compare these desired points with real points in images. If the distances between the desired points and real points are less than threshold, the points are correct points which also are called inliers. Otherwise, if the distances are higher than the threshold, the points are incorrect points which are called outliers. The quantity of the inliers will be recorded. The next iteration will start to execute the process again. If the next iteration gets a higher quantity of the inliers, the record will be substituted. After a specified iteration time, the H matrix will approach the correct matrix. Fig. 9 shows the experimental results of the inliers between the images.

IV. PICKING BRACKET WITH OBJECT RECOGNITION

The purpose of this section is to investigate how to detect the holding place after the object is detected in the camera view by a series of image process. Afterwards, the coordinate transformation for obtaining the position in the robot frame is used to implement the task of pick up the object.

4.1 Finding the Specified Color Region

The object recognition has been done in the last section. The object is filtered out in the image by the boundary box and the pixel out of the boundary box is set to black as shown in Fig. 10. The corner of the object is marked in blue circle. The purpose is to filter out the blue corner here. In order to be better for perception of color than (Red, Green, Blue) RGB color space in the image. Hue, Saturation, Value (HSV) color space is adopted. HSV color space separates hue, saturation, and intensity value. The range of hue is from 0° to 360°. Saturation and intensity value ranges from 0 to 1. Thus a good hue range is selected to find desired object color region.

After transformation to the HSV space, the binary image can be obtained by checking whether the pixels in the image is in the specified HSV range. If the pixel is in the range for each HSV parameter, then the pixel is set to 255 in each channel. Otherwise, the channel in the pixel will be all set to 0. The hue parameter range is set from 99 to 122. The saturation parameter is from 52 to 244. The value is 43 to 208. Fig. 11 depicts the result of extracting the blue corner where the four corners of the object were found. However, a little noise occurs between the two corners in the bottom. Thus the following morphological operation is used to eliminate these noises.

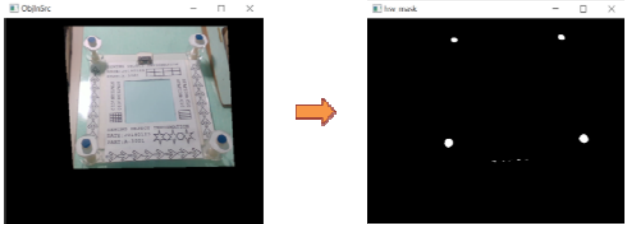

Fig. 11. Result of extracting blue corner.

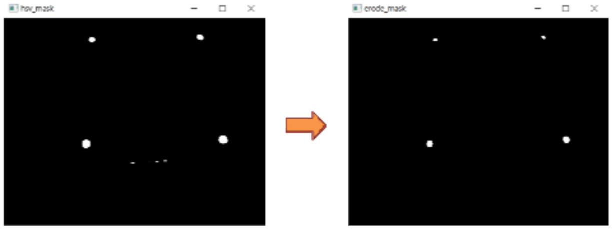

Fig. 12. Erosion process in object image.

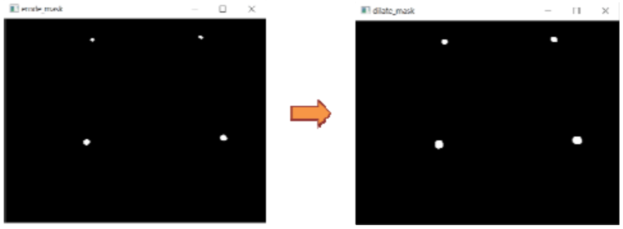

Fig. 13. Dilation process in object image.

4.2 Morphological Operation

In this subsection, the morphological operation is used to reduce the noise in the binary image. Two kinds of morphological operations are used here: erosion and dilation. The following description is the erosion operation. First, choose a 3x3 pixels kernel and move the kernel to all pixels in the picture. An anchor point is the point in the center of kernel. Next, compute a local minimum over the area of the kernel and replace the anchor point with this local minimum value. For dilation operation, use the same process with the erosion operation, but the anchor point will be replaced with the local maximum value. Fig. 12 shows the object image after the erosion operation. The noise in the bottom for the two corners can be reduced. Afterwards, Fig. 13 shows the dilation process and makes the size of the corner dilate to the original size.

4.3 Canny Edge Detector

In this subsection, the Canny edge detector will be introduced. After the morphological operation, the Canny edge detector is used to find the edge of the objector corner. The Canny edge detector is executed as the following steps.

Step 1: filter out the noise by the Gaussian filter kernel in (16).

$$\mathrm{K}=\frac{1}{159}\begin{bmatrix}2 & 4 & 5 & 4 & 2\\ 4 & 9 & 12 & 9 & 4\\ 5 & 12 & 15 & 12 & 5\\ 4 & 9 & 12 & 9 & 4\\ 2 & 4 & 5 & 4 & 2\end{bmatrix} \tag{16}$$

Step 2: calculate the intensity gradient by executing convolution to the image I with the Sobel operator via (17) and (18).

$$\mathrm{G}_x=\begin{bmatrix}-1 & 0 & 1\\ -2 & 0 & 2\\ -1 & 0 & 1\end{bmatrix},\mathrm{G}_y=\begin{bmatrix}-1 & -2 & -1\\ 0 & 0 & 0\\ 1 & 2 & 1\end{bmatrix} \tag{17}$$

$$g_x=I*G_x,g_y=I*G_y \tag{18}$$

Step 3: compute the gradient strength and direction via (19), and Fig. 14 shows the result of the used the Canny edge detector.

$$\mathrm{g}=\sqrt{\mathrm{g}_x{}^2+\mathrm{g}_y{}^2},\theta=\arctan(\frac{g_y}{g_x}) \tag{19}$$

Step 4: find the center coordinates via the image moment via (21).

$$m_{ji}=\sum_{x,y}I(\mathrm{x,y})\cdot\mathrm{x}^j\cdot\mathrm{y}^i \tag{20}$$

$$cen_x=\frac{m_{10}}{m_{00}},cen_y=\frac{m_{01}}{m_{00}} \tag{21}$$

4.4 Coordinate Transformation

After finding the coordinates of the object corner on the image, the depth is detected from the RGB-D sensor depth frame, where Fig. 15 shows the depth frame of the RGB-D camera. The coordinates should be transformed from the camera coordinate frame to the image coordinate frame. Fig. 16 shows the RGB-D camera position related to the robot frame coordinate in the physical structure. The origin of the robot frame is in the middle of the first axis of the dual arms. LH1 means the length from origin to the back of the camera, LH2 is the length from back of camera to the axis of camera, and LH3 is defined from the axis of camera to the front of the camera. Fig. 17 illustrates the robot frame to the RGB-D camera frame with the joint information shown in the DH table. We fixed the rotational angle θ_h of the RGB-D camera as $-50°$ .Via the homogeneous transformation matrix, the transform matrix ${}^0T_{camera}$ is calculated in (22). (23) transforms the position on top surface of the holding place in the robot frame $(x_o,y_{o,}z_o)$ from that in the camera frame $(x_{cam},y_{cam,}z_{cam})$. Note that z_{offset} is offset between top surface and holding point.

$$\begin{aligned}{}^0T_{camera}={}^0A_{p1}\cdot{}^{p1}A_{p2}\cdot{}^{p2}A_{p3}\cdot{}^{p3}A_{p4}\cdot{}^{p4}A_{camera}&=\begin{bmatrix}1 & 0 & 0 & 0\\ 0 & 1 & 0 & 0\\ 0 & 0 & 1 & LH1\\ 0 & 0 & 0 & 1\end{bmatrix}\begin{bmatrix}1 & 0 & 0 & LH2\\ 0 & 1 & 0 & 0\\ 0 & 0 & 1 & LH1\\ 0 & 0 & 0 & 1\end{bmatrix}\\ &\begin{bmatrix}1 & 0 & 0 & 0\\ 0 & 0 & -1 & 0\\ 0 & 1 & 0 & 0\\ 0 & 0 & 0 & 1\end{bmatrix}\begin{bmatrix}\cos\theta_H & 0 & -\sin\theta_H & LH3\cdot\cos\theta_H\\ \sin\theta_H & 0 & \cos\theta_H & LH3\cdot\sin\theta_H\\ 0 & -1 & 0 & 0\\ 0 & 0 & 0 & 1\end{bmatrix}\begin{bmatrix}0 & 0 & 1 & 0\\ -1 & 0 & 0 & 0\\ 0 & -1 & 0 & 0\\ 0 & 0 & 0 & 1\end{bmatrix}\end{aligned} \tag{22}$$

$$\begin{bmatrix}x_o\\ y_o\\ z_o\\ 1\end{bmatrix}={}^0T_{camera}\begin{bmatrix}x_{cam}\\ y_{cam}\\ z_{cam}\\ 1\end{bmatrix}-\begin{bmatrix}0\\ 0\\ z_{offset}\\ 1\end{bmatrix} \tag{23}$$

TABLE I. THE DH PARAMETERS OF THE ROBOT FRAME

Joint	θ_{home}	d_j	a_j	α_j	θ_i
P1	0	LH1	0	0	None
P2	0	0	LH2	0	None
P3	0	0	0	90	None
P4	0	0	LH3	90	θ_h
Image	-90	0	0	90	None

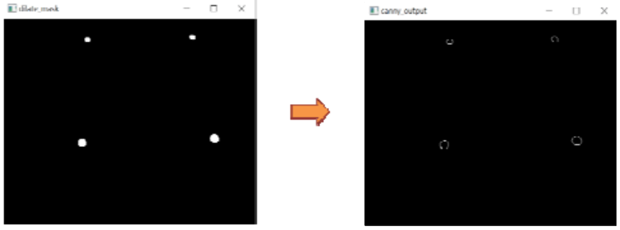

Fig. 14. Result of Canny edge detector.

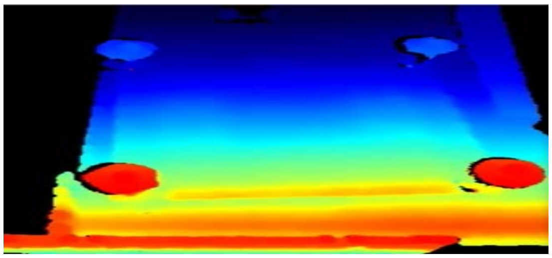

Fig. 15. Depth frame from GRB-D sensor.

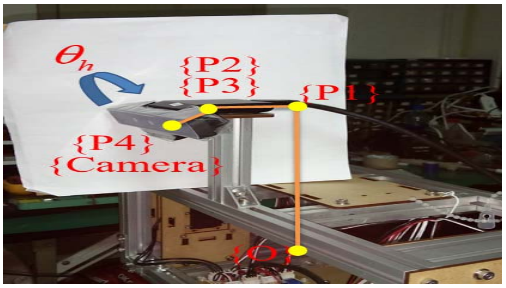

Fig. 16. RGB-D camera in physical structure.

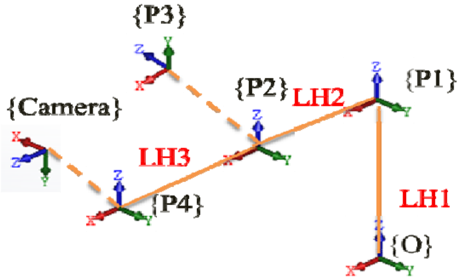

Fig. 17. Coordinate frame of the RGB-D camera in the robot.

V. EXPERIMENTAL RESULTS AND DISCUSSION

This section conducts two experiments to examine the effectiveness of the image recognition and task execution of picking up the bracket. The first experiment aims to verify the proposed object detection scheme by the RGB-D camera. The experiment is described in the following. First of all, the waist of the robot was set to an initial position that cannot detect the target object. A reference object image was preset for the recognition. Next, the waist motor got started for rotation. In the meantime, the video stream acquiring from the RealSense RGB-D camera were executed to carry out the object recognition process continuously. The waist motor continued to rotate until the object was detected and the coordinates of the object corner were calculated. Furthermore, the coordinates in the x direction of the left bottom corner and the right bottom corner should close to each other. Thus the task for picking up the object was accomplished. In this experiment, the object was detected by the image recognition method and the corner coordinates were found as shown in Fig. 18. Thus, the waist motor stopped in the desired position and the result validated the effectiveness of the method.

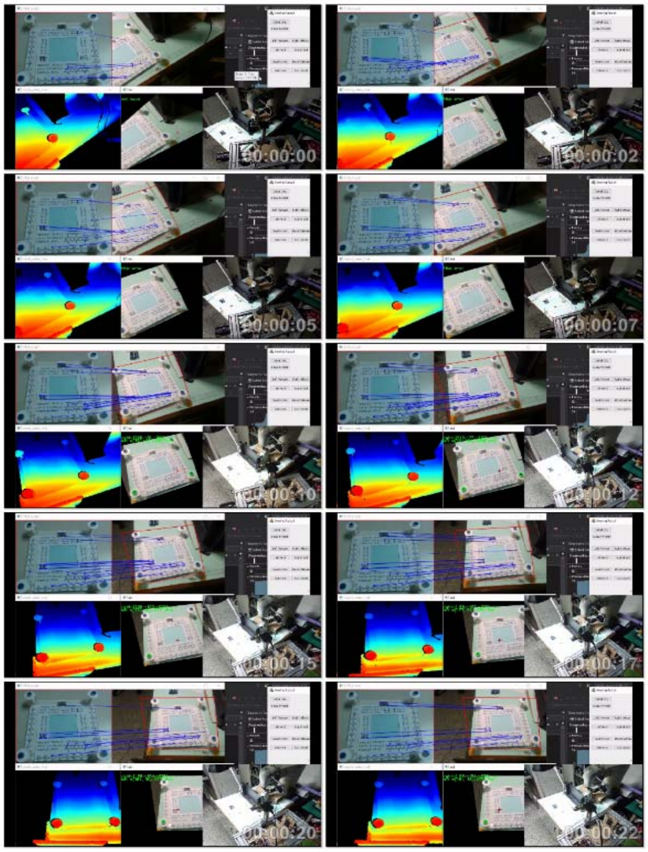

Fig. 18. Experimental results of finding the bracket.

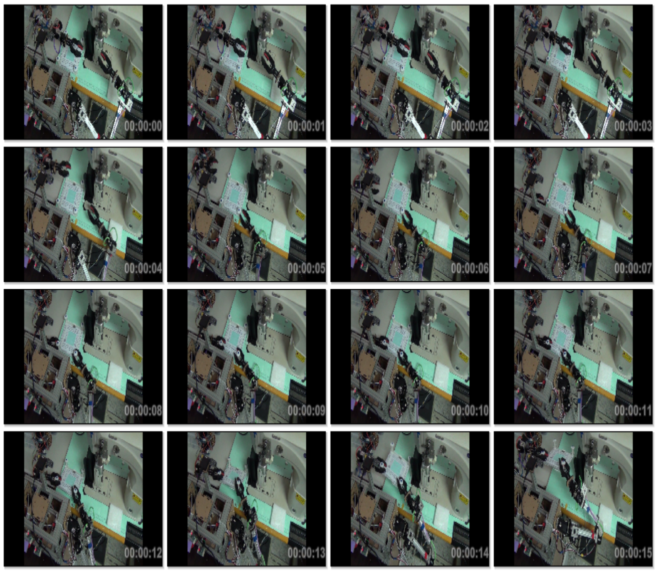

Fig. 19. Experimental results of picking up the bracket.

The second experiment is carried out to examine the pick-up of the desired stitching object. The procedure is delineated as follows. First, the coordinates in the corners of the left bottom and right bottom were found using the image process, and the dual arms were then controlled to move toward the positions nearby the corner coordinates first. Afterwards, the dual arms were moved to the centers of the holding place along a line trajectory in both right and left arms, respectively. Finally, the grippers grasped the object, and then the dual arms moved upward in the z direction to pick up the bracket. Fig. 19 illustrates the still pictures of movements while executing the pick-up task. The results in Fig. 19 indicates the success of the proposed pick-up procedure for the desired object.

VI. CONCLUSIONS AND FUTURE WORK

The paper has presented techniques using image recognition and pick-up execution for the autonomous shoe-sewing procedure with a robotic dual-arm system. The experimental robotic system has been built by equipping with two 7-DOF arms, one microcontroller, one Realsense RGB-D sensor, and one personal computer used for image recognition and motion control of the dual arms. In particular, the microcontroller has been used for the peripheral devices such as waist motor, grippers and sewing machine signal communication. The proposed object recognition techniques, including ORB feature detector combined with morphological operations, has been used in the experiments of object recognition and pick-up. The image recognition has been successfully applied to detect the object from the reference image and obtain the coordinates in the corner by the depth values from the Realsense RGB-D camera and coordinate transformation. Finally, the task of pick-up bracket has been done successfully. An interesting topic for future work would be to propose a more real-time task execution system that avoids any collisions between the dual-arm system and post-bed sewing machine.

REFERENCES

[1] H. L. Hsu, C. C. Tsai, and F. C. Tai, "Path Planning and Motion Control of a Robotic Dual-Arm System for Automatic Shoe Sewing," in *Proc. of 2018 International Conference on Systems Sciences and Engineering*, National Taipei University, New Taipei City, Taiwan, 28-30 June, 2018.

[2] H. Bay, A. Ess, T. Tuytelaars, and L. Van Gool, "Speeded-up robust features (SURF)," *Computer vision and image understanding* 110, (2008): 346-359.

[3] E. Rublee, V. Rabaud, K. Konolige, and G. Bradski, "ORB: an efficient alternative to SIFT or SURF," in *Proc. 2011 IEEE International Conference on Computer Vision* (ICCV), Barcelona, Spain, 6-13 Nov 2011.

[4] T. T. Liang, *Autonomous Task Execution of a Two-Armed Robot with Stereo Vision Camera*, MS Thesis, Department of Electrical Engineering, National Chung Hsing University, July 2010.

[5] S. C. Tsai, *Vision-Based Design for Adaptive Grasping of a Humanoid Robot Arm*, MS Thesis, Institute of Electric and Control Engineering, National Chiao Tung University, Oct 2011.

[6] J.F. Canny, "A computational approach to edge detection, " *IEEE Transactions on Patter Analysis and Machine Intelligence*, 8(6), pp.679-698,1986.

[7] Y. S. Wang, *Mechatronic design, motion planning and cooperation of an anthropomorphous two-armed robot*, MS Thesis, Department of Electrical Engineering, National Chung Hsing University, June 2009.

[8] C. H. Li, *Driving System Design and Two-Dimension Bar Tacking Function Control of an Industrial Sewing Machine*, MS Thesis, Department of Electrical Engineering, National Chung Hsing University, January 2017.

[9] Z. Y. Tsai, *Machine vision based servo control of a robotic sewing system*, MS Thesis, Department of Mechanical Engineering, National Yunlin University of Science & Technology.

[10] C. Harris and M. Stephens, "A combined corner and edge detector," Plessey Research Roke Manor, United Kingdom, The Plessey Company pic., 1988.

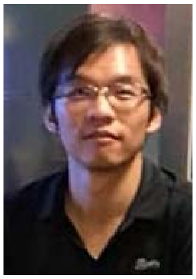

Han-Lin Hsu received the B.S. and M.S. degrees in the Department of Electrical Engineering, National Chung Hsing University, Taichung, Taiwan, ROC, in 2016 and 2018, respectively. His current research interests include mechatronics, intelligent control, intelligent computing and intelligent robotics with their applications to smart machinery.

Ching-Chih Tsai received the Diplomat in Electrical Engineering from National Taipei Institute of Technology, Taipei, Taiwan, ROC, the MS degree in Control Engineering from National Chiao Tung University, Hsinchu, Taiwan, ROC and the Ph.D degree in Electrical Engineering from Northwestern University, Evanston, IL, USA, in 1981, 1986 and 1991, respectively. Currently, he is currently a Distinguished Professor in the Department of Electrical Engineering, National Chung-Hsing University, Taichung, Taiwan, where he served the Chairman in the Department of Electrical Engineering from 2012 to 2014. He is a Fellow of IEEE, IET and CACS.

Dr. Tsai served as the Chair, Taipei Chapter, IEEE Control Systems Society, from 2000 to 2003, and the Chair, Taipei Chapter, IEEE Robotics and Automation Society from 2005 to 2006. In 2007, he was the program chair of 2007 CACS international automatic conference sponsored by Taipei chapter, IEEE control systems society. In 2010, he served as the program co-chair of SICE 2010 annual conference in Taiwan, which was technically sponsored by IEEE CSS; in 2011, he served as the General Chair, 2011 International conference on service and interactive robotics; in 2012, he has served as the General Chair, 2012 International conference on Fuzzy Theory and Its Applications, the General Chair, 2012-2015 CACS International Automatic Control Conferences, and the General Chair, 2016-2017 International Conference on Advanced Robotics and Intelligent Systems. Dr. Tsai served the two-term President, Chinese Institute of Engineers in Central Taiwan, Taiwan from 2007 to 2011, and two-term President of Chinese Automatic Control Society from 2012 to 2015. Since 2008, he has been the Executive Directors in Boards of Government of thee professional associations, including Robotic Society of Taiwan, Taiwan Fuzzy Systems Association, and Taiwan Systems Association. He has served as the Chair, Taichung Chapter, IEEE Systems, Man, and Cybernetics Society since 2009, the Chair of IEEE SMC Technical Committee on intelligent learning in control systems since 2009, the President of Robotics Society of Taiwan since 2016, the steering committee of Asian Control Association since 2014, a BOG member of IEEE Nanotechnology council since 2012, the Vice President of International Fuzzy Systems Association since 2015, and a BOG member of the IEEE SMCS since 2017.

Dr. Tsai has published more than 500 technical papers, and seven patents in the fields of control theory, systems technology and applications. Web of Science has indexed his paper entitled "Adaptive Neural Network Control of a Self-Balancing Two-Wheeled Scooter" in the category Automation Control Systems, where the paper was ranked 408 out of 37607 articles (published between 2010 to 2014). Dr. Tsai is respectively the recipients of the Third Society Prize Paper Award from IEEE Industry Application Society in 1998, the Outstanding Automatic Control Engineering Award in 2008 from Chinese Automatic Control Society (CACS), and the Outstanding Engineering Professor Award in 2009 from the Chinese Institute of Engineers in 2009, the IEEE Most Active SMC Technical Committee (TC) Award in 2012 from IEEE SMC Society, the Outstanding Electrical Engineering Professor Award from the Chinese Institute of Electrical Engineering in 2014, Outstanding Industry Contribution Award from Taiwan Systems Association in 2016, the best paper award in the International Journal of Fuzzy Systems in 2017, and many best paper awards from many international conferences technically supported by IEEE. He is the advisor, IEEE SMC student branch chapter at National Chung Hsing University; this chapter was the recipient of certificate of appreciation from IEEE SMCS in 2009. He has served as the associate editors of International Journal of Fuzzy Systems, and IEEE Transactions on Systems, Man and Cybernetics: Systems, IEEE Transactions on Industry Informatics, and

International Journal of Electrical Engineering. Recently, he has served as the Editor-in-Chief of a new international robotics journal called “iRobotics”. His current interests include advanced nonlinear control methods, deep model predictive control, fuzzy control, neural-network control, advanced mobile robotics, intelligent service robotics, intelligent mechatronics, intelligent learning control methods with their applications to industrial processes and intelligent machinery.

Feng-Chun Tai received the B.S., M.S. and Ph.D. degrees in Department of Electrical Engineering from National Chung Hsing University, Taichung, Taiwan, ROC. in 2007, 2010 and 2018, respectively. His current research interests include mobile robots, intelligent control, navigation system and their applications to industrial processes and machines.

Vibration Suppression of a 6-DOF Robot Manipulator based on Multi-mode Robust Input Shaping

Yean-Yia Lin, Zhi-Hao Kang, Hsiang-Yuan Ting and Han-Pang Huang, *Member, IEEE*

***Abstract* —This study addresses the vibration suppression of a multi-axis manipulator with the elastic joints. A feedforward/feedback control architecture with multi-mode robust input shaping is proposed. The feedforward control strategy is a zero time-delay input shaping with contour-error compensation, which not only compensates the contour error but also improves the disadvantage of the zero time-delay input shaping, and the polyreference least-squares complex frequency domain method (PolyMAX) is applied to estimate modal parameters. The feedback control strategy is a motor-side feedback control based on elastic-joint dynamics. In order to combine the feedforward and feedback controls, this study proposes a method based on the properties of convolution, and the first four derivatives of the shaped command can be calculated instead of numerical differentiation. The simulation and experimental results verify the performance of the proposed feedforward/feedback architecture for vibration suppression.**

***Index Terms*—Vibration suppression, Multi-Axis Manipulator, Input Shaping, Elastic-Joint Dynamics.**

I. INTRODUCTION

In recent years, industrial robots are designed to be lightweight to save the cost of the mechanisms, actuators, and energy required. In addition, a series elastic actuator (SEA) and a variable-stiffness joint have recently been used to facilitate safe cooperation and compliance control [38]. Moreover, a harmonic drive, a flexible component, is widely used to provide higher torque in the robot arm. However, resonance vibration will be generated in high-speed rest-to-rest motions, which leads to low levels of accuracy and precision in industrial applications. To achieve high accuracy in high-speed motions, the strategies to suppress the vibration are divided into the active and the passive. Common passive strategies [4, 39] are to change the configuration of the mechanism or design the damper to avoid/eliminate the specific resonant frequencies, whereas the active control method can eliminate vibration without changing the mechanism, such as feedback control, input/command shaping, and iterative learning control [37]. These active control methods have their respective advantages and disadvantages. Feedback control can eliminate most of the resonance vibrations caused by input and disturbance. However, the vibration at the beginning of the command always exists, and the bandwidth of feedback control will affect the performance of the vibration suppression. Iterative learning control (ILC) also imposes no requirements on the precise parameters of the dynamics. However, it increases the time needed to reach a response without vibration. Input shaping is a feedforward control method that has no effect on the stability of the original system and imposes no requirements on the precise parameters of the dynamics. However, there are several modes available for a physical mechanism and the input shaper used to suppress more modes leads to increased delay time and a reduction in the performance of the system.

The input shaping methods were first systematically described in the late 1950s [30]. Over the next 60 years, several variations of the input shaper are proposed for different purpose. The robust input shaper [27, 35] is robust to the errors of the modal parameters, such as the derivative method, the tolerable vibration method, the so-called extra insensitive (EI) method, and the specified insensitivity (SI) method, each with varying levels of robustness. However, the robust input shapers increase the delay time. Therefore, the learning input shaping was proposed to estimate the actual parameters, such as input shaping with golden section searches [24], input shaping with genetic algorithms [1, 22, 26], input predictive shaping [14], adaptive input shaping [9, 10], input shaping with neural networks [6], and model reference input shaping [5]. These methods are based on the sufficient data from the command and response to find optimized modal parameters or to design the controller so that the response will close to the model. However, the highly non-linear system will increase the learning complexity and precision with learning input shaping. So, the methods are not considered in this study. The complex mechanical structures usually have multimodality. The multi-mode input shaper [17] integrates the multi-mode by convolution of all the shapers designed for each of the modes. The shaped command being different from the unshaped one may cause unexpected behaviors. The contour error compensation will minimize the distortion before the command into the system [2, 13, 19]. The above methods focus on countervailing the joint vibration by the shapers. In addition, command after input shaping creates a serious problem as input delay. There are three methods designed to reduce the delay time. One is to solve the optimization problem [11, 12, 18, 23] by finding the appropriate modal parameters where the time-delay is least subject to the constraints so that the magnitude of vibration is restricted to below certain levels. The

---

This work was supported in part by the Syntec technology CO., Taiwan.

Han Pang Huang is a professor of Department of Mechanical Engineering, National Taiwan University, Taipei, Taiwan (e-mail: hanpang@ntu.edu.tw).

second method is the so-called negative input shaping method [33] where the impulses are a unit magnitude, and the positive/negative impulses are interlaced. In other words, the first impulse is positive, the second is negative, the third is positive, and so on. The two aforementioned methods cannot completely eliminate the delay time. The third method is the zero time-delay input shaping method [40, 41], which is the method to fully eliminate the delay time theoretically. In control field, input shaping can be embedded into the controller. There are two types of the control architectures. The more common one is the feedforward/feedback control structure [20, 21, 25, 32]. The feedforward control is an input shaping module, whereas the feedback control is a position controller. The other is the inverse signal shaper [16, 36]. The convolution of the actual link-side joint angle and the inversion of input shaper with distributed delay is fed back in comparison to the reference command. Although the performance of the vibration elimination caused by disturbances is better than the structure of feedforward input shaping, the inverse signal shaper cannot eliminate the delay time by means of zero time-delay input shaping.

In this study, the proposed multi-mode robust input shaping with accelerator and contour error compensation (MMR-IS-ACE) will improve the problems of time-delay and error correction. The conventional input shaping method only plans one motion state, without planning the first four derivatives of the shaped command. This is not enough for comprehensive feedback control. The proposed modified input shaping is based on the properties of convolution and is able to plan the high-order derivatives of the shaped command simultaneously, instead of through numerical differentiation, which is largely incapable of achieving high-order derivative terms.

II. MODELING AND CONTROL OF ELASTIC-JOINT DYNAMICS

A. Elastic-joint dynamics

In general, the nonlinear dynamics model of robot manipulator can be divided into two types: rigid-body dynamics and elastic-joint dynamics. The former assumes a rigid robot, and both the actuator and link are simplified for most mechanical structures under this assumption. However, elastic-joint dynamics are more consistent with the characteristics of a robot manipulator, owing to the structure of the joints. In each joint of the manipulator, the input torque is generated by a motor, and then the torque is increased by harmonic drives to the output links. In fact, the harmonic drive and torque sensor have elasticity. Thus, the elastic-joint robot dynamics can be modeled as [31]

$$\mathbf{M(q)\ddot{q} + C(q,\dot{q})\dot{q} + g(q)} = \boldsymbol{\tau}_e \tag{1}$$

$$\mathbf{B\ddot{\boldsymbol{\theta}} + G_r}\boldsymbol{\tau}_e = \boldsymbol{\tau} \tag{2}$$

where $\boldsymbol{\theta}$ and $\mathbf{q}$ represent vector of the motor-side and link-side angular displacements, respectively. In link-side dynamics (1), $\mathbf{M(q)}$ is the inertia matrix; $\mathbf{C(q,\dot{q})}$ is the centrifugal and Coriolis generalized forces; $\mathbf{g(q)}$ represents the gravitational generalized forces and $\boldsymbol{\tau}_e$ represents the elastic torque. In motor-side dynamics (2), $\mathbf{B}$ represents the inertia matrix of the motor; $\mathbf{G}_r$ represents the gear ratio and $\boldsymbol{\tau}$ represents control input. The robot arm can be formed as a two-inertia system, which connects motors and links by torsion spring. The elastic torque can be formed as the stiffness parameters $\mathbf{K}$ by the deviation between the motor-side and link-side angular displacement as

$$\boldsymbol{\tau}_\mathbf{e} = \mathbf{K(G_r}\boldsymbol{\theta}\mathbf{ - q)} \tag{3}$$

The joint elasticity is one of reasons of vibration which is characterized by the transmission of elastic torque between two dynamics model. Then the inverse dynamics of the elastic-joint robot manipulator can be derived as

$$\begin{aligned}\boldsymbol{\tau} = \mathbf{BG_r^{-1}\{K^{-1}[M(q)q^{(4)} + 2\dot{M}(q)\dddot{q}}\\ \mathbf{+\ddot{M}(q)\ddot{q} + \ddot{n}(q,\dot{q})] + \ddot{q}\} + G_r[M(q)\ddot{q} + n(q,\dot{q})]}\end{aligned} \tag{4}$$

where $\mathbf{n}$ represents the combination of $\mathbf{C(q,\dot{q})}$ and $\mathbf{g(q)}$; $\mathbf{q^{(4)}}$ represents the four time differential of $\mathbf{q}$.

The elastic-joint dynamics characterize the joint elasticity and results in vibration. The proposed vibration suppression method will use the dynamics for modal parameter estimation and use the feedforward controller to eliminate the system vibration. The following will introduce the control and estimation methods.

B. Feedback/Feedforward control

The control architecture for the manipulator with elastic-joint dynamics consists of the feedforward and the feedback control as

$$\boldsymbol{\tau} = \mathbf{u_{FF} + u_{FB}} \tag{5}$$

The feedforward control is used to compensate for nonlinear dynamics and adds the proposed input shaper for vibration suppression, which can be derived as

$$\begin{aligned}\mathbf{u_{FF}} = \mathbf{BG_r^{-1}\{K^{-1}[M(q_d)q_d^{(4)} + 2\dot{M}(q_d)\dddot{q}_d + \ddot{M}(q_d)\ddot{q}_d}\\ \mathbf{+\ddot{n}(q_d,\dot{q}_d)] + \ddot{q}_d\} + G_r[M(q_d)\ddot{q}_d + n(q_d,\dot{q}_d)]}\end{aligned} \tag{6}$$

On the other hand, the conventional PD feedback control is a high-gain controller based on the rigid-body dynamics which does not consider the joint elasticity. However, the PD feedback control ensure the system stability and the tracking performance, which can be derived as

$$\mathbf{u_{FB}} = \mathbf{K_p(q_d - G_r}\boldsymbol{\theta}) + \mathbf{K_v(\dot{q}_d - G_r}\dot{\boldsymbol{\theta}}) \tag{7}$$

where $\mathbf{K_p}$ and $\mathbf{K_v}$ represent the gain of angular displacement and angular velocity error; subscript **d** represents the desired trajectory.

C. Modal analysis for robot manipulator

The conventional model-based PD control will generate the vibration due to the joint elasticity. The modal analysis method, "PloyMAX" [3] is a curve fitting method in frequency domain used to model the vibration for the frequency response functions of the output signals. Then the modal parameters can be calculated by the eigenvalue of the system after the modeling procedure. The polynomial form is described as

$$H(\omega) = B(\omega)A(\omega)^{-1} \tag{8}$$

where $H(\omega)\in\mathbb{C}$ is the frequency response function (FRF). $B(\omega)\in\mathbb{C}$ is the numerator polynomial and $A(\omega)\in\mathbb{C}$ is the denominator polynomial. The numerator polynomial and denominator polynomial are defined as

$$B(\omega)=\sum_{r=0}^{p}\Omega_r(\omega)\beta_r$$
$$A(\omega)=\sum_{r=0}^{p}\Omega_r(\omega)\alpha_r \tag{9}$$

where $\Omega_r(\omega)$ is the polynomial basis; p is the polynomial order; β_r and α_r are polynomial coefficients. Because the frequency-domain model is derived from a discrete-time model, its polynomial bases, $\Omega_r(\omega)$ are

$$\Omega_r(\omega)=e^{j\omega\Delta t} \tag{10}$$

where Δt is the sampling time. If the frequencies locate between f_0 and f_{end}, then the unknown parameters are

$$\omega=2\pi(f-f_0)$$
$$\Delta t=\frac{1}{2(f_{end}-f_0)} \tag{11}$$

The polynomial coefficients of the right matrix-fraction model are assumed to be real values. Furthermore, the FRF model can be rewritten as the function dependent on coefficients, $H(\omega_k,\theta)$.

$$\boldsymbol{\beta}=\begin{bmatrix}\beta_0\\ \beta_1\\ \cdots\\ \beta_p\end{bmatrix}\in\mathbb{R}^{(p+1)\times 1},\ \boldsymbol{\alpha}=\begin{bmatrix}\alpha_0\\ \alpha_1\\ \cdots\\ \alpha_p\end{bmatrix}\in\mathbb{R}^{(p+1)\times 1}$$
$$\boldsymbol{\theta}=\begin{bmatrix}\beta\\ \alpha\end{bmatrix}\in\mathbb{R}^{2(p+1)\times 1} \tag{12}$$

The least-squares method is applied to estimate the unknown model coefficients $\boldsymbol{\theta}$ so that the sum of errors, $\varepsilon(\omega_k,\boldsymbol{\theta})$, between the FRF measured data and the model is minimum. $\widehat{H}(\omega_k)$ represents the FRF measured data, where $\omega_k\,(k=1,2,\ldots,N_f)$ are the discrete frequencies of FRF measurements.

$$\begin{aligned}\varepsilon(\omega_k,\theta)&=\left(H(\omega_k,\boldsymbol{\theta})-\widehat{H}(\omega_k)\right)\\ &=\left(B(\omega_k,\boldsymbol{\beta})A^{-1}(\omega_k,\boldsymbol{\alpha})-\widehat{H}(\omega_k)\right)\end{aligned} \tag{13}$$

Now, the companion matrix can be constructed as

$$\mathbf{A_c}=\begin{bmatrix}\alpha_{p-1} & \alpha_{p-2} & \cdots & \alpha_1 & \alpha_0\\ 1 & 0 & \cdots & 0 & 0\\ 0 & 1 & \cdots & 0 & 0\\ \vdots & \vdots & \ddots & \vdots & \vdots\\ 0 & 0 & \cdots & 1 & 0\end{bmatrix} \tag{14}$$

This matrix is used to calculate the poles (eigenvalues) and modal participation factors (eigenvectors) as

$$\left(\mathbf{A_c}-\lambda_n\mathbf{I}_{p\times p}\right)\mathbf{V}_n=0 \tag{15}$$

The poles are related to the natural frequencies ω_n and relevant damping ratio ζ_n. The eigenvectors $\mathbf{V}_n$ are related to the modal participation factor.

$$\lambda_n,\lambda_n^*=-\zeta_n\omega_n\pm i\omega_n\sqrt{1-\zeta^2} \tag{16}$$

The polyreference least-squares complex frequency domain method (PolyMAX) estimates the modal parameters of the vibration in the output signals, which are the necessary parameters for the input shaping approach.

III. INPUT SHAPING ALGORITHM

The conventional input shaping suppress the vibration caused by the input. The desired command is shaped to eliminate the system vibration. However, the conventional method yields the input delay as well as the contour error. It is desired to reduce the time delay and contour error.

A. *Conventional input shaping*

The conventional input shaper is designed to modify the command, as shown in Fig. 1, so that the response of the unexpected vibration will be suppressed [28, 29].

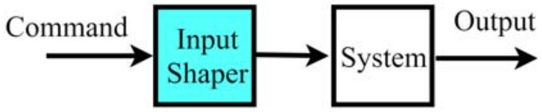

Fig. 1. Input shaping architecture.

Assuming the system between the command and the response of unexpected vibration is a second-order linear and time-invariant system as:

$$\frac{Y(s)}{U(s)}=\frac{\omega_n^2}{s^2+2\zeta\omega_n s+\omega_n^2} \tag{17}$$

and impulse response as:

$$y(t)=\left[A\frac{\omega_n}{\sqrt{1-\zeta^2}}e^{-\zeta\omega_n(\mathrm{t}-\mathrm{t}_1)}\right]\sin(\omega_n\sqrt{1-\zeta^2}\,(\mathrm{t}-\mathrm{t}_1)) \tag{18}$$

where A is the amplitude of impulse (input), ω_n is the natural frequency of the system, ζ is the damping ratio of the system and t_1 is the time of impulse input. The principle of the input shaping is to generate another pulse at t_2 to cancel out the vibration. The Fig. 2-(a) shows the example of two impulse responses. For N inputs, these impulse responses can be synthesized from (18) as

$$y(t)=y_1(t)+y_2(t)+\cdots+y_N(t) \tag{19}$$

where $y_1,\ldots y_N$ are the sub-impulse response of the N inputs. These impulses can be derived as

$$y_i(\mathrm{t})=B_i\sin(\alpha t+\phi_i)=A_{amp}\sin(\alpha t+\psi)\ ,\ i\in 1,\ldots,N \tag{20}$$

where

$$B_i=A_i\frac{\omega_n}{\sqrt{1-\zeta^2}}e^{-\zeta\omega_n(t-t_i)}$$
$$\phi_i=\omega_n\sqrt{1-\zeta^2}\,t_i \tag{21}$$

$$A_{amp}=\sqrt{(\sum_{i=1}^{N}B_i\cos\phi_i)^2+(\sum_{i=1}^{N}B_i\sin\phi_i)^2};$$
$$\psi=\tan^{-1}(\sum_{i=1}^{N}B_i\cos\phi_i\Big/\sum_{i=1}^{N}B_i\sin\phi_i)\tag{22}$$

In order to suppress the vibration caused by the first impulse, A_{amp} must be equal to zero as the two terms of (22) after t_N must be equal to zero. The constraints can be formulated as

$$\sum_{i=1}^{N}A_ie^{-\zeta\omega_n(t_N-t_i)}\cos(\omega_n\sqrt{1-\zeta^2}t_i)=0$$
$$\sum_{i=1}^{N}A_ie^{-\zeta\omega_n(t_N-t_i)}\sin(\omega_n\sqrt{1-\zeta^2}t_i)=0\tag{23}$$

Subsequently, the third constraint is $t_1=0$ and the fourth is $\sum_{j=1}^{N}A_j=1$. These four constraints are used to solve at least two impulses. This is called zero-vibration method (ZV) and the two-impulse shaper is time-optimal, as shown in Fig. 2-(b).

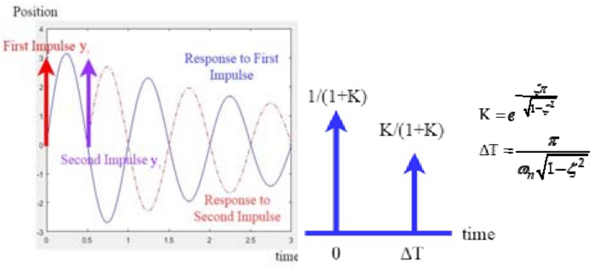

(a) (b)

Fig. 2. (a) Two-impulse response. (b) Two-impulse input shaper

B. *Proposed Multi-mode Robust Input Shaping* (*MMR-IS*)

The conventional input shaping utilize the additional impulse input to eliminate the vibration which is generated by the system. However, the input shaper will cause the input delay and the contour error. In order to improve the conventional method, the proposed multi-mode robust input shaping contains three parts for robustness of the input shaping, as shown in Fig. 3. The proposed method contains three parts:

- Accelerator
- Multi-mode robust input shaper
- Contour error compensation

First, the proposed accelerator is based on the zero time-delay input shaping, which is first proposed in [40] by means of accelerating input. However, the conventional accelerator may exceed the joint torque limit.

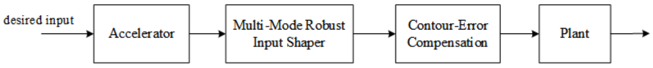

Fig. 3. Proposed multi-mode robust input shaping architecture

In addition, the time scale in this method may be negative when the natural frequencies are low. To mitigate these two problems, the modified zero time-delay input shaping is proposed [41]. However, the zero time-delay input shaping has two severe problems. One is a compensator calculated by the impulse response of the system adds oscillation to the command, which will excite unexpected vibration. The other problem exists in both zero time-delay input shaping methods. Although these methods can fully eliminate the delay time, the shaped commands always result in unexpected and larger vibration than the response of the unshaped command. To solve these problems, the modified accelerator adds an adjustable parameter f_α and the time scale α . The modified accelerator can be derived as

$$\alpha=\frac{T}{T+f_\alpha\times t_n}\tag{24}$$

where T is the time instant of the last impulse in the time sequence; t_n is the time-delay of the shaper and f_α is defined as a non-negative value so that the compensation to the delay time is adjustable. There are three advantages with a flexible time scale. First, the time scale can be adjusted to avoid exceeding the joint torque limit. Second, the time scale must be positive even if the natural frequency is low. Last but not the least, it can prevent the response from exciting unexpected vibration by adjusting f_α. However, it remains delay time. The accelerated desired joint angle as:

$$\mathbf{q}_\mathbf{d}^{\mathbf{acc}}(t)=\mathbf{q}_\mathbf{d}\left(\frac{t}{\alpha}\right)\qquad\forall t\in[0,\alpha T]\tag{25}$$

Second, the multi-mode robust input shaping is the main part to suppress the vibrations. Even though the conventional input shaper composed of more than two impulses will increase the delay time, the vibrations with high frequencies will not be excited due to the asymmetry in the sensitivity curves of this shaper. There are maximum number of the impulses in the shapers designed by full-order modified input shaping. The magnitude in the frequency response of the full-order modified input shaping with zero-vibration (FMIS-ZV) input shaper [34] is much lower than the zero-vibration input shaper in high frequency region. The FMIS-ZV input shaper is given as

$$\begin{bmatrix}A_i\\t_i\end{bmatrix}=\begin{bmatrix}\frac{1}{1+M}&\frac{K}{1+M}&\cdots&\frac{K^{N-1}}{1+M}\\0&\frac{2\Delta T}{N}&\cdots&(N-1)\frac{2\Delta T}{N}\end{bmatrix}\tag{26}$$

$$K=e^{\frac{-2\zeta\pi}{N\sqrt{1-\zeta^2}}}\tag{27}$$
$$M=K+K^2+\cdots+K^{N-1}$$

where N is the maximum integer less than $2\Delta T$/*sampling period*. It is difficult to directly solve all constraints for multi-mode zero-vibration methods, even though the shaper is time optimal. A convenient way [17] is to convolute a single-mode input shaper, which is used to suppress the first resonance mode, using the original command in the first step. The last step is convoluted with a single-mode input shaper, which is then used to suppress the second resonance mode. Repeat the second step until all resonance modes are considered. The shaped command can be used to eliminate the multi-mode residual vibration. In order to make the input shaper be robust to the error of natural frequency and damping ratio. The derivative method [27, 35] is applied to design the robust input shaper. The derivative order of the constraints is defined as the robustness type R_T. If robustness type is 1, the first order derivative of the constraints can be calculated as the additional constraints as

$$\sum_{i=1}^{N} A_i t_i e^{-\zeta\omega_n(t_N-t_i)}\sin(\omega_n\sqrt{1-\zeta^2}t_i)=0$$
$$\sum_{i=1}^{N} A_i t_i e^{-\zeta\omega_n(t_N-t_i)}\cos(\omega_n\sqrt{1-\zeta^2}t_i)=0 \tag{28}$$

If R_T =1, the three impulses can be solved at least by these six constraints shown in Fig. 4.

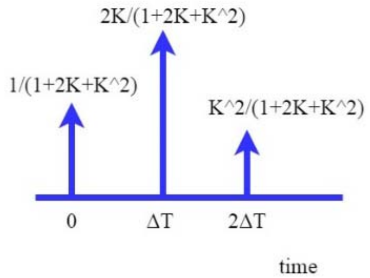

Fig. 4. Three-impulse input shaper with R_T=1.

If R_T =0, the two impulses can be solved at least by four constraints. It is worth to mentioning that the three-impulse shaper equals to the convolution of the two-impulse shaper with itself. It can be extended to design robust FMIS. The number of robustness type is also equal to the times of convoluting the command with the FMIS-ZV input shaper. This method can improve the robustness to the errors of natural frequency and damping ratio. The multi-mode robust input shaping algorithm is shown in Table 1.

TABLE I. MULTI-MODE ROBUST INPUT SHAPING ALGORITHM

Multi-mode robustness input shaping algorithm

```
1. Given a desired command
2. for each mode i = 1, 2,…, m
3.    Initialize the input shaper K[i], M[i], N[i] (25)
4.    for j = 0, 1,.., R_T (robustness type)
5.       The command is convolution R_T times
            Command = Command * input shaper[i]
6.    end
7. end
8. The multi-mode shaped command is convolution R_T ×m
      times
```

Third, the contour error compensation [2, 7, 8, 15, 19] is used to eliminate distortion and the delay time in the Cartesian space. The aforementioned input shaping is used in the joint space so that the shaped commands are always different from the unshaped ones. But it may cause unexpected behaviors. Moreover, the proposed multi-mode robust input shaping with accelerator may remain delay time. In order to improve these problems, the contour-error compensation is applied. The contour error of the end-effector is as

$$\mathbf{X_c}=\mathbf{X}+\boldsymbol{\varepsilon} \tag{29}$$

where $\mathbf{X}$ is the vector of position and orientation by forward kinematics of the shaped commands in joint space; $\boldsymbol{\varepsilon}$ is the contour-error term calculated by the method proposed in [13]. Subsequently, the shaped-compensated command $\mathbf{q}_{sc}$ in joint space can be obtained by inverse kinematics. Considering the transformation of the contouring error between the Cartesian space and joint space, it must be checked whether the Jacobian matrix is near the singularity and whether the compensation in joint space is available. The modification of singularity avoidance is employed at the current position, and then the modified contour error for each joint is derived as

$$\begin{cases}\delta q_c=\left(\omega^*\cdot\mu/M_s\right)\cdot f_{CE}\cdot(q_{sc}-q_s)\ , \ if\ \ \omega^*<M_s\\ \delta q_c=f_{CE}\cdot(q_{sc}-q_s)\qquad\qquad ,\quad \text{otherwise}\end{cases} \tag{30}$$

and

$$\omega^*=\sqrt{\det\left(\mathbf{J}(\boldsymbol{\theta})\mathbf{J}^{\mathbf{T}}(\boldsymbol{\theta})\right)} \tag{31}$$

where $\mathbf{J}(\mathbf{q})$ is the Jacobian matrix; μ is a positive constant; M_S is a threshold value vicinity of the singular point; f_{CE} is a compensation gain; q_{sc} is the shaped and compensated command from (29) and q_s is the shaped command. In order to avoid exciting unexpected vibration, the compensation term must be multiplied by a non-negative and adjustable value f_{CE} since over compensation will excite the unexpected vibration in the application.

IV. PROPOSED VIBRATION SUPPRESSION ARCHITECTURE

Input shaping is a method to transform the desired trajectory to feedforward controller to eliminate the vibration, which has no effect on the stability of the original system and no requirement from the precise dynamics parameters. However, input shaping cannot guarantee the tracking performance. Therefore, the PD feedback control is used to ensure the stability of the tracking performance. The conventional PD feedback control has high tracking performance, but the resonance vibration on the link side still exist.

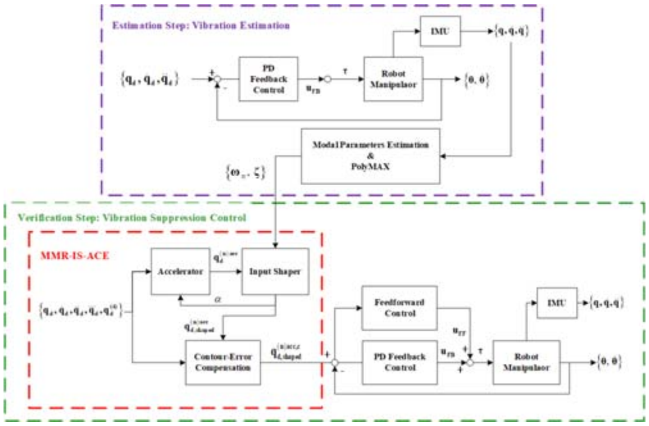

Fig. 5. Control block diagram for vibration suppression.

To improve the performance of a single control strategy, the vibration suppression architecture is proposed, as shown in Fig.5. The input shaping approach in joint space is used in feedforward control. The conventional PD controller is used in feedback control. However, not only the desired joint angles but also the first four derivatives of the desired joint angle are necessary to feedback control, and the conventional input shaping only generates the shaped joint angle. A method is proposed to calculate the first four derivatives of the shaped command simultaneously with the shaped command. This is based on the concept that the convolution of unshaped commands with input shapers can be reduced to shifting and scaling in time domain. In other words, if the 0th to 4th order derivatives of the desired joint angle are planned by the 9th order polynomial functions in advance, then these high order terms can be calculated as:

$$\mathbf{q}_{\mathbf{d,shaped}}^{\mathbf{acc}}(t)=\mathbf{q}_{\mathbf{d}}\left(\frac{t}{\alpha}\right)*(\text{input shaper})$$

1-order derivative:

$$\dot{\mathbf{q}}_{\mathbf{d,shaped}}^{\mathbf{acc}}(t)=\frac{1}{\alpha}\dot{\mathbf{q}}_{\mathbf{d}}\left(\frac{t}{\alpha}\right)*(\text{input shaper})$$

2-order derivative:

$$\ddot{\mathbf{q}}_{\mathbf{d,shaped}}^{\mathbf{acc}}(t)=\left(\frac{1}{\alpha}\right)^{2}\cdot\ddot{\mathbf{q}}_{\mathbf{d}}\left(\frac{t}{\alpha}\right)*(\text{input shaper}) \qquad (32)$$

3-order derivative:

$$\dddot{\mathbf{q}}_{\mathbf{d,shaped}}^{\mathbf{acc}}(t)=\left(\frac{1}{\alpha}\right)^{3}\cdot\dddot{\mathbf{q}}_{\mathbf{d}}\left(\frac{t}{\alpha}\right)*(\text{input shaper})$$

4-order derivative:

$$\mathbf{q}_{\mathbf{d,shaped}}^{(4)\,\mathbf{acc}}(t)=\left(\frac{1}{\alpha}\right)^{4}\cdot\mathbf{q}_{\mathbf{d}}^{(4)}\left(\frac{t}{\alpha}\right)*(\text{input shaper})$$

where $\forall t\in[t,\alpha T]$. Moreover, the 9th order polynomial functions are used to fit the contour-error compensation terms in (30). The first four derivatives of the contour-error compensation terms can be derived as

$$\begin{aligned}
\mathbf{q}_{\mathbf{d,shaped}}^{\mathbf{acc,c}}(t)&=\mathbf{q}_{\mathbf{d,shaped}}^{\mathbf{acc}}(t)+\boldsymbol{\delta}\mathbf{q}_{\mathbf{c}}\\
\dot{\mathbf{q}}_{\mathbf{d,shaped}}^{\mathbf{acc,c}}(t)&=\dot{\mathbf{q}}_{\mathbf{d,shaped}}^{\mathbf{acc}}(t)+\boldsymbol{\delta}\dot{\mathbf{q}}_{\mathbf{c}}\\
\ddot{\mathbf{q}}_{\mathbf{d,shaped}}^{\mathbf{acc,c}}(t)&=\ddot{\mathbf{q}}_{\mathbf{d,shaped}}^{\mathbf{acc}}(t)+\boldsymbol{\delta}\ddot{\mathbf{q}}_{\mathbf{c}} \qquad (33)\\
\dddot{\mathbf{q}}_{\mathbf{d,shaped}}^{\mathbf{acc,c}}(t)&=\dddot{\mathbf{q}}_{\mathbf{d,shaped}}^{\mathbf{acc}}(t)+\boldsymbol{\delta}\dddot{\mathbf{q}}_{\mathbf{c}}\\
\mathbf{q}_{\mathbf{d,shaped}}^{(4)\,\mathbf{acc,c}}(t)&=\mathbf{q}_{\mathbf{d,shaped}}^{\mathbf{(4)acc}}(t)+\boldsymbol{\delta}\mathbf{q}_{\mathbf{c}}^{(4)}
\end{aligned}$$

The desired trajectories are modified, which includes the accelerator, input shaper and contour error compensation. These modified trajectories (33) are substituted into (6) to eliminate the system vibration.

The procedures of simulations and experiments are divided into two steps: the estimation step and the verification step. The former is to estimate the vibration of the system to obtain the natural frequency and damping ratio. The latter is to verify the performance of the vibration suppression architecture. The vibration suppression architecture is shown in Fig. 5.

- **Estimation step:** Given a desired trajectories, the PD feedback control is based on the rigid-body dynamics which generate the vibration during the motion. The joint vibration can be attributed to the model-based PD control which only considers the motor-side tracking performance. During the motion, the link-side vibration can be measured by inertia measurement unit (IMU). Subsequently, the natural frequency and damping ratio of vibrations will be estimated by means of PolyMAX. Finally, the parameters are used to generate the shaping commands.
- **Verification step:** Given a desired trajectories, the commands are accelerated by (25). The accelerated commands are shaped by multi-mode robust input shaping (26) and (28), then the end-effector contour error is compensated by (29) and (30), and the desired trajectories are modified. The above process is the proposed input shaping – MMR-IS-ACE, as shown in red frame of Fig. 5. These commands are obtained by (32) and (33) to feedforward/feedback controller which is based on the elastic-joint dynamics. The vibrations in the estimation step are expected to be suppressed.

V. SIMULATIONS

A 6-DOF robot manipulator is used to simulate the proposed vibration suppression method. The 6-DOF robot manipulator was developed in our laboratory. The joints use DC motors and feedback angular displacement, velocity, and torque from the controller. The transmission between input-output uses a pulley or spur gear series harmonic drive to amplify the link-side torque from the motor torque. The 6-DOF robot manipulator is designed by Solidworks, and the material characteristics are used to analyze all the parameters, as shown in Table 2. The model for simulations are based on elastic-joint dynamics. Moreover, the desired trajectories for six axes are planned by the 9th order polynomial functions. In the simulations, we only consider the input shaping of the first three joints. The simulations results between unshaped and shaped commands/responses will be discussed in the following.

TABLE II. 6-DOF ROBOT MANIPULATOR MODEL PARAMETERS. THE PARAMETERS REPRESENT D-H(Θ, D, A,A), LINK-SIDE DYNAMICS(MASS-M, CENTER OF MASS-CX,Y,Z, INERTIA-IXX,YY,ZZ), MOTOR-SIDE DYNAMICS (MOTOR INERTIA-B) AND JOINT STIFFNESS K

Joints Parameters (units)	**1**	**2**	**3**	**4**	**5**	**6**
θ (*rad*)	θ_1	$\theta_2+\pi$	θ_3	$\theta_4+\pi/2$	θ_5	$\theta_6+\pi/2$
d (*m*)	1.22	0	0.371	0	0.28	0
a (*m*)	0	0	0.01	-0.01	0	0.12982
α (*rad*)	90	90	90	-90	90	90
m (*kg*)	1.529	0.344	2.034	0.236	1.246	0.274
C_x (*m*)	-0.0036	0.0005	-0.0072	0.0031	-0.0023	0.0002
C_y (*m*)	-0.0342	0.0068	-0.1382	-0.0003	-0.1303	0.0371
C_z (*m*)	-0.012	0.02	0.0024	0.0347	0.0004	-0.0012
I_{xx} ($kg\ m^2$)	0.0035	0.0002	0.0328	0.0003	0.0073	0.0001
I_{yy} ($kg\ m^2$)	0.0022	0.0002	0.0152	0.0002	0.0008	0.0001
I_{zz}($kg\ m^2$)	0.0025	0.0003	0.0327	0.0002	0.0074	0.0001
B ($g\ m^2$)	0.0012	0.0012	0.001	0.001	0.001	0.0038
K(*Nm/rad*)	1000	1000	1000	1000	1000	1000
Gr	0.005	0.004	0.005	0.004	0.005	0.0033

A. *Multi-mode robust input shaping (MMR-IS)*

In this section, the simulations between unshaped commands/responses and shaped commands/responses based on multi-mode robust input shaping (MMR-IS) are discussed. In the MMR-IS simulations, the aim is to simulate the vibration suppression performance of the MMR-IS, comparing with the unshaped method. The unshaped results are based on the conventional PD feedback control. In addition, the MMR-IS only shape the commands rather than accelerating it. The parameters of MMR-IS are shown in Table 3 and the results are shown in Fig. 6. The results show that the motor-side PD feedback control has a great tracking performance as well. But the link-side has the vibrations due to the joint elasticity, as shown in Fig. 6. The simulation results show that the maximum delay time is 2.4 seconds with MMR-IS. The vibrations are obviously reduced to ± 0.01 rad.

TABLE III. THE PARAMETERS OF MULTI-MODE ROBUST INPUT SHAPING

Joint	1	2	3
ω_n (Hz)	1.806	1.676	1.672
ζ	0.385	0.107	0.078
R_T	3	1	0
Delay Time (s)	2.4	1.19	0.6

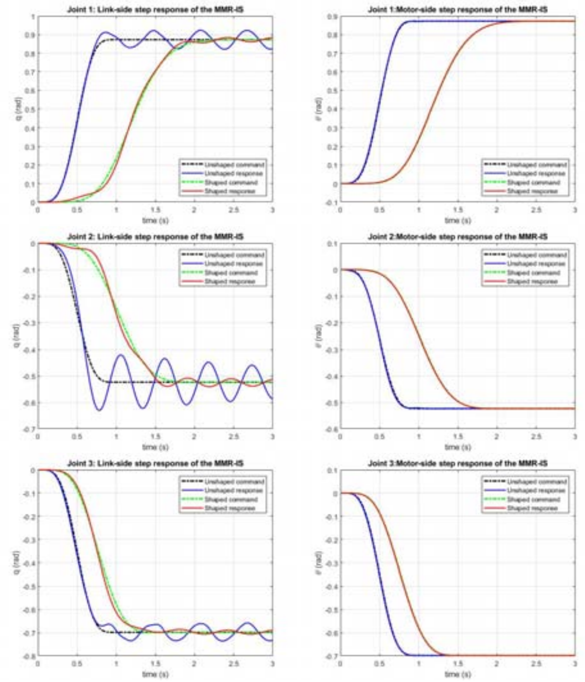

Fig. 6. Comparison between unshaped and MMR-IS step responses. Upper-left to lower-left represent the q_1 to q_3 and Upper-right to lower-right represent the θ_1 to θ_3. black-unshaped command, blue-unshaped response, green- shaped command and red-shaped response.

The Fig. 7 shows the spectrum of the link-side angular acceleration. The blue lines represent the spectra of the link-side angular acceleration and the red lines represent the spectra of the link-side angular acceleration with MMR-IS. The simulation results show that the magnitudes of the natural frequencies listed in Table 3 are significantly suppressed by the proposed input shaping. Above joint space simulation results are projected by forward kinematics to the end-effector to compare the results in Cartesian space, and the translation and orientation are shown in Fig. 8.

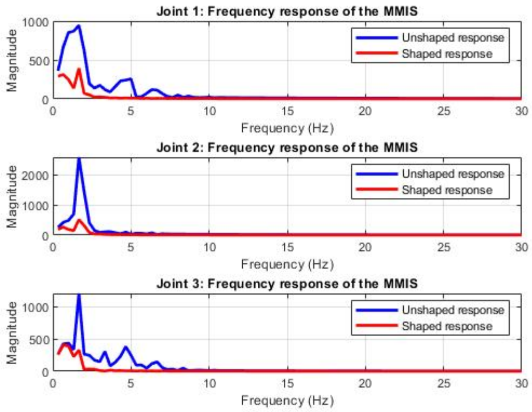

Fig. 7. Frequency response of the link-side angular acceleration. (blue-unshaped response and red-shaped response)

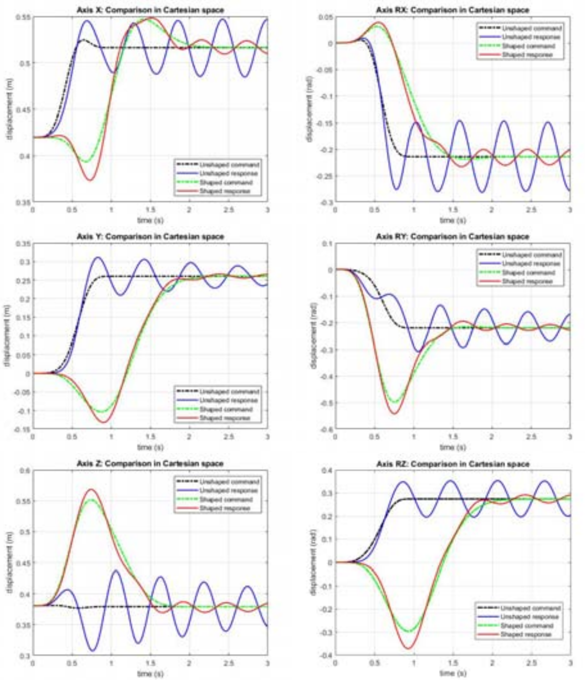

Fig. 8. End-effector comparison between unshaped responses and shaped responses. Upper-left to lower-left are x, y and z. Upper-right to lower-right are orientations x, y and z. black-unshaped command, blue-Unshaped response, green- Shaped command and red-shaped response.

The simulations results show that the vibration of the end-effector also has significant suppression, the minimum amplitude of vibration in the direction y is within ± 0.005 m and orientation y is within ± 0.01 rad. The simulation results show the MMR-IS can suppress the vibration significantly. However, there are two problems with the proposed shaper. One is the delay time, which reduces the tracking performance. The other problem is the serious contour error in the end-effector, as shown in Fig. 8. The shaped position commands in end-effector are distorted. Therefore, the proposed vibration suppression method has added the accelerator and contour-error compensation to improve the robustness of the MMR-IS. The following will show the simulations.

B. Multi-mode robust input shaping with accelerator and contour error compensation (MMR-IS-ACE)

Because of the problems of the MMR-IS, in this section, the comparisons between unshaped commands/responses and shaped commands/responses based on MMR-IS with accelerator and contour-error compensation (MMR-IS-ACE) are discussed. The parameters are listed in TABLE . The maximum delay time is 0.7 seconds, which is better than the maximum delay time of the NTD-IS (2.4s). The delay time is reduced at least 33.3 (%).

TABLE IV. THE PARAMETERS OF MMR-IS-ACE

Joint	1	2	3
ω_n (Hz)	1.806	1.676	1.672
ζ	0.385	0.107	0.078
R_T	3	1	0
f_α	2	5	1
f_{CE}	0.3	0.3	0.3
Delay Time (s)	0.7	0.2	0.4

The vibrations in the link-side responses can be obviously suppressed within ±0.01 rad and the delay time is also reduced without exciting unexpected vibrations, as shown in Fig. 9. Specially, the q_1 to q_3 have better tracking performance than MMR-IS. Unfortunately, the delay time cannot be fully eliminated since the larger f_α and f_{CE} excite unexpected vibrations.

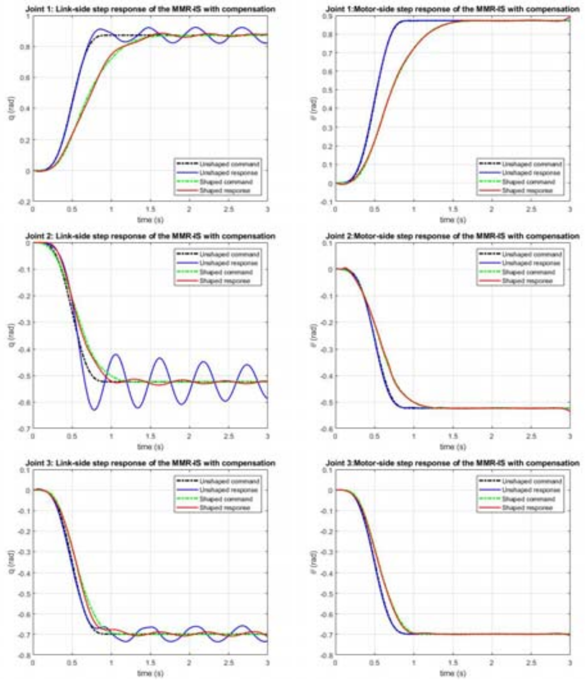

Fig. 9. Comparison between unshaped and MMR-IS-ACE step responses. Upper-left to lower-left represent the response of q_1 to q_3 and upper-right to lower-right represent the response of θ_1 to θ_3. black-unshaped command, blue-unshaped response, green- shaped command and red-shaped response.

The spectrums of the link-side angular acceleration show the magnitude of the natural frequencies are reduced compared to unshaped commands and the results are also better than MMR-IS, as shown in Fig. 10.

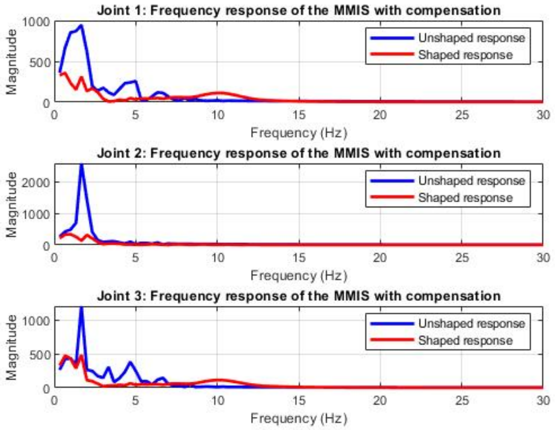

Fig. 10. Frequency response of the link-side angular acceleration with MMR-IS-ACE. (blue-unshaped response and red-shaped response)

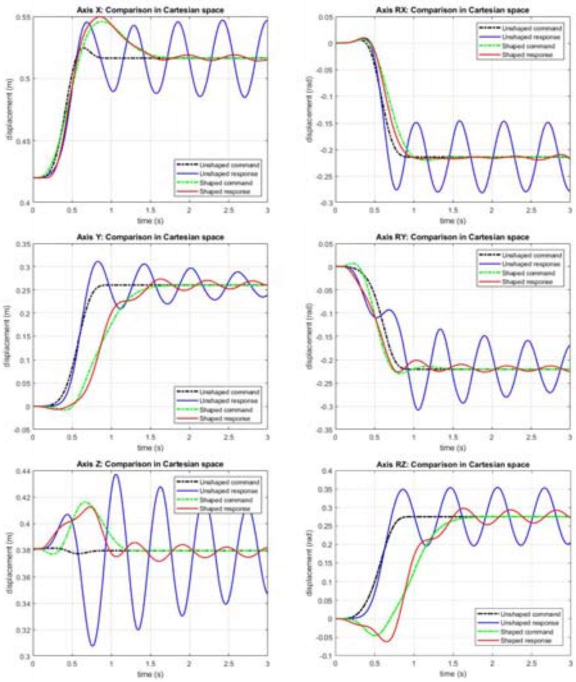

Fig. 11. End-effector comparison between unshaped responses and shaped responses. black-unshaped command, blue-unshaped response, green- shaped command and red-shaped response.

VI. VIBRATION SUPPRESSION CONTROL EXPERIMENTS

The simulations show that the MMR-IS-ACE can not only suppress the vibrations but also eliminate the delay time and contour error. In order to verify the performance of the architecture proposed in this study. In the experiments, the end-effector of the manipulator is equipped with a cup of water, as shown in Fig. 12.

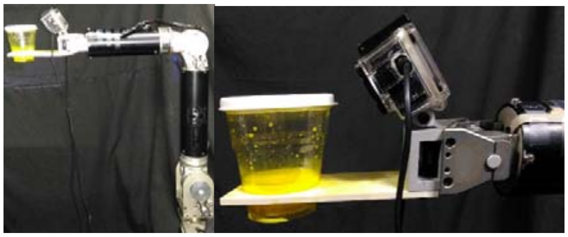

Fig. 12 The scenario of the vibration suppression experiments

The cup with water is expected to be stable under a fast motion. The end-effector is also equipped with an inertia measurement unit (IMU) to measure the motion states, containing the vibration signals. Subsequently, the shaped commands of each joint can be obtained by the test of single axis. The shaped command of the joints will be able to suppress the vibrations caused by the relevant axes. From the experimental results, the multi-axis shaped commands, which are combined with the shaped commands of each axis, also have high performance of vibration suppression.

A. Modal analysis and testing for each joints

The experiments are aimed to analyze the natural frequency and damping ratio of each joint one by one. Then each joint will be tested separately for tuning the optimal input shaping parameters. First, the desired trajectories are given for six joints which planned by the 9th order polynomial functions, called unshaped commands. In the estimation step, the manipulator will follow the desired trajectory by conventional PD feedback control then measure the link-side states by IMU. The input-output data can be used to calculate the natural frequency and damping ratio. In the estimation experiments, the joint 3rd to 5th have no obvious residual vibrations in the link-side responses. Therefore, the input shaping is applied to eliminate the resonance vibrations only for the 1st to 3rd joints. The parameters and experimental results are listed in Table 5.

The results show that the delay time of the proposed method are reduced at least 75.8 (%) compared to MMR-IS. The unshaped and the shaped commands for the first three joints are shown in Fig. 13. The link-side accelerations are measured by IMU, the vibrations have been significantly suppressed compared to the unshaped results, as shown in Fig. 14.

TABLE V. THE PARAMETERS OF MMS-IS-ACE

Joint	1		2		3	
$\omega_n\ (Hz) \begin{bmatrix} \text{mode 1} \\ \text{mode 2} \\ \vdots \end{bmatrix}$	$\begin{bmatrix} 11.3528 \\ 13.0124 \end{bmatrix}$		$\begin{bmatrix} 16.3459 \\ 20.0127 \\ 13.0155 \end{bmatrix}$		$\begin{bmatrix} 8.3456 \\ 6.6800 \end{bmatrix}$	
$\zeta \begin{bmatrix} \text{mode 1} \\ \text{mode 2} \\ \vdots \end{bmatrix}$	$\begin{bmatrix} 0.0586 \\ 0.0436 \end{bmatrix}$		$\begin{bmatrix} 0.0392 \\ 0.0356 \\ 0.0488 \end{bmatrix}$		$\begin{bmatrix} 0.0542 \\ 0.0633 \end{bmatrix}$	
Robustness Type	6		6		3	
f_α	0.7		1		0.7	
f_{CE}	0.7		0.7		0.7	
Delay time (s) MMR-IS | MMR-IS-ACE	1.1	0.27	1.3	0.31	1.04	0.05

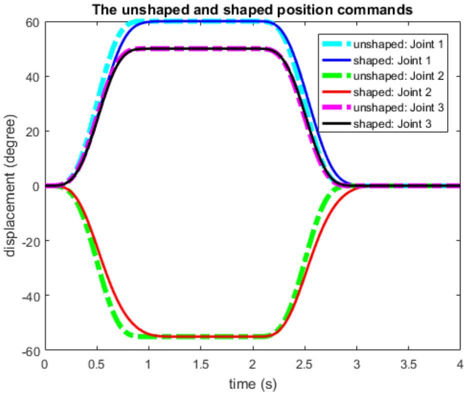

Fig. 13. The unshaped and shaped commands for 1st to 3rd joints.

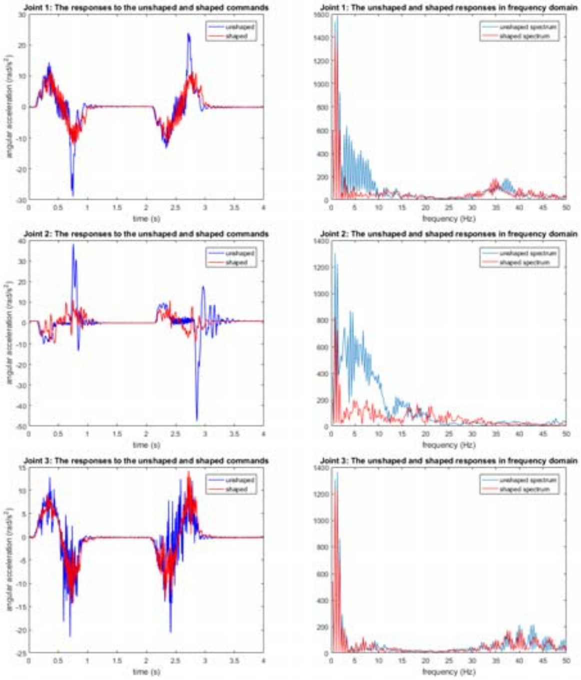

Fig. 14. The link-side joint 1 to joint 3 acceleration responses to the unshaped and shaped commands in time (left) /frequency domain (right). blue-unshaped, red-shaped.

The jerks of the unshaped results are successfully suppressed about 50% by MMR-IS-ACE. In frequency domain, the magnitudes in the range of natural frequency are reduced in the spectra of link-side angular acceleration for the first three joints. The tracking performance of the motor-side states are also verified, as shown in Fig. 15. The experiments of the proposed vibration suppression architecture guarantees both the motor-side tracking performance and the feasibility of MMR-IS-ACE to suppress the vibrations in each joint. These parameters can be used to do the multi-axis experiments.

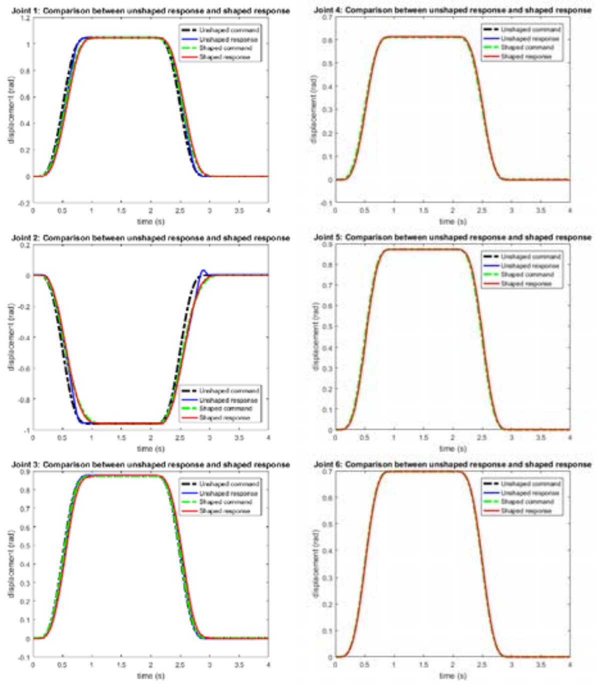

Fig. 15. Comparison between unshaped and shaped responses in the motor-side θ. Upper-left to lower-left are joint 1 to joint 3. Upper-right to lower-right are joint 4 to joint 6, respectively.

B. *Vibration Suppression for Multi-Axis Manipulator*

The above results have verified the vibration suppression architecture both in the motor-side and the link-side. In the multi-axis experiments, only the end-effector tracking performance are considered. The multi-axis shaped commands are composed of the six single-axis shaped commands. The vibration suppression parameters of the multi-axis manipulator utilize Table 5 which are verified in single joint experiments. The delay time is reduced at least 75.8 (%).The unshaped and the shaped commands for the end-effector are shown in Fig. 16. The commands of MMR-IS-ACE are similar to unshaped commands. The end-effector jerks are suppressed in x, y, z and ry, especially in x direction, as shown in Fig. 17. The orientation of x and z directions also suppress part of vibrations, but the difference between the shaped and unshaped can be attributed to the difference of the input commands. In the multi-axis vibration suppression experiments, the water in the cup can be stably move back and forth and the vibrations, delay time are obviously eliminated by the proposed vibration suppression architecture.

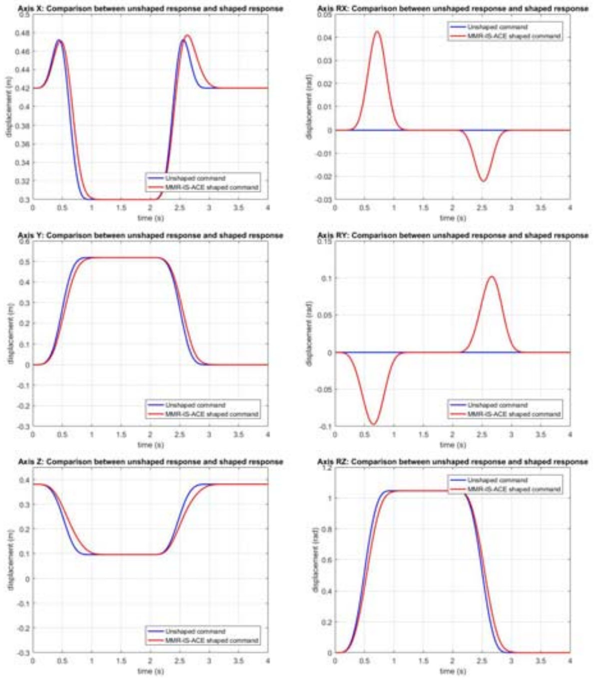

Fig. 16 Comparison between the unshaped and shaped commands for the end-effector. Upper-left to lower-left are x, y and z. Upper-right to lower-right are orientations x, y and z. blue-unshaped, red-shaped.

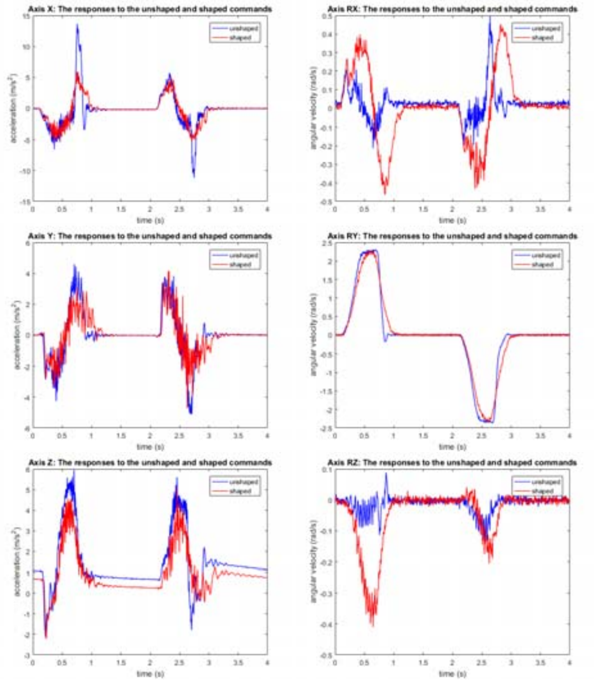

Fig. 17 End-effector accelerations with the unshaped and shaped commands. Upper-left to lower-left are x, y and z. Upper-right to lower-right are orientations x, y and z. blue-unshaped, red-shaped.

VII. CONCLUSIONS

In this paper, two topics are emphasized. One is to improve the existed input shaping approach. The modified zero time-delay input shaping with contour-error compensation is proposed to eliminate both the delay time and the contour error. The other topic is to combine the MMR-IS-ACE with the motor-side feedback controller. The desired trajectories and their first four derivatives are planned by means of the properties of the convolution, which are necessary to the feedback control based on elastic-joint dynamics. Such a feedforward/feedback control architecture guarantees the tracking performance on the motor-side and the suppression of resonance vibrations by the proposed input shaping. From the results of the simulations and experiments, the performance of the proposed method is verified. The vibrations and delay time are obviously eliminated. In addition, the parameters can be used to shape different trajectories, which must be within the limit of joint torque.

REFERENCES

[1] M. S. Alam and M. O. Tokhi, "Hybrid Fuzzy Logic Control with Genetic Optimisation for a Single-Link Flexible Manipulator," *Engineering Applications of Artificial Intelligence*, Vol. 21, No. 6, pp. 858-873, 2008.

[2] Y. Altintas and M. Khoshdarregi, "Contour Error Control of Cnc Machine Tools with Vibration Avoidance," *CIRP Annals-Manufacturing Technology*, Vol. 61, No. 1, pp. 335-338, 2012.

[3] B. Peeters, H. Van der Auweraer, P. Guillaume, and J. Leuridan, "The Polymax Frequency-Domain Method: A New Standard for Modal Parameter Estimation," *Shock and Vibration*, Vol. 11, No. 3, 4, pp. 395-409, 2004.

[4] R. Chaari, F. Djemal, F. Chaari, M. S. Abbes, and M. Haddar, "Experimental Study of Passive Vibration Suppression Using Absorber with Spherical Ball Impact Damper," *Proceedings of the Institution of Mechanical Engineers, Part C: Journal of Mechanical Engineering Science*, Vol. 231, No. 17, pp. 3193-3201, 2017.

[5] W. Chatlatanagulchai, "Model Reference Input Shaping Using Quantitative Feedforward-Feedback Controller," *Engineering Journal (Eng. J.)*, Vol. 21, No. 1, pp. 207-220, 2017.

[6] W. Chatlatanagulchai, S. Nithi-uthai, and P. Intarawirat, "Intelligent Backstepping System to Increase Input Shaping Performance in Suppressing Residual Vibration of a Flexible-Joint Robot Manipulator," *Engineering Journal (Eng. J.)*, Vol. 21, No. 5, pp. 203-223, 2017.

[7] C. S. Chen and L. Y. Chen, "Cross-Coupling Position Command Shaping Control in a Multi-Axis Motion System," *Mechatronics*, Vol. 21, No. 3, pp. 625-632, 2011.

[8] C. S. Chen, Y. H. Fan, and S. P. Tseng, "Position Command Shaping Control in a Retrofitted Milling Machine," *International Journal of Machine Tools and Manufacture*, Vol. 46, No. 3-4, pp. 293-303, 2006.

[9] Z. Chu and J. Hu, "An Improved Recursive Least Square–Based Adaptive Input Shaping for Zero Residual Vibration Control of Flexible System," *Advances in Mechanical Engineering*, Vol. 8, No. 4, pp. 1-14, 2016.

[10] M. O. T. Cole and T. Wongratanaphisan, "A Direct Method of Adaptive Fir Input Shaping for Motion Control with Zero Residual Vibration," *IEEE/ASME Transactions on Mechatronics*, Vol. 18, No. 1, pp. 316-327, 2013.

[11] H. Deng, J. D. Sun, S. D. Huang, and G. Z. Cao, "Vibration Suppression of the Flexible Manipulator Using Optimal Input Shaper and Linear Quadratic Regulator," *Proc. of International Conference on Ubiquitous Robots and Ambient Intelligence (URAI)*, Goyang, South Korea, pp. 255-260, 2015.

[12] A. Dhanda and G. Franklin, "Real-Time Generation of Time-Optimal Commands for Rest-to-Rest Motion of Flexible Systems," *IEEE Transactions on Control Systems Technology*, Vol. 21, No. 3, pp. 958-963, 2013.

[13] K. Erkorkmaz, C. H. Yeung, and Y. Altintas, "Virtual Cnc System. Part Ii. High Speed Contouring Application," *International Journal of Machine Tools and Manufacture*, Vol. 46, No. 10, pp. 1124-1138, 2006.

[14] S. Grazioso, G. Di-Gironimo, W. Singhose, and B. Siciliano, "Input Predictive Shaping for Vibration Control of Flexible Systems," *Proc. of IEEE Conference on Control Technology and Applications (CCTA)*, Mauna Lani, HI, USA, pp. 305-310, 2017.

[15] D. Habineza, M. Rakotondrabe, and Y. Le-Gorrec, "Simultaneous Suppression of Badly Damped Vibrations and Cross-Couplings in a 2-Dof Piezoelectric Actuator by Using Feedforward Standard H∞ Approach," *Proc. of Next-Generation Robotics II; and Machine Intelligence and Bio-inspired Computation: Theory and Applications IX*, Baltimore, Maryland, USA, Vol. 9494, pp. 1-6, 2015.

[16] M. Hromčík and T. Vyhlídal, "Inverse Feedback Shapers for Coupled Multibody Systems," *IEEE Transactions on Automatic Control*, Vol. 62, No. 9, pp. 4804-4810, 2017.

[17] J. M. Hyde and W. P. Seering, "Using Input Command Pre-Shaping to Suppress Multiple Mode Vibration," *Proc. of IEEE International Conference on Robotics and Automation*, Sacramento, California, USA, pp. 2604-2609, 1991.

[18] A. Kamel, F. Lange, and G. Hirzinger, "New Aspects of Input Shaping Control to Damp Oscillations of a Compliant Force Sensor," *Proc. of IEEE International Conference on Robotics and Automation (ICRA)*, Pasadena, CA, USA, pp. 2629-2635, 2008.

[19] M. R. Khoshdarregi, S. Tappe, and Y. Altintas, "Integrated Five-Axis Trajectory Shaping and Contour Error Compensation for High-Speed Cnc Machine Tools," *IEEE/ASME Transactions on Mechatronics*, Vol. 19, No. 6, pp. 1859-1871, 2014.

[20] K. P. Liu, W. You, and Y. C. Li, "Combining a Feedback Linearization Approach with Input Shaping for Flexible Manipulator Control," *Proc. of International Conference on Machine Learning and Cybernetics*, Xi'an, China, Vol. 1, pp. 561-565, 2003.

[21] R. Mar, A. Goyal, V. Nguyen, T. Yang, and W. Singhose, "Combined Input Shaping and Feedback Control for Double-Pendulum Systems," *Mechanical Systems and Signal Processing*, Vol. 85, pp. 267-277, 2017.

[22] R. R. Orszulik and J. Shan, "Active Vibration Control Using Genetic Algorithm-Based System Identification and Positive Position Feedback," *Smart Materials and Structures*, Vol. 21, No. 5, pp. 1-10, 2012.

[23] L. Y. Pao and W. E. Singhose, "On the Equivalence of Minimum Time Input Shaping with Traditional Time-Optimal Control," *Proc. of IEEE Conference on Control Applications*, Albany, NY, USA, pp. 1120-1125, 1995.

[24] J. Park, P. H. Chang, H. S. Park, and E. Lee, "Design of Learning Input Shaping Technique for Residual Vibration Suppression in an Industrial Robot," *IEEE/ASME Transactions on Mechatronics*, Vol. 11, No. 1, pp. 55-65, 2006.

[25] L. Rupert, P. Hyatt, and M. D. Killpack, "Comparing Model Predictive Control and Input Shaping for Improved Response of Low-Impedance Robots," *Proc. of IEEE-RAS 15th International Conference on Humanoid Robots (Humanoids)*, Seoul, South Korea, pp. 256-263, 2015.

[26] M. H. Shaheed, M. O. Tokhi, A. J. Chipperfield, and A. K. M. Azad, "Modelling and Open-Loop Control of a Single-Link Flexible Manipulator with Genetic Algorithms," *Journal of Low Frequency Noise, Vibration and Active Control*, Vol. 20, No. 1, pp. 39-55, 2001.

[27] J. Shan, H. T. Liu, and D. Sun, "Modified Input Shaping for a Rotating Single-Link Flexible Manipulator," *Journal of Sound and Vibration*, Vol. 285, No. 1-2, pp. 187-207, 2005.

[28] N. C. Singer and W. P. Seering, "Preshaping Command Inputs to Reduce System Vibration," *Journal of Dynamic Systems, Measurement, and Control*, Vol. 112, No. 1, pp. 76-82, 1990.

[29] N. C. Singer and W. P. Seering, "Using Acausal Shaping Techniques to Reduce Robot Vibration," *Proc. of IEEE International Conference on Robotics and Automation*, Philadelphia, PA, USA, pp. 1434-1439, 1988.

[30] W. Singhose, "Command Shaping for Flexible Systems: A Review of the First 50 Years," *International journal of precision engineering and manufacturing*, Vol. 10, No. 4, pp. 153-168, 2009.

[31] M. W. Spong, "Modeling and Control of Elastic Joint Robots," *Journal of dynamic systems, measurement, and control*, Vol. 109, No. 4, pp. 310-318, 1987.

[32] U. Staehlin and T. Singh, "Design of Closed-Loop Input Shaping Controllers," *Proc. of American Control Conference*, Denver, CO, USA, Vol. 6, pp. 5167-5172, 2003.

[33] Y.-G. Sung, W.-S. Jang, and J.-Y. Kim, "Negative Input Shaped Commands for Unequal Acceleration and Braking Delays of Actuators," *Journal of Dynamic Systems, Measurement, and Control*, Vol. 140, No. 9, pp. 1-6, 2018.

[34] M.-S. Tsai, Y.-C. Huang, M.-T. Lin, and S.-K. Wu, "Integration of Input Shaping Technique with Interpolation for Vibration Suppression of Servo-Feed Drive System," *Journal of the Chinese Institute of Engineers*, Vol. 40, No. 4, pp. 284-295, 2017.

[35] J. Vaughan, A. Yano, and W. Singhose, "Comparison of Robust Input Shapers," *Journal of Sound and Vibration*, Vol. 315, No. 4-5, pp. 797-815, 2008.

[36] T. Vyhlidal, M. Hromcik, and V. Kucera, "Inverse Signal Shapers in Effective Feedback Architecture," *Proc. of European Control Conference (ECC)*, Denver, CO, USA, pp. 4418-4423, 2013.

[37] C. Wang, M. Zheng, Z. Wang, C. Peng, and M. Tomizuka, "Robust Iterative Learning Control for Vibration Suppression of Industrial Robot Manipulators," *Journal of Dynamic Systems, Measurement, and Control*, Vol. 140, No. 1, pp. 1-9, 2018.

[38] Y. Wang, Y. Chen, K. Chen, Y. Wu, and Y. Huang, "A Flat Torsional Spring with Corrugated Flexible Units for Series Elastic Actuators," *Proc. of 2nd International Conference on Advanced Robotics and Mechatronics (ICARM)* Hefei, China, pp. 138-143, 2017.

[39] K. Yamada, "Complete Passive Vibration Suppression Using Multi-Layered Piezoelectric Element, Inductor, and Resistor," *Journal of Sound and Vibration*, Vol. 387, pp. 16-35, 2017.

[40] Y. Zhao, W. Chen, T. Tang, and M. Tomizuka, "Zero Time Delay Input Shaping for Smooth Settling of Industrial Robots," *Proc. of IEEE International Conference on Automation Science and Engineering (CASE)*, Fort Worth, TX, USA, pp. 620-625, 2016.

[41] Y. Zhao and M. Tomizuka, "Modified Zero Time Delay Input Shaping for Industrial Robot with Flexibility," *Proc. of ASME 2017 Dynamic Systems and Control Conference*, Tysons, Virginia, USA, Vol. 3, pp. 1-6, 2017.

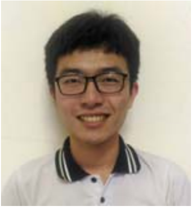

Yean-Yia Lin received the B.S. degree from National Chung Hsing University, Taichung, Taiwan in 2016 ,and M.S. degree from National Taiwan University, Taipei, Taiwan in 2018. He is currently an engineer at Syntec Tech. CO.. His major research interests include robot arm, modal analysis and input shaping.

Zhi-Hao Kang received the B.S. and M.S. degree from Chung Yuan Christian University, Taoyuan, Taiwan in 2009 and 2011, respectively. He is currently working toward his Ph. D. degree in the Department of Mechanical Engineering, National Taiwan University, Taipei, Taiwan. His current research interests include robot arm, model-based control, cyber-physical system and elastic-joint dynamics.

Hsiang-Yuan Ting received the B.S. and M.S. degree from National Chin-Yi University of Technology, Taichun, Taiwan in 2005 and 2007, respectively. He is currently working toward his Ph. D. degree in the Department of Mechanical Engineering, National Taiwan University, Taipei, Taiwan. His current research interests include human robot interaction and safety issues.

Han-Pang HUANG (S'83-M'86) received the M.S. and Ph.D. degrees in electrical engineering from the University of Michigan, Ann Arbor, MI, USA, in 1982 and 1986, respectively.

Since 1986, he has been with National Taiwan University, Taipei, Taiwan, where he is currently a Professor with the Department of Mechanical Engineering and the Graduate Institute of Industrial Engineering and serves as the Director of NTU Robotics Laboratory. He has been elected as a Distinguished Professor of the National Taiwan University since 2006, and held the position of Zhong Zhuo-Zhang Chair Professor since 2009. He served as the Director of Manufacturing Automation Technology Research Center, an Associate Dean with the College of Engineering, the Director of the Graduate Institute of Industrial Engineering, and the Chairperson of Mechanical Engineering with National Taiwan University. His current research interests include machine intelligence, humanoid robots, intelligent robotic systems, prosthetic hands, manufacturing automation, nano-manipulation, and nonlinear systems. He has authored more than 370 papers on those topics, which have been published in refereed technical journals and conference proceedings.

Prof. Huang was a recipient of the Ford University Research Award from 1996 to 1998, the Distinguished Research Award thrice from 1996 to 2002, the Research Fellow Award twice from 2002 to 2008, the Distinguished Research Fellow Award from the National Science Council, Taiwan, in 2009, the Distinguished Education Award on Radio Frequency Identification from EPCglobal in 2010, the TECO Outstanding Science and Technology Research Achievement Award in 2012, the HIWIN Technologies Corp. Distinguished Industry Creation Award in 2014. He was an Editor-in-Chief of the Journal of Chinese Fuzzy System Association from 1997 to 1999, the *International Journal of Fuzzy System* from 1999 to 2002, an Associate Editor of the IEEE TRANSACTIONS ON AUTOMATION SCIENCE AND ENGINEERING from 2003 to 2005, an Associate Editor of the *International Journal of Advanced Robotics Systems*, the IEEE/ASME TRANSACTIONS ON MECHATRONICS, and the Publication Management Committee of IEEE/ASME journals, and an Editorial Board Member of the *International Journal of Advanced Robotics* from 2004 to 2008 and the *International Journal of Service Robots*. He is currently on the editorial board of the *International Journal of Electronic Business Management*, and an Editor of the *International Journal of Automation and Smart Technology*. He was named in Who's Who in the World 2001, 2002, and Who's Who in the R. O. C. 2002. He has served as the Committee Chair/Co-Chair and a member of several national, international, and the IEEE conferences. He was a fellow of the Chinese Institute of Automation Engineers in 2010 and the Chinese Society of Mechanical Engineers in 2011.

Task Allocation and Food Servicing of a Collaborative Multi-Robot System for IOT-based Intelligent Restaurant

Ting-Yu Luke Lin, Ching-Chih Tsai, and Feng-Chun Tai

Abstract-**This paper presents a task allocation and food servicing method for collaborative multi-robots operating at an IoT (internet of things)-based intelligent restaurant, aiming at performing the goals of intelligent restaurant by handling different tasks. This multi-robot system consists of three kinds of mobile service robots: one is the reception robot to go to the doorway to welcome customers and lead them to available seats, the other is the meal-carrying robot to deliver the ordered meal to the corresponding customers, and another is the service robot to get customers' orders and transfer them to the cook via IoT, and stand by to serve the customer for extra requests. Based on ROS (robot operating system), a boss node is created to receive requests from other end devices such as Laptops and Smart phones. Once all robots' status has been known through Actionlib package in ROS, suitable tasks with priority will be distributed by the boss node to available robots. A market-based allocation approach is then proposed to find the best robot to complete a task with the minimum cost. Once the tasks have been allocated, a multi-robot path planning method based on the shortest path is used to obtain the optimal path of each robot with the capability of adaptive Monte Carlo Localization (AMCL). Simulations and experimental results are performed to show the effectiveness and merits of the proposed collaborative multi-robot system for an IoT (internet of things)-based intelligent restaurant.**

***Index Terms*—Collaboration, human-robot interactions, intelligent restaurant, IOT (Internet of Things), multi-robot, navigation, ROS (Robot Operating System), market-based allocation, multi-robot path planning, adaptive Monte Carlo Localization.**

I. INTRODUCTION

RECENTLY, service robots have entered humans' life and assist their daily life. Several practitioners in China have implemented service robots in restaurants [1]. In one of Ningbo's restaurants, meal delivery has been serviced by two mobile robots which have one-meter height. They mainly trace white line on the floor to deliver the meal. Once they have reached the customer's seats, they will have voice interaction with the customers. In one of Suzhou's restaurants, the robot can order meals, make meals, deliver meals, and perform a show for customers. In one of Harbin's restaurants, there exist several kinds of robots that handle different tasks such as dumpling cooking robot, noodles cooking robot, vegetables cooking robot, ground meal delivery robot, air meal delivery robot, and reception robot. In one of Jiangxi's restaurants, a noodle-cutting robot can make four bowls of noodles within 5 minutes.

The capability of indoor navigation for an autonomous mobile robot inside intelligent restaurants is a very challenging problem. The mobile robot's localization is one of the most fundamental problems in mobile robot's navigation. A well-known solution to this problem is to establish an occupancy grid map of the environment and uses it to determine the navigation direction such that the robot is guided towards a desired goal. Adaptive Monte Carlo Localization (AMCL) [2] is an efficient way to localize the robot in the given map.

With multi-robot system, tasks can be handled more efficiently by proper task allocation methods such as bio-inspired approach, market-based approach, and knowledge-based approach [3]. The problem of multi-robot task allocation has attracted in-depth studies. For example, Guerrero and Oliver [4] proposed a method to find the shortest amount of time and the optimal number of robots in task allocation through auction algorithm and verified the efficiency of the algorithm in an auction foraging task.

Although mobile robots have been implemented to serve as waiters, they mainly rely on lines on the floor to handle delivery tasks. This motivates us to enable the robots to have autonomous navigation ability based on the map built by SLAM, in order to increase their mobility flexibility. This paper is aimed to develop techniques of mobile collaborative multi-robots for intelligent restaurants. In the presented contents, centralized tasks will be allocated to make multi-robots cope with tasks cooperatively.

The rest of the paper is organized as follows. Section II describes the proposed system architecture equipped with hardware devices and software. Section III provides the detailed description of the adaptive Monte Carlo localization (AMCL) method to localize robots in the given map. Section IV elucidates the multi-robot task allocation method which enables multi-robot to work collaboratively. Section V presents one simulation using three robots to verify the proposed multi-robot task allocation. Section VI presents experimental results to validate the proposed task execution method. Finally, Section VII concludes this paper.

II. SYSTEM STRUCTURE AND DESCRIPTION

This section will introduce the system structure of the experimental setup composed of used mobile robots, ROS and task allocation. In the experimental multi-robotic system,

Ting-Yu Luke Lin, Ching-Chih Tsai, and Feng-Chun Tai are with the Department of Electrical Engineering, National Chung Hsing University, Taichung 40227, Taiwan.
(Corresponding author Ching-Chih Tsai, email: cctsai@nchu.edu.tw)
(email: a4010126@gmail.com, fctai@nchu.edu.tw)

The authors gratefully acknowledge financial support from the Ministry of Science and Technology, Taiwan, the R.O.C., under contract MOST 106-2218-E-005-003-.

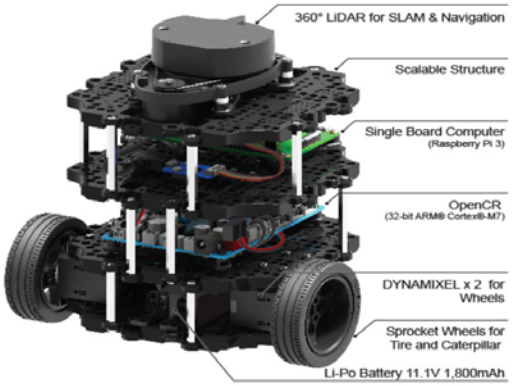

Fig. 1. Turtelbot3 Burger.

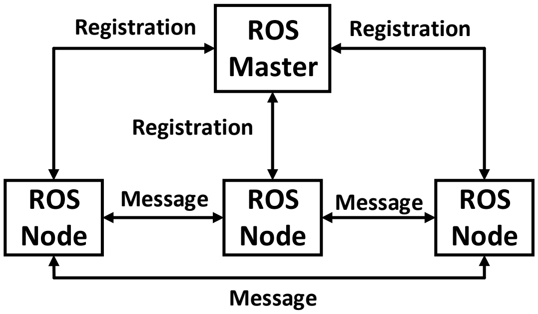

Fig. 2. ROS architecture.

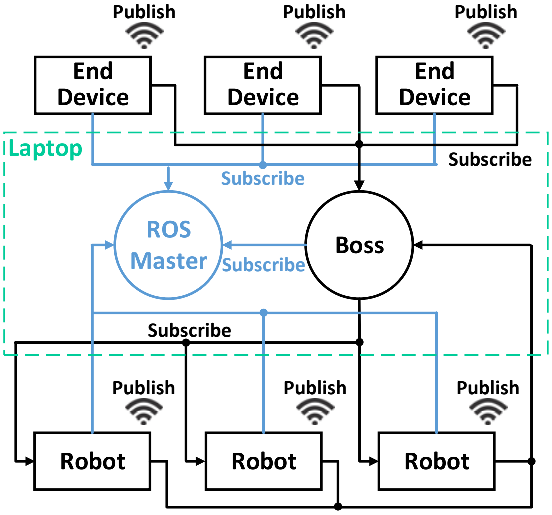

Fig. 3. Implementation of IoT on ROS.

several commercial mobile robots, called Turtlebot3 Burgers, will be used to work as reception, meal-carrying and service robots, depending upon the distances to the task to be completed. A task allocation architecture will be briefly described.

Fig. 1 shows the experiment robot, Turtlebot3 Burger [5], which is equipped with one Raspberry Pi3, one LiDAR sensor, one OpenCR control board, two Dynamixel motors and drivers. Fig. 2 depicts the ROS architecture [6] which is the main software framework of the experiment robot. Fig. 4 shows the task allocation architecture in which all the robots will link to the ROS Master in the laptop, and the Boss node will subscribe the status of each robot and then allocate desired tasks to them based on their cost to finish the task.

TABLE I. AMCL ALGORITHM

```
AlgorithmKLD_Sampling_MCL ($S_{t-1}, u_t, z_t, m, \varepsilon, \delta$):
  $S_t = \varnothing$
  $M = 0, M_X = 0, k = 0$
  for all b in H do
    b=empty
  endfor
  do
    draw I with probability $\propto \omega_{t-1}^{[i]}$
    $s_t^{[M]}$ = sample_motion_model($u_t$, $s_{t-1}^{[i]}$)
    $\omega_t^{[M]}$ = measurement_model($z_t$, $s_t^{[M]}$, m)
    $S_t = S_t + \langle s_t^{[M]}, \omega_T^{[M]} \rangle$
    if $s_t^{[M]}$ falls into empty bin b then
      k=k+1
      b=non-empty
      if k>1 then
        $M_X := \frac{k-1}{2\varepsilon}\left\{1-\frac{2}{9(k-1)}+\sqrt{\frac{2}{9(k-1)}}z_{1-\delta}\right\}^3$
    endif
    M=M+1
  while $M < M_X$ or $M < M_{X\min}$
  return $S_t$
```

III. ADAPTIVE MONTE CARLO LOCALIZATION

This section will propose a localization method for a mobile robot to localize itself in a given map. The AMCL method is a well-known probabilistic localization system for a robot moving in a 2D map. Because the robot may not behave in a perfectly predictable way, it generates many random guesses of where it is going. Theses guesses are particles, each of which contains a full description of a possible future state. When the robot observes the environment via LiDAR, it discards particles inconsistent with this observation, and generates more particles close to those that appear consistently. Table 1 overviews the AMCL algorithm. At every time t, the algorithm takes the previous belief $S_{t-1} = \left\{s_{t-1}^{[1]}, s_{t-1}^{[2]}, \ldots, s_{t-1}^{[M]}\right\}$, an actuation command u_t, data received from sensors z_t, landmark location m, and statistic error bounds ε and δ ; and then the algorithm outputs the new belief S_t.

In this algorithm, the AMCL method is improved by sampling the particles in an adaptive manner based on an error estimate using the Kullback-Leibler divergence (KLD). Initially, it is necessary to use a large M to cover the entire map with a uniformly random distribution of particles. Once the particles have converged, maintaining such a large sample size is wasteful. The KLD-sample scheme is a variant of the Monte Carlo Localization where at each iteration, the sample size, M_X , is calculated. The sample size M_X is calculated such that, with probability $1-\delta$, the error between the true posterior and the sample-based approximation is less than ε . Both variables, δ and ε , are fixed parameters. The main idea behind this is to

TABLE II. DIJKSTRA ALGORITHM.

```
Function Dijkstra (Graph, source):
    for each vertex in Graph:
        dist[v] := infinity;
    previous[v] := undefined
end for
dist[source] := 0;
Q := the set of all nodes in Graph
while Q is not empty:
    u := vertex in Q with smallest distance in dist[];
    remove u from Q;
    if dist[u]=infinity;
        Break
    endif
    for each neighbor v of u
        alt := dist[u]+dist_between (u,v);
        if alt < dist[v]:
            dist[v] := alt;
            previous[v] := u;
            decrease-key v in Q;
        end if
    end for
end while
return dist
End Function
```

TABLE III. DWA ALGORITHM.

1. Discretely sample robots control space (dx,dy,dtheta).
2. For each sampled velocity, perform forward simulation for the robot to see the result of the sampled velocity applied for a period of time.
3. Evaluate each trajectory from the result of forward simulation, using a metric that includes properties such as: proximity to obstacles, proximity to goal, and proximity to the global path and discard those collide with obstacles. The cost function is defined as follows:

$$
\begin{aligned}
&cost\\
&= path\ distance\ bias *\\
&\quad (distance\ to\ path\ from\ the\ endpoint\ of\ the\ trajectory)\\
&+ goal\ distacne\ bias *\\
&\quad (distance\ to\ local\ goal\ from\ the\ endpoint\ of\ the\ trajectory)\\
&+ occdist\ scale *\\
&\quad (The\ closer\ to\ the\ obstacle\ the\ higher\ of\ this\ cost)
\end{aligned}
$$

4. Pick the highest-score velocity and send it to the robot.
5. Rinse and repeat.

create a grid (a histogram) overlaid on the state space. Each bin in the histogram is initially empty. At each iteration, a new particle is drawn from the previous (weighted) particle set with probability proportional to its weight. The KLD-sampling algorithm draws particles from the previous, weighted, particle set and applies the motion before placing the particles into its bin. This algorithm keeps track of the number of non-empty bins, *k*. If a particle is inserted in a previously empty bin, the value of M_x is recalculated so as to increase mostly linearly in *k*. This process is repeated until the sample size *M* is the same as M_x. In practice, the KLD-sampling consistently outperforms and converges faster than classic MCL.

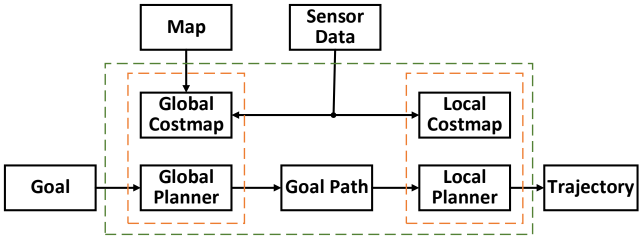

Fig. 4. Navigation flowchart.

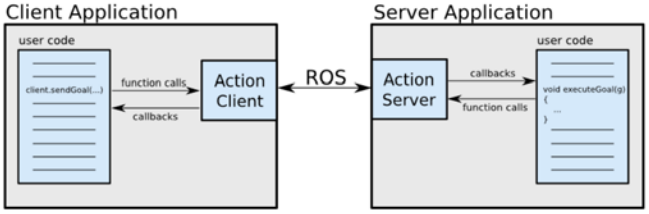

Fig. 5. Client-Server Interaction.

IV. MULTI-ROBOT TASK ALLOCATION

The purpose of this section is to propose a task allocation method for the collaborative multi-robot system. The task allocation architecture will be first delineated and the multi-robot path planning method will be explained for each robot to avoid collisions when handling tasks.

4.1 Navigation

When the robot gets requests from the Boss node in Fig. 3, the robot will start to navigate itself to its destination, in order to finish desired task. Fig. 4 illustrates the process for navigation based on a given map [7]. When the goal is sent out, the global planner will produce a global path trajectory that won't hit any obstacles in the global map based on the shortest path Dijkstra's algorithm [8], as shown in Table 2. After the global path is planned by the global planner, the local planner will activate obstacle avoidance at any time based on the sensing data. The DWA (Dynamic Window Approach) [9] is used for the local planer. The idea of DWA is shown in Table 3.

4.2 Task Allocation Architecture

Once the Boss node has gathered requests from the end devices, it will start to transmit the tasks stored in the first-in first-out queue to the robots. The robots register under the ROS Master in the laptop, and the Boss node will communicate with robots through Actionlib [10]. The Actionlib package provides a standardized interface for interfacing with preemptable tasks. For example, this package can include the task of moving the robot to a target location and performing a laser scan and returning the resulting point cloud. Moreover, this Actionlib package not only provides tools to create servers that execute long-running goals that can be preempted, but also offers a client interface in order to send requests to the server.

The ActionClient and ActionServer, shown in Fig. 5, communicate via a "ROS Action Protocol", which is built on the top of ROS messages. The client and server provide a simple API for users to request goals (on the client side) or to execute goals (on the server side) via function calls and

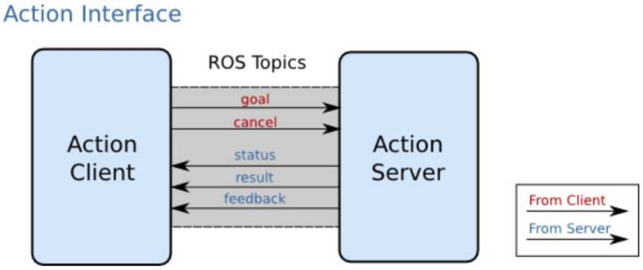

Fig. 6. Action Interface & Transport Layer.

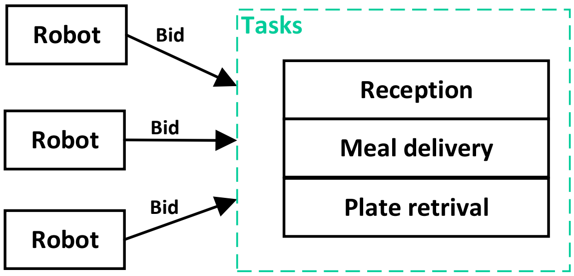

Fig. 7. Market-based approach for task allocation.

callbacks. The action protocol relies on the ROS topics in a specified ROS namespace in order to transmit messages as shown in Fig. 6. In the following, the Goal, Feedback, and Result messages are defined in this Actionlib package such that clients and servers communicate with each other.

Goal - used to send new goals to servers
Cancel - used to send cancel requests to servers
Status - Used to notify clients on the current state of every goal in the system.
Feedback - Used to send clients periodic auxiliary information for a goal.
Result - Used to send clients one-time auxiliary information upon completion of a goal.

Through actionlib, the Boss node will be able to send goals to each robots based on their status. Based on the known map and navigation method introduced in the previous section, each robot is able to reach destination after receiving orders from Boss.

Fig. 7 shows market-based approach for task allocation. The tasks are divided into three categories. One is reception, another is meal delivery and the other is plate retrieval. Market-based approach makes use of market economoics to decide how to allocate tasks to multi-robot. Robots communiate to bid for tasks according to their cost to finish the task. Assignments are made by assign each task to the robot that can operate it with shortest distance. Tasks are divided into three levels. Reception has the hishest priority which has to be finished immediately. Meal delievery task takes the second place. Plate retrieval is the lowest which is the last task to be finished.

4.3 Multi-Robot Path Planning

Fig. 8 (a) shows how the multi-robots' path planning is done in their working areas. The triangle denotes the work place and the triangle points in the upper half, lower right, lower left represent the dining room, kitchen, and reception area,

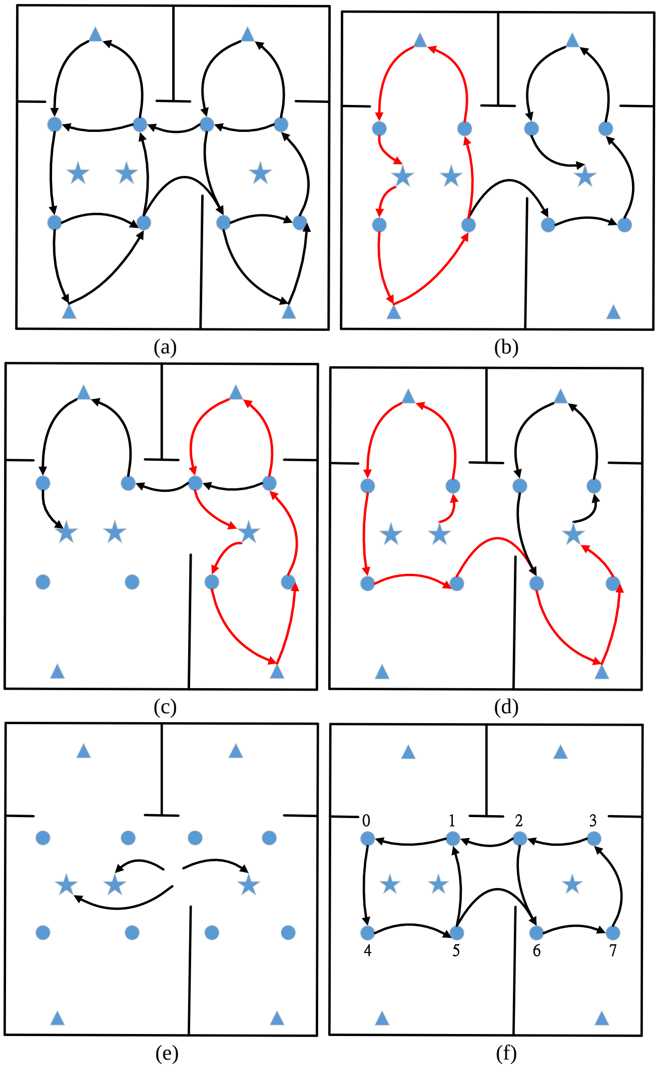

Fig. 8. Path planning of multi-robot: (a) multi-robot's path planning and working area; (b) path planning of reception; (c) path planning of meal delivery; (d) path planning of plate retrieval; (e) all the robots going to standby points when there are no tasks; (f) route for circle points.

respectively. The circle denotes the transition point to the work place. Each robot will pass through the circle point to the work place. When the task is finished, each robot will leave the task point by passing through circle point to serve other tasks. The star means the standby point. When there are no tasks, all the robots will go to the star point to wait for another task from the boss node. Fig. 8 (b) shows the path planning of reception; the reception robot will go to the triangle point to handle reception task by passing through the circle point. Afterwards, it will lead customers to the room by passing through circle points. Fig. 8 (c) shows the path planning of meal delivery, where the meal-delivery robot will go to the triangle point to get the meal. Then, it will leave for the dining room to send the meals for the customers. Fig. 8 (d) shows the path planning of plate retrieval. When the customers finish their meals, the robot will go to the dining room to pick all the empty plates and go back to the kitchen. Finally, when there are no tasks from the boss node, all the robots will go to the standby point shown in Fig. 8 (e). The robot's route of circle points in Fig. 8 (f) is described as an adjacency matrix in (1). Since there are eight circle points, the

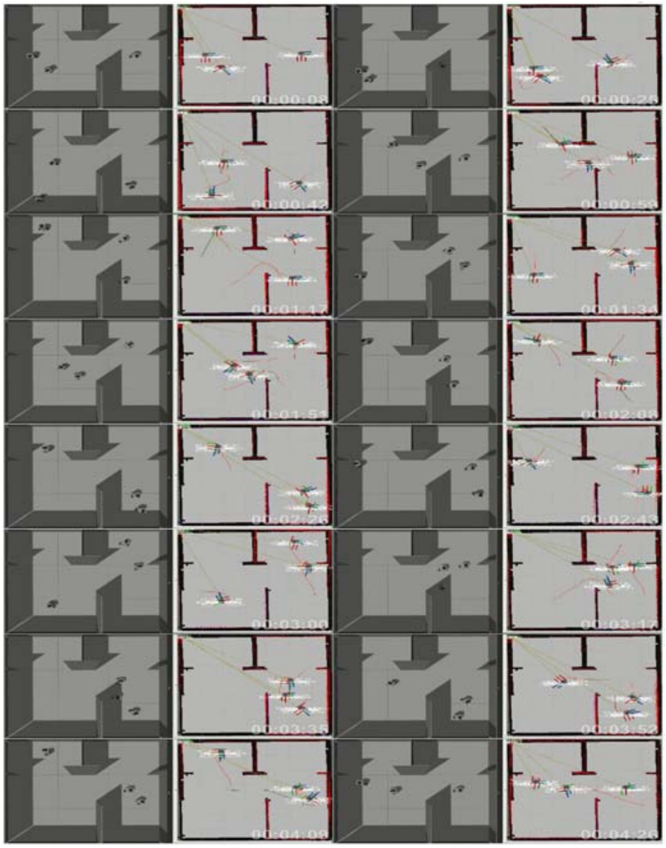

Fig. 9. Simulation resulst of multi-robot task allocation.

TABLE IV. PROCESSING TIME FOR EACH ALLOCATED TASK.

Task	Process time
Reception 1	67.18 s
Reception 2	102.28 s
Meal delivery 1	76.9 s
Meal delivery 2	212.2 s
Plate retrieval 1	184 s
Plate retrieval 2	198.5 s

dimension of the adjacency matrix is 8x8. Where 1 means the two points are connected and the distance of the two points is 1, and 0 means they are not connected. The Dijkstra algorithm will be implemented to find the shortest path to the trangular task point.

$$G = \begin{bmatrix} 0 & 0 & 0 & 0 & 1 & 0 & 0 & 0 \\ 1 & 0 & 0 & 0 & 0 & 0 & 0 & 0 \\ 0 & 1 & 0 & 0 & 0 & 0 & 1 & 0 \\ 0 & 0 & 1 & 0 & 0 & 0 & 0 & 0 \\ 0 & 0 & 0 & 0 & 0 & 1 & 0 & 0 \\ 0 & 1 & 0 & 0 & 0 & 0 & 1 & 0 \\ 0 & 0 & 0 & 0 & 0 & 0 & 0 & 1 \\ 0 & 0 & 0 & 1 & 0 & 0 & 0 & 0 \end{bmatrix}$$

V. SIMULATION AND DISCUSSION

In this section, one simulation is conducted to show the performance of the IoT-based multi-robot task allocation shown in Fig. 9. Two reception tasks, two meal delivery tasks, and two plate retrieval tasks are tested. After the Boss node gathers tasks from customers, the tasks will be divided into three levels. Reception has the highest priority to be finished, meal delivery takes the second place, and plate retrieval is the lowest.

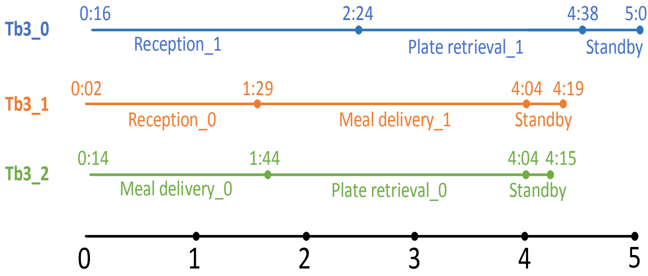

Fig. 10. Process time of each robot.

Fig. 11. Experimental results of the multi-robot task execution.

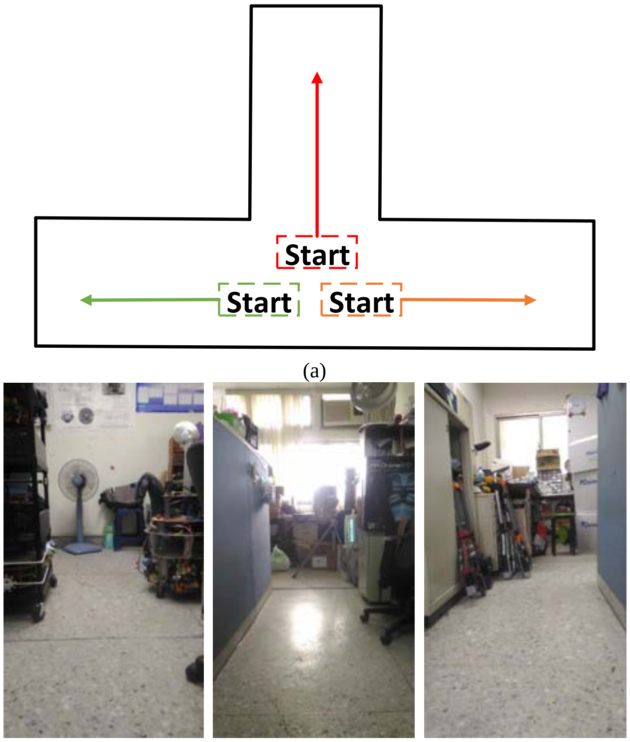

(a)

(b) (c) (d)

Fig. 12. Experiment environment of the three-robot task execution: (a) the floorplan of the experimental environment; (b) the scene of the red line in (a); (c) the scene of the orange line in (a); (d) the scene of the green line in (a).

Fig. 13. Still Pictures during the experimental process of the three-robot task execution.

In the beginning, all the robots will stay at the standby point. Once the tasks are allocated, the three robots will bid for the first reception task, and then other two robots will bid for the remaining tasks. All the robots will follow the path planning in Fig. 8 to avoid collisions with each other. Table IV shows the processing time for each allocated task and Fig. 10 depicts the process time of each robot.

VI. EXPERIMENT AND DISCUSSION

In this section, an experiment is conducted to examine the performance of the multi-robot task execution. Fig. 11 shows the still pictures of the two mobile robots doing the reception and meal delivery tasks, respectively. The results have validated the applicability of the proposed task allocation and task execution method. Fig. 12 displays the experimental environment and Fig. 13 shows the still pictures during the experimental process of the two-robot task execution. Similar to the two-robot task execution, each robot was shown able to reach its destination successfully. To sum up, the multi-robot task execution experiment was shown effective in taking the advantage of finishing tasks in a shorter time. Further, coordination and software framework of the multi-robot remains to be done in accomplishing the multi-robot task execution smoothly.

VII. CONCLUSIONS AND FUTURE WORK

This paper has presented techniques for multi-robot task allocation and food servicing of an IoT-based intelligent restaurant. The AMCL algorithm has been successfully implemented via ROS to localize multi-robots in a known map. The IoT-based task reception and task allocation method has been proposed to gather task requests from end devices and allocate tasks to suitable robots to finish the tasks with a minimum cost. The multi-robot path planning has been designed to avoid collisions with other robots. One simulation and one experiment have been conducted for illustration of the effectiveness and applicability of the proposed method. An interesting topic for future work would be to combine the multi-robot method in [11] with the proposed task allocation and task execution method to achieve a more complete task for IoT-based intelligent restaurants.

REFERENCES

[1] Intelligent restaurant in China, [Online]. Available: https://kknews.cc/zh-tw/tech/xrr3z68.html

[2] S. Thrun, W. Burgard, D. Fox, Probabilistic robotics [M]. London: MIT Press, 2005.

[3] L. Parker, “Distributed Intelligence: Overview of the Field and its Application in Multi-Robot Systems,” *Journal of physical agents*, vol. 2, no. 1, March 2008.

[4] J. Guerrero and G. Oliver, "Multi-robot task allocation strategies using auction-like mechanisms[J]", *Artificial Research and Development in Frontiers in Artificial Intelligence and Applications*, vol. 100, pp. 111-122, 2003.

[5] Turtlebot3 – ROBOTIS e-Manual, [Online]. Available: http://emanual.robotis.com/docs/en/platform/turtlebot3/overview/

[6] ROS 101: Intro to the Robot Operating System, [Online]. Available: http://robohub.org/ros-101-intro-to-the-robot-operating-system/

[7] ROS navigation, [Online]. Available: http://wiki.ros.org/navigation

[8] Dijkstra's algorithm. [Online]. Available: https://en.wikipedia.org/wiki/Dijkstra%27s_algorithm

[9] D. Fox, W. Burgard and S. Thrun, "The dynamic window approach to collision avoidance," *IEEE Robotics & Automation Magazine*, vol. 4, no. 1, pp. 23-33, Mar. 1997.

[10] Actionlib, [Online]. Available: http://wiki.ros.org/actionlib.

[11] T. Y. Lin, C. C. Tsai, and F. C. Tai, "LiDAR-Based Distributed Multi-Robot SLAM Using ROS," in *Proc. of 2018 International Conference on Systems Sciences and Engineering*, National Taipei University, New Taipei City, Taiwan, 28-30 June, 2018.

Ting-Yu Luke Lin received the B.S. and MS degrees in the Department of Electrical Engineering, National Chung Hsing University, Taichung, Taiwan, ROC, in 2016 and 2018, respectively. His current research interests include deep learning, intelligent computing and intelligent robotics with their applications to smart machinery.

Ching-Chih Tsai received the Diplomat in Electrical Engineering from National Taipei Institute of Technology, Taipei, Taiwan, ROC, the MS degree in Control Engineering from National Chiao Tung University, Hsinchu, Taiwan, ROC and the Ph.D degree in Electrical Engineering from Northwestern University, Evanston, IL, USA, in 1981, 1986 and 1991, respectively. Currently, he is currently a Distinguished Professor in the Department of Electrical Engineering, National Chung-Hsing University, Taichung, Taiwan, where he served the Chairman in the Department of Electrical Engineering from 2012 to 2014. He is a Fellow of IEEE, IET and CACS.

Dr. Tsai served as the Chair, Taipei Chapter, IEEE Control Systems Society, from 2000 to 2003, and the Chair, Taipei Chapter, IEEE Robotics and Automation Society from 2005 to 2006. In 2007, he was the program chair of 2007 CACS international automatic conference sponsored by Taipei chapter, IEEE control systems society. In 2010, he served as the program co-chair of SICE 2010 annual conference in Taiwan, which was technically sponsored by IEEE CSS; in 2011, he served as the General Chair, 2011 International conference on service and interactive robotics; in 2012, he has served as the General Chair, 2012 International conference on Fuzzy Theory and Its Applications, the General Chair, 2012-2015 CACS International Automatic Control Conferences, and the General Chair, 2016-2017 International Conference on Advanced Robotics and Intelligent Systems. Dr. Tsai served the two-term President, Chinese Institute of Engineers in Central Taiwan, Taiwan from 2007 to 2011, and two-term President of Chinese Automatic Control Society from 2012 to 2015. Since 2008, he has been the Executive Directors in Boards of Government of thee professional associations, including Robotic Society of Taiwan, Taiwan Fuzzy Systems Association, and Taiwan Systems Association. He has served as the Chair, Taichung Chapter, IEEE Systems, Man, and Cybernetics Society since 2009, the Chair of IEEE SMC Technical Committee on intelligent learning in control systems since 2009, the President of Robotics Society of Taiwan since 2016, the steering committee of Asian Control Association since 2014, a BOG member of IEEE Nanotechnology council since 2012, the Vice President of International Fuzzy Systems Association since 2015, and a BOG member of the IEEE SMCS since 2017.

Dr. Tsai has published more than 500 technical papers, and seven patents in the fields of control theory, systems technology and applications. Web of Science has indexed his paper entitled "Adaptive Neural Network Control of a Self-Balancing Two-Wheeled Scooter" in the category Automation Control Systems, where the paper was ranked 408 out of 37607 articles (published between 2010 to 2014). Dr. Tsai is respectively the recipients of the Third Society Prize Paper Award from IEEE Industry Application Society in 1998, the Outstanding Automatic Control Engineering Award in 2008 from Chinese Automatic Control Society (CACS), and the Outstanding Engineering Professor Award in 2009 from the Chinese Institute of Engineers in 2009, the IEEE Most Active SMC Technical Committee (TC) Award in 2012 from IEEE SMC Society, the Outstanding Electrical Engineering Professor Award from the Chinese Institute of Electrical Engineering in 2014, Outstanding Industry Contribution Award from Taiwan Systems Association in 2016, the best paper award in the International Journal of Fuzzy Systems in 2017, and many best paper awards from many international conferences technically supported by IEEE. He is the advisor, IEEE SMC student branch chapter at National Chung Hsing University; this chapter was the recipient of certificate of appreciation from IEEE SMCS in 2009. He has served as the associate editors of International Journal of Fuzzy Systems, and IEEE Transactions on Systems, Man and Cybernetics: Systems, IEEE Transactions on Industry Informatics, and International Journal of Electrical Engineering. Recently, he has served as the Editor-in-Chief of a new international robotics journal called "iRobotics". His current interests include advanced nonlinear control methods, deep model predictive control, advanced fuzzy control, advanced neural-network control, advanced mobile robotics, intelligent service robotics, intelligent mechatronics, intelligent learning control methods with their applications to industrial processes and smart machinery.

Feng-Chun Tai received the B.S., M.S. and Ph.D. degrees in Department of Electrical Engineering from National Chung Hsing University, Taichung, Taiwan, ROC. in 2007, 2010 and 2018, respectively. His current research interests include mobile robots, intelligent control, navigation system and their applications to industrial processes and machines.

Information for Authors

Aim and Scope

The *i***Robotics** is an official journal of Robotics Society of Taiwan (RST) and is published quarterly. The *i***Robotics** will consider high quality papers that deal with the theory, design, and application of intelligent robotic system, intelligent artificial system, and extension theory systems ranging from hardware to software. Survey and expository submissions are also welcome. Submission of a manuscript should indicate that it has been neither published, nor copyrighted, submitted, accepted for publication elsewhere (except that the short version may have been presented at the conferences). Submitted manuscripts must be typewritten in English and as concise as possible.

Process for Submission of a Manuscript

The *i***Robotics** publishes two types of articles: regular papers and technical notes. All contributions are handled in the same procedure, where each submission is reviewed by an associate editor who makes an initial decision to send the manuscript out for peer review or to reject without external review. Articles can be rejected at this stage for a variety of reasons, such as lack of novelty, topics outside the scope of the Journal, flaws in the scientific validity, or unprofessional presentation. We are therefore not normally able to provide authors with feedback on rejected manuscripts. If the associate editor believes the article may be of interest to our readers, it is then sent out for external peer review by at least two external reviewers. According the recommendation of the associate editor, the Editor-in-Chief makes the final decision. All manuscripts should be submitted electronically in Portable Document Format (PDF) through the manuscript submission system at [http://www.rst.org.tw]. The corresponding author will be responsible for making page proof and signing off for printing on behalf of other co-authors. Upon acceptance of a paper, authors will be requested to supply their biographies (100 to 200 words) and two copies of the final version of their manuscript (in DOC format and in PDF format).

Style for Manuscript

Papers should be arranged in the following order of presentation:

1) First page must contain: a) Title of Paper (without Symbols), b) Author(s) and affiliation(s), c) Abstract (not exceeding 150 words for Papers or 75 words for Technical Note, and without equations, references, or footnotes), d) 4-6 suggested keywords, e) Complete mailing address, email address, and if available, facsimile (fax) number of each author, f) Preferred address for correspondence and return of proofs, and g) Footnotes (if desired).
2) The text: Submitted manuscripts must be typewritten double-spaced. All submitted manuscripts should be as concise as possible. Regular papers are normally limited to 26 double-spaced, typed pages, and technical notes are 12 double-spaced, typed pages. Please see the Page charge for those who want to submit long papers.
3) Acknowledgements of financial or other support (if any).
4) References: References should be numbered and appear in a separate bibliography at the end of the paper. Use numerals in square brackets to cite references, e.g., [15]. References should be complete and in the style as follows.
   [1] C. C. Lee, "Fuzzy logic in control systems: Fuzzy logic controller - Part I," *IEEE Trans. Syst. Man Cybern.*, vol. 20, no. 2, pp. 404-418, 1990.
   [2] C. Golaszewski and P. Ramadge, "Control of discrete event processes with forced events," in *Proc. of 26th IEEE Conf. Decision and Control*, Los Angeles, CA, pp. 247-251, Dec. 1987.
   [3] P. E. Wellstead and M. B. Zarrop, *Self-Tuning Systems*, New York: Wiley, 1991.
   [4] Project Rezero, available at http://rezero.ethz.ch/project_en.html (last visited: 2017-07).
5) Tables
6) Captions of figures (on separate sheet of paper)

Style for Illustrations

1) It is in the author's interest to submit professional quality illustrations. Drafting or art service cannot be provided by the Publisher.
2) Original drawings should be in black ink on white background. Maximum size is restricted to 17.4 by 24.7 cm. Glossy prints of illustrations are also acceptable.
3) All lettering should be large enough to permit legible reduction of the figure to column width, sometimes as small as one quarter of the original size. Typed lettering is usually not acceptable on figures.
4) Provide a separate sheet listing all figure captions, in proper style for the typesetter, e.g., "Fig. 5. The error for the proposed controller."
5) Illustrations should not be sent until requested, but authors should be ready to submit these immediately upon acceptance for publication.

Page Charges

After a manuscript has been accepted for publication, the author's company or institution will be approached with a request to pay a page charge to cover part of the cost of publication. The charges include:

1) NT$ 5000 for the 10 printed pages of a full paper or for the 6 printed pages of a short paper, and the excess page charge of NT$ 1500 per extra printed page for both full and short papers.
2) For color figures or tables, an additional cost will be charged. The cost, depending on the number of color figures/tables and the final editing result, will be given upon the acceptance of this paper for publication.

Copyright

It is the policy of the RST to own the copyright of the technical contributions. It publishes on behalf of the interests of the RST, its authors, and their employers, and to facilitate the appropriate reuse of this material by others. Authors are required to sign a RST Copyright Form before publication.

Manuscripts (in PDF Format) Submission Website: http://www.rst.org.tw
Editor-in-Chief: Ching-Chih Tsai, Department of Electrical Engineering, National Chung Hsing University, Taiwan
Email: cctsai@nchu.edu.tw
Tzuu-Hseng S. Li, Department of Electrical Engineering, National Cheng Kung University, Taiwan
Email: thsli@mail.ncku.edu.tw
Managing Editor: Dr. Feng-Chun Tai, Department of Electrical Engineering, National Chung Hsing University, Taiwan
Email: fctai@nchu.edu.tw

iRobotics

VOLUME 1, NUMBER 3 SEPTEMBER, 2018

CONTENTS

REGULAR PAPERS

Observer-based Impedance Control for Power Assisting Devices
Chao-Jen Chen, Ming-Yang Cheng, and Chun-Hsien Wu 1

A Wheeled Robot Indoor Positioning System Based on Particle Filter
Yuan-Pao Hsu and Chih-Hao Yang 13

Intelligent Control of a Wheeled Mobile Robot for Path Tracking and Anti-Collision System
Gwo-Ruey Yu and Yu-Shan Chiu 19

Image Recognition and Pick-up Execution of a Robotic Dual-Arm System for Automatic Shoe Sewing
Han-Lin Hsu, Ching-Chih Tsai, and Feng-Chun Tai 27

Vibration Suppression of a 6-DOF Robot Manipulator based on Multi-mode Robust Input Shaping
Yean-Yia Lin, Zhi-Hao Kang, Hsiang-Yuan Ting, and Han-Pang Huang 35

Task Allocation and Food Servicing of a Collaborative Multi-Robot System for IOT-based Intelligent Restaurant
Ting-Yu Luke Lin, Ching-Chih Tsai, and Feng-Chun Tai 47

TECHNICAL NOTE

iRobotics
Volume 1, Number 3, September, 2018